université PARIS-SACLAY

Development of a high spatial resolution functional MRI sequence at ultra-high field

Développement d'une séquence d'IRM fonctionnelle à haute résolution spatiale et à haut-champ

Thèse de doctorat de l'université Paris-Saclay

École doctorale n° 575 : electrical, optical, bio : physics and engineering (EOBE)
Spécialité de doctorat : Imagerie et physique médicale
Graduate School : Sciences de l'Ingénierie des Systèmes, Référent : Faculté des sciences d'Orsay

Thèse préparée dans l'unité de recherche BAOBAB (Université Paris-Saclay, CEA, CNRS), sous la direction de Nicolas BOULANT, directeur de recherche

Thèse soutenue à Paris-Saclay, le 29 septembre 2022, par

Redouane JAMIL

Composition du jury

Alexis AMADON Directeur de recherche, CEA-Saclay NeuroSpin	Président
Wietske VAN DER ZWAAG Directrice de recherche, Spinoza Centre for Neuroimaging, Amsterdam	Rapporteur & Examinatrice
Markus BARTH Professeur, The University of Queensland, Brisbane	Rapporteur & Examinateur
Tony STÖCKER Professeur, Deutsche zentrum für neurodegenerative erkrankungen, Bonn	Examinateur
Benedikt A. POSER Professeur, Maastricht University	Examinateur
Nicolas BOULANT Directeur de recherche, CEA-Saclay NeuroSpin	Directeur de thèse

THESE DE DOCTORAT
NNT : 2022UPAST119

université PARIS-SACLAY

ÉCOLE DOCTORALE
Physique et ingénierie : Electrons, Photons, Sciences du vivant (EOBE)

Titre : Développement d'une séquence d'IRM fonctionnelle à haute résolution spatiale et à haut-champ
Mots clés : IRM, ultra haut champ, haute resolution, IRM fonctionelle, EPI

Résumé : L'imagerie par résonance magnétique fonctionnelle (IRMf) à ultra-haut champ bénéficie d'un rapport signal sur bruit renforcé permettant d'augmenter la résolution spatio-temporelle des images cérébrales. Cette technique consiste à mesurer le changement en amplitude du signal grâce au couplage neurovasculaire induit par l'activité neuronale. Ainsi, une IRM à 11.7T fut installé à NeuroSpin afin de pousser la résolution et sensibilité des acquisitions et approfondir notre connaissance du cerveau humain. Cependant, l'ultra-haut champ s'accompagne d'une plus grande inhomogénéité du champ radiofréquence (RF), générant des zones sombres et une perte de contraste sur l'image. Des solutions de transmission RF ont été développées à NeuroSpin avec succès pour résoudre ce problème. L'objectif principal de cette thèse consiste à développer dans ce contexte des solutions dédiées à l'IRMf (impulsions RF, séquences, reconstruction). Des impulsions RF universelles ont été spécifiquement conçues pour les excitations sélectives afin de bénéficier d'une inhomogénéité de champ RF réduite avec un temps d'acquisition plus court. Les impulsions ont ensuite été implémentées avec succès sur une séquence EPI-3D avec un outil simple de mesure et de correction des artefacts de délais de gradient utilisant des blips de gradient. Enfin, différentes combinaisons de canaux de réception RF optimisant la stabilité du signal ont été explorées. Une solution analytique basée sur les données et optimale pour le rapport signal sur bruit temporel a été proposée, mais celle-ci avait tendance à éroder les pics d'activation, mettant en lumière les limites de cette métrique pourtant largement utilisée.

Title : Development of a high spatial resolution functional MRI sequence at ultra-high field
Keywords : MRI, ultra-high field, high resolution, functionnal MRI, EPI

Abstract : Functional Magnetic Resonance Imaging (fMRI) at ultra-high field benefits from a boosted signal to noise ratio enabling an increase in the spatiotemporal resolution of the human cortex. This technique consists of measuring the signal change induced by neuronal activity through neurovascular coupling. Therefore, a 11.7T MRI has been installed in order to push resolution and sensitivity in the acquisitions and gain detailed knowledge about the human brain. However, ultra-high field comes with more severe radiofrequency (RF) field inhomogeneity resulting in dark region and loss of contrast in the image. RF transmission solutions have been successfully developed at NeuroSpin to tackle this problem. The main goal of this thesis consists in developing in this context dedicated solutions to fMRI (RF pulses, sequences, reconstruction). Universal RF pulses were specifically designed for slab-selective excitations in order to benefit from the reduced RF field inhomogeneity and a shorter acquisition time. The pulses were then successfully implemented into a 3D-EPI with a simple gradient delay measurement and artifact correction tool employing gradient trim blips. Finally, different RF coil combination strategies optimizing signal stability were explored. A data-based and analytical solution optimal in temporal signal to noise ratio was derived but had a tendency to erode activation spikes shading light on the limits of this widely used quality metric.

To my parents, and my brother
I love you

Acknowledgements

Motivated by a strong interest in medical imaging, I spent the first months at NeuroSpin as an intern but doing a Ph.D. was not part of my plans. However, the stimulating work environment and trust that the METRIC team offered convinced me to continue my work through a Ph.D. Therefore, I would like to deeply thank my thesis director **Nicolas Boulant**, for opening to me the doors of NeuroSpin and MRI science and giving me the opportunity to continue my work as a Ph.D. candidate.

Secondly, I would like to thank all the jury members, especially the reviewers Prof. **Wietske van der Zwaag** and Prof. **Markus Barth** for agreeing to expertise my work. I extend my thanks to Prof. **Benedikt Poser**, Prof. **Tony Stocker** and Dr. **Alexis Amadon** for their participation in my jury.

I thank **Franck Mauconduit**, for teaching me everything about sequence coding and definitely making me a better C++ developer. I am very grateful to **Caroline Le Ster**, **Vincent Gras**, **Alexandre Vignaud** and **Cecile Lerman** for their precious help and availability. I also thank **Aurelien Massire** for our digestive walks talking about Blizzard and his fruitful advice and coaching during my job search. The invivo experiments would have been more stressful and harder without the help and kindness of **Chantal Gistiny**, **Yann Lecomte** and **Valerie Berland**.

During these three years, I had the opportunity to collaborate with other teams, I want to first thank the team of **Tony Stöcker** at DZNE Bonn who welcomed me for one week in their lab and made me feel part of the team. I thank **Rüdiger Stirnberg** who provided a great MRI sequence on which I implemented my work. I express my gratitude to the CHU of Poitiers and their 7T platform led by **Rémy Guillevin** who gave me the opportunity to validate my work. I thank also **Mathieu Naudin** and **Marc Lapert**, for helping me with the setup, and providing the proper environment to perform my tests smoothly.

Of course, I was not alone at my desk, the support of other students was very important to me especially during peak covid times. I most importantly want to thank **Chaithya GR**, for his eternal good mood making my three years so much more enjoyable. I express appreciation to **Guillaume Daval-Frerot**, **Pierre-Antoire Comby**, **Paul-François Gapais**, **Zaineb Amor**, **Renata Porciuncula Baptista**. Furthermore, I do not forget to mention **Raghuram**, **Tiffany Bounmy** and **Alexis Thual** for the memorable after works.

Contents

General Introduction 1

I Context 7

1 Magnetic Resonance Imaging for neuroscience 9
1.1 Making an image with MRI . . . 9
1.2 Pulse sequence . . . 15
1.3 Imaging the Brain and BOLD contrast . . . 22

2 Imaging the brain at high resolution 27
2.1 Stakes and challenges of high resolution imaging . . . 27
2.2 Benefits and challenges of ultra high field imaging . . . 32
2.3 Tackling RF transmit field inhomogeneities at ultra-high field . . . 36

II Methodological Developments 43

3 RF pulse design 45
3.1 Slab selective Universal pulse design . . . 46
3.2 Gradient delay correction . . . 51

4 Sequence implementation 61
4.1 Implementation of the pulses in the sequence . . . 61
4.2 Gradient delay diagnostic tool . . . 66

5 Temporal SNR optimization through RF coil combination in fMRI: The more, the better? 71
5.1 Introduction . . . 72
5.2 Theory . . . 73
5.3 Materials & methods . . . 76
5.4 Results . . . 78
5.5 Discussion . . . 82

General Conclusion **87**
Contributions 87

Appendices **89**

A Résumé en français (Abstract in French) **91**

List of Figures **99**

List of Tables **105**

Bibliography **107**

General Introduction

Background

MODERN scientific medicine progress has been more and more linked to technological improvements for the last half century. From automatic adjustable beds, syringe drivers, bladder scanners, ventilators to hemodialysis machines: healthcare and high technology have become intertwined like never before. The area of diagnostics has not been spared either.

Traditionally, diagnosis used to be based on an interview of the patient followed by a clinical examination consisting in an auscultation, palpation, percussion of the patient's body with their hands or rudimentary equipment. Eventually, the doctor would then provide an adapted treatment, but the method could be flawed by the subjectivity of the physician, acting as described by psychologist Daniel Kahneman, like noise in human judgement. For example, a patient suffering from arrhythmia would have to rely on the stethoscope, talent, experience and hearing ability of his doctor in order to get a proper diagnosis. The arrival of ECG transformed the field of cardiology by enabling doctors to record the heart's electrical activity. This offered the ability to have an objective and quantitative measurement that was sharable with colleagues and comparable to other patients. Moreover, the precision of the measurement itself allowed the establishment of range of metrics such as the PQRST sequence for heart rhythm interpretation. Today's cardiologists could not be regarded as serious without proper equipment and practice less and less traditional auscultation.

Diagnosis took a step further when doctors became able to see inside their patients' body noninvasively thanks to medial imaging. From the first image in 1895 by Wilhelm Röntgen, medical imaging extended to various modalities and usage. With radiography, surgical operations became easier to plan and to perform, with echography, pregnancy follow-ups could evaluate the baby's growth and detect or confirm a diagnosis, with positron emission tomography, cancers could be spotted much earlier and followed up during treatment. Thus, Medical imaging became a formidable tool for diagnosis and is now often demanded by the patients themselves. It allowed physicians to explore regions of the body that were usually very hard or even impossible to explore with traditional methods. A typical example of the latter category is the brain. Today, Magnetic Resonance Imaging is the tool of choice when it comes to explore the brain because it offers the best spatial resolution and contrast compared to other modalities. Because MRI is a technique yet still at its infancy compared to other imaging modalities, our understanding of the brain remains limited. In psychiatry, the doctor can evaluate the state of his patient during an interview and then determine if

the patient suffers from bipolar trouble or psychosis for example. However, the diagnosis can be difficult to make based only on an interview. The discipline lacks of quantitative and objective measurements of the clinical state of the patient. Therefore, MRI related methods like functional MRI developed by Seigi Ogawa in 1990 [Oga+90] is a promising tool for neuroscience research. It is already used clinically to prepare brain surgeries and help surgeons to avoid critical brain regions.

Some critical regions such as the hippocampus or the cortex can display a complex structure within a few centimeters. Therefore, in order to explore such regions, neuroscientists and clinicians need often high spatial resolution images. However, in MRI, higher spatial resolution goes with a loss in SNR and/or longer acquisition time. This limit can be repelled by using ultra-high field (>7T) imaging which benefits from a higher signal-to-noise ratio. Initiated in 2004 and delivered in 2017, the 11.7 tesla MRI Iseult became the most powerful whole-body MRI in the world opening a path towards high spatial resolution images of excellent quality. However, at higher magnetic fields, radio frequency field involved in the imaging process gets increasingly inhomogeneous, resulting in dark regions and loss of contrast. These artifacts are referred as B_1 inhomogeneities. During this time, CEA NeuroSpin METRIC team focused on reducing these artifacts. In 2012, Cloos et al. [Clo+12] developed a patented method to alleviate B_1 inhomogeneities by providing a pulse design called k_T-points^{TM} improving image quality. In 2017 in the same team, Gras and al. [Gra+17b] built over the $k_T - points$ foundations the plug-and-play "Universal Pulses" approach, benefiting from lower magnetization flip angle inhomogeneity but without the need of extra calibration scans. The next step is to have a dedicated fMRI sequence to perform functional MRI at 11.7 tesla.

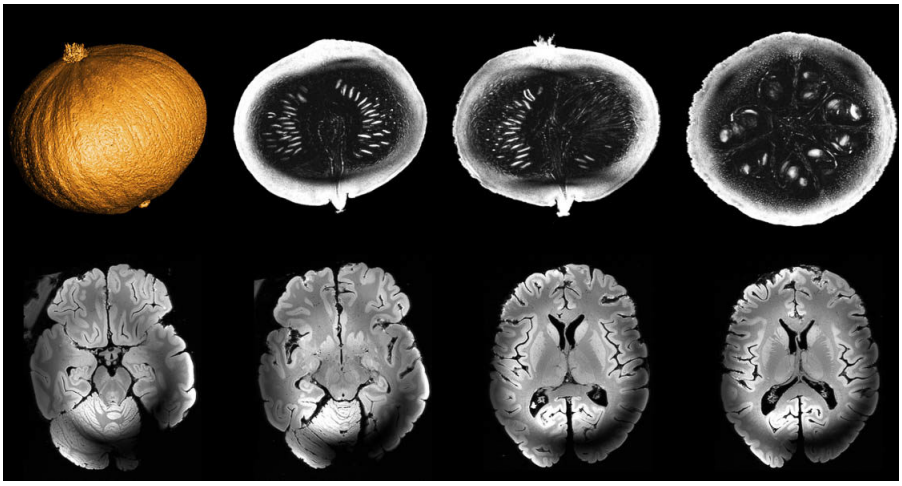

Figure 0.1: **First MR images from Iseult MRI acquired at NeuroSpin**: MR image of a squash and an ex vivo brain at 0.4 mm isotropic resolution. Conventional transmission was used for this method leading to strong signal inhomogeneities in the image. They can be alleviated thanks to the parallel transmission techniques developped at NeuroSpin.

Purpose of this thesis

The goal of this thesis is to provide an MRI sequence that will take advantage of the previously described developments to push fMRI resolution further. An MRI sequence is decomposed

into a series of events including RF pulses for excitation of the magnetization, spatial encoding and readout by means of pulse sequence programming, and image reconstruction. This thesis addresses each one of these items with original research and developments. For RF pulses, Universal Pulses were adapted into slab selective pulses allowing the acquisition of a reduced field of view pushing further spatio-temporal resolution in fMRI with the 3D-EPI sequence. Spoke bipolar RF pulse shapes are preferable over unipolar parametrizations because of their larger robustness versus B_0 field offsets and their shorter duration, allowing shorter echo times. The former, however, is sensitive to gradient delays which impact performance. To overcome this problem, we have implemented the trim-blip approach (gradient blip design and its implementation on the Siemens platform) which is the most general technique, i.e. it only requires knowledge of the delays. This led to a publication in Magnetic Resonance in Medicine. This implementation was first performed on the VB17 software platform for in vivo demonstration on the 7T scanner of NeuroSpin. The tool was further developped and implemented on the VE12 software to be later on exploited on the Iseult 11.7T scanner. This tool is about to be incorporated in the PASTeUR package of universal pulse sequences, disseminated worldwide, and was tested on Siemens Terra scanners. The sequence programming aspect of this work was built upon the 3D-EPI sequence provided by Rudiger Stirnberg (DZNE, Bonn), and incorporated the parallel transmission aspects. Finally, motivated initially by the STARC method for image formation, we explore different methods of RF coil combination for image reconstruction suitable for fMRI and discuss the relevance of signal stability (temporal SNR) as quality metric. We derive an analytical formula for tSNR or t-score for the mean optimality. We show, however, that such methods erode neural activations or are prone to double-dipping, thereby recommending caution when data-driven approaches are used for coil combination and image formation. This work led to one publication in PlosOne.

Thesis Outline

This dissertation will be separated in two parts, the first part introduces the context and the state of the art of MR at ultra-high field, high resolution and for functional MRI. The second part will present my contributions to the field.

Chapter 1: *Magnetic Resonance Imaging for neuroscience* introduces the main physical concepts for MRI followed by a focus on brain imaging and fMRI. We will take this opportunity to motivate the choice of the MRI sequence that will be used.

Chapter 2: *Imaging the brain at high resolution* reviews the challenges of high resolution imaging and the common tools enabling it which is parallel imaging and sampling strategies. Then we introduce the benefits and challenges of ultra-high field imaging and finish by presenting the available solutions to alleviate B_1 field inhomogeneity.

Chapter 3: *RF pulse design* presents the design choices and method of slab-selective Universal Pulses. Next, we introduce a method to correct for gradient delay artifacts these pulses suffer from.

Contributions:

- Showed experimentally the feasibility of *slab-selective Universal Pulses*.

- A general method to correct for gradient delay artifact in bipolar multi spoke RF pulses.

Chapter 4: *Sequence implementation* shows the implementation of the pulses in the sequence.

Contributions:

- *3D-EPI-UP*: A parallel transmit 3D-EPI using Universal pulses for full brain and slab selective excitations, starting from Rudiger Stirnberg's single channel sequence version.
- A quick online tool to measure gradient delays to incorporate this information into the trim-blip compensation approach.

Chapter 5: *Temporal SNR optimization through RF coil combination in fMRI: The more, the better?* investigate optimal RF coil combinations in an attempt to improve BOLD sensitivity.

Contributions:

- Provide an analytical solution for a temporal SNR optimal RF coil combination.
- Similarly, provide a solution to improve the t-score for the mean.

Publications

Accepted articles in Peer-Reviewed Journals

- R. Jamil, F. Mauconduit, V. Gras and N. Boulant. 'General gradient delay correction method in bipolar multispoke RF pulses using trim blips'. In: *Magnetic resonance in medicine* 85.2 (2021), pp. 1004–1012
- R. Jamil, F. Mauconduit, C. Le Ster, P. Ehses, B. A. Poser, A. Vignaud and N. Boulant. 'Temporal SNR optimization through RF coil combination in fMRI: The more, the better?' In: *PloS one* 16.11 (2021), e0259592

Part I

Context

Chapter 1

Magnetic Resonance Imaging for neuroscience

Chapter Outline

1.1 Making an image with MRI . . . 9
1.1.1 Magnetization . . . 10
1.1.2 Excitation . . . 11
1.1.3 Relaxation . . . 13
1.1.4 Reception and Image Reconstruction . . . 14
1.2 Pulse sequence . . . 15
1.2.1 Gradient Recalled Echo . . . 15
1.2.2 Spin-Echo . . . 18
1.2.3 Echo-Planar Imaging . . . 18
1.2.4 Magnetic fields mapping . . . 21
1.2.5 Contrast . . . 22
1.3 Imaging the Brain and BOLD contrast . . . 22
1.3.1 Anatomy and physiology . . . 22
1.3.2 fMRI in practice . . . 23

Magnetic resonance imaging is the association of several scientific breakthroughs. First, was the discovery and description of nuclear magnetic resonance phenomenon by Isidor Rabi in 1939. Edward Purcell and Felix Bloch independently achieved the first measurements of NMR in 1946. Paul Lauterbur and Peter Mansfield introduced in the early 70s the use of gradients in the magnetic field to spatially encode the signal and thus be able to acquire an image. This chapter will describe the physical background behind MRI, then the concept of pulse sequence and its variations are introduced with a focus on the echo planar imaging sequence. Finally, we will see how these methods are used in functional MRI.

1.1 Making an image with MRI

An MR machine has four main components that contribute to reconstruct an image:

- *A Magnet*: To generate a strong magnetic field noted B_0 with a strength on the order of several teslas. The most common design consists in a superconducting solenoid. It is mainly characterized by its aperture and homogeneity sphere size.
- *Gradient coils*: To create an additional spatially linearly varying magnetic field G. Three coils are used in order to create a magnetic field gradient in each spatial direction. Gradient coils are characterized by their peak amplitude (in mT/m), peak slew rate (in mT/m/ms) and their linearity which determines the maximum size of the field of view.
- *A Transmission radiofrequency coil*: To generate a pulsed radiofrequency magnetic field B_1^+ to excite the nuclear spins.
- *A Reception coil*: For reception of the signal. State of the art designs consist of arrays of coil elements making multiple receive channels improving SNR and allowing parallel imaging [Roe+90].

1.1.1 Magnetization

Protons and neutrons have a physical property called spin similar to an angular momentum leading to a dipolar magnetic moment. In presence of a magnetic field, proton spins will align along the main B_0 field. The spins precess at an angular frequency given by Larmor equation:

$$\omega_0 = \gamma B_0 \tag{1.1}$$

with ω_0 in $rad.s^{-1}$, γ the gyromagnetic ratio of the nucleus in $rad.s^{-1}.T^{-1}$ and B_0 in Tesla. It can also be expressed in $Hz.T^{-1}$, for hydrogen, $\gamma = 267.5 \times 10^6 rad.s^{-1}.T^{-1} = 42.6 MHz.T^{-1}$.

MR imaging mostly relies on hydrogen proton spins because of their abundance in the human body. In presence of a magnetic field, spins align in the same direction as the magnetic field (low energy state) or in the opposite direction (high energy state) representing thus two independent energy states. The energy difference is expressed by the Planck relation and Larmor frequency as

$$\hbar\omega_0 = \gamma\hbar B_0 \tag{1.2}$$

with $\hbar = h/2\pi$ and h the Planck's quantum constant. However, spins should fully align with the magnetic field in a low energy state, but thermal motion will tend to equalize both energy states. Considering a sample of spin density $\rho_0 = N/V$ spins with N the number of spins and V the volume, this equilibrium is predicted by the Boltzmann probability distribution which estimates a spins excess in the low energy state:

$$\Delta N \simeq N\frac{\hbar\omega_0}{2kT} \tag{1.3}$$

A cluster of spin excess in a volume V will then form a net magnetization or moment M_0, approximated by the expression

$$M_0 = \frac{\rho_0\gamma^2\hbar^2}{4kT}B_0 \tag{1.4}$$

with k the Boltzmann constant and T the absolute temperature in Kelvins. The magnetization depends on the proton density of the sample and the field strength. The expression shows that by increasing the magnetic field strength, the available net magnetization will be greater. It motivates the need of higher magnetic fields to increase the measured signal. This trend is

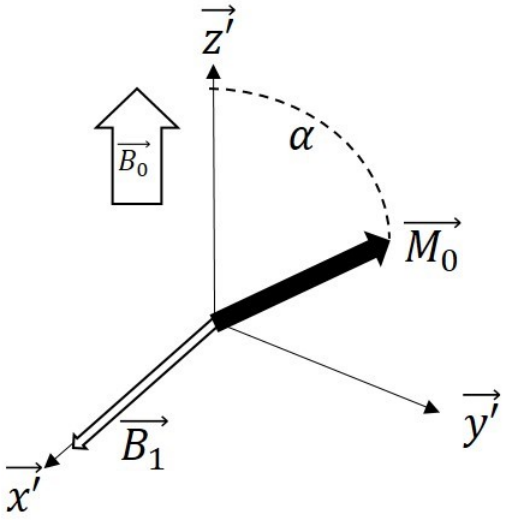

Figure 1.1-1: **Magnetization behavior after an excitation in a rotating frame around $\vec{z}$.**: After an RF excitation, the spin is tilted and a transversal magnetization appears in the $x-y$ plane. The frame of representation is a rotating at the Larmor frequency.

further boosted by Faraday's law of induction in signal detection which gives another factor of B_0 in the signal. We will show now, how this magnetization is reoriented to be measurable and be at the source of the signal.

1.1.2 Excitation

Because proton spins are analogous to precessing gyroscopes, it is possible to describe the behavior of the net magnetization M_0 with classical physics. Let a laboratory frame $(\vec{x}, \vec{y}, \vec{z})$ with a static magnetic field $\vec{B}_0 = B_0\vec{z}$ over a spin isochromat (microscopic volume of spin precessing at the same frequency), the net magnetization in the isochromat is aligned with the magnetic field such that $\vec{M}_0 = M_0\vec{z}$. Spins enter a resonance state if subjected to an orthogonal magnetic field B_1^+ oscillating at their Larmor frequency. For example at $3\mathrm{T}$, setting hydrogen proton spins into resonance requires a magnetic B_1^+ field oscillating at 127.8 MHz.

This result in a tilt of the net magnetization $\vec{M}_0$ around an axis located into the transverse plane $\vec{x} - \vec{y}$ so that

$$\vec{M}_0 = \vec{M}_z + \vec{M}_+ = M_0\cos(\alpha)\vec{z} + M_0\sin(\alpha)\vec{u}\ ,\ \vec{u} \subset (\vec{x}, \vec{y}) \tag{1.5}$$

with α the flip angle (FA) and depends on the RF pulse time integral

$$\alpha = \gamma \int B_1^+(t)dt \tag{1.6}$$

when at resonance and there is no phase modulation on the pulse. α is in degrees, γ in $Hz.T^{-1}$ and B_1^+ in Tesla. Also, we write $\vec{M}_+$ as,

$$M_+(t) = M_x(t) + iM_y(t) = \sin(\alpha)M_0e^{-i\omega_0 t + i\phi_0} \tag{1.7}$$

with ϕ_0 the initial phase of the transverse of the magnetization. Figure 1.1-1 shows the magnetization behavior after an excitation of flip angle α and $\phi_0 = \pi/2$.

It is possible to excite only a region of a sample by adding a magnetic gradient field $\vec{G}$ during the emission of the RF field. This will change the precession frequency of spins spatially. If the B_1^+ field oscillating at the Larmor frequency is generated, only a part of the sample is excited whose extent depends on the spectral profile of the pulse. For example if a gradient $G(z) = G_z z$ (with z the position along axis $\vec{z}$) is applied along $\vec{z}$ the equation (1.1) becomes spatially dependent along $\vec{z}$ and

$$\omega(z) = \gamma(B_0 + G_z z) \tag{1.8}$$

This configuration offers the possibility to excite only a set of spins located in a slice or slab. The position and thickness of the slice depends then on the frequency bandwidth of the RF excitation and the gradient amplitude. The two most common RF pulse shapes are:

- *rectangle shape*: Its Fourier transform is a sinc function, most of the energy is concentrated at 0Hz. It is modulated at the Larmor frequency for non-selective excitations.
- *apodized sinc shape*: the Fourier transform of a sinc shape is a rectangle function, the energy is evenly distributed in a frequency bandwidth around 0Hz for infinite durations. It is typically apodized for instance with Hanning windows to suppress ripples when the pulse duration is finite. An apodized sinc shaped RF pulse will excite spins precessing in the corresponding frequency band. The excitation becomes *selective* when the sinc is modulated and emitted with a gradient along the slice selection axis.

The thickness of the selected slice is typically controlled by the gradient amplitude and the frequency bandwidth of the RF emission. Figure 1.1-2 shows the effect of the gradient on

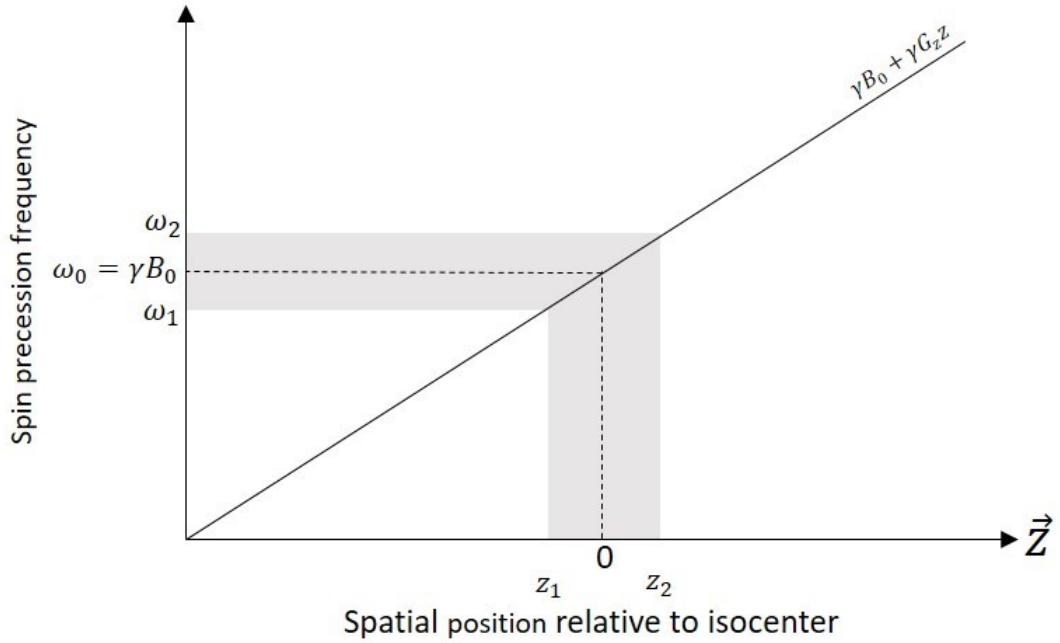

Figure 1.1-2: **Gradient for selective excitation**:Example for a gradient applied along $\vec{z}$. When a sinc shaped RF pulse is emitted coupled with a gradient on an axis, only a slice is selected. The thickness of the slice depends on the bandwidth of the pulse and the gradient amplitude.

the Larmor frequency of spins along an axis. For a slice of thickness $\Delta z = z_2 - z_1$, the RF bandwidth must span from $\omega_2 = \omega(z_2)$ to $\omega_1 = \omega(z_1)$. From 1.8 an excitation bandwidth can be determined

$$BW_{RF} = \omega_2 - \omega_1 = \gamma G_z \Delta z \tag{1.9}$$

with $\Delta z = z_2 - z_1$. Thus the relationship between the slice or slab thickness Δz, the gradient and the RF bandwidth BW_{RF} and G_z is given by

$$G_z = \frac{BW_{rf}}{\gamma \Delta z} \tag{1.10}$$

Slice orientation is also controlled by the gradients. Setting a gradient on two axis during a selective RF excitation will produce an oblique slice excitation. The computation of gradient amplitudes can be done by computing the corresponding gradient amplitude for a non oblique excitation of thickness TH and projecting the result 1.10 in the other axis with the proper rotation matrix R:

$$G = \begin{bmatrix} G_x \\ G_y \\ G_z \end{bmatrix} = R \begin{bmatrix} 0 \\ 0 \\ \frac{BW_{rf}}{\gamma TH} \end{bmatrix} \tag{1.11}$$

Slice position consists simply in adding a frequency offset to the excitation, it is practically performed with a phase modulation of the RF pulse.

1.1.3 Relaxation

After being tilted with an RF excitation, $\vec{M_0}$ will then progressively align itself back with the static field B_0 during a period called relaxation. The dynamics describing relaxation of $\vec{M_0}$ are different for the regrowth of its longitudinal component of the magnetization $\vec{M_z}$ and decay of its transversal component $\vec{M_+}$. They are described by the Bloch equation:

- Each spin will tend to line up back with B_0 through a thermal energy transfer with its environment. The regrowth of the longitudinal magnetization is expressed with the regrowth time T_1 by the relation

$$\frac{dM_z}{dt} = \frac{1}{T_1}(M_0 - M_z) \tag{1.12}$$

- Spins will experience local field interactions with neighboring spins. This causes the decaying of the transversal magnetization expressed with the relaxation time T_2 by the relation

$$\frac{d\vec{M_+}}{dt} = \gamma \vec{M_+} \times \vec{B}_{ext} - \frac{1}{T_2}\vec{M_+} \tag{1.13}$$

These two equations can be combined to describe the spin relaxation into a single vector equation:

$$\frac{d\vec{M}}{dt} = \gamma \vec{M} \times \vec{B}_{ext} + \frac{1}{T_1}(M_0 - M_z)\vec{z} - \frac{1}{T_2}\vec{M_+} \tag{1.14}$$

The evolution of the magnetization components M_x, M_y and M_z during the relaxation period is obtained by solving Bloch equation with $\vec{B}_{ext} = B_0\vec{z}$:

$$M_x(t) = e^{-t/T_2}(M_x(0)\cos\omega_0 t - M_y(0)\sin\omega_0 t) \tag{1.15}$$

$$M_y(t) = e^{-t/T_2}(M_y(0)\cos\omega_0 t + M_x(0)\sin\omega_0 t) \tag{1.16}$$

$$M_z(t) = M_z(0)e^{-t/T_1} + M_0(1 - e^{-t/T_1}) \tag{1.17}$$

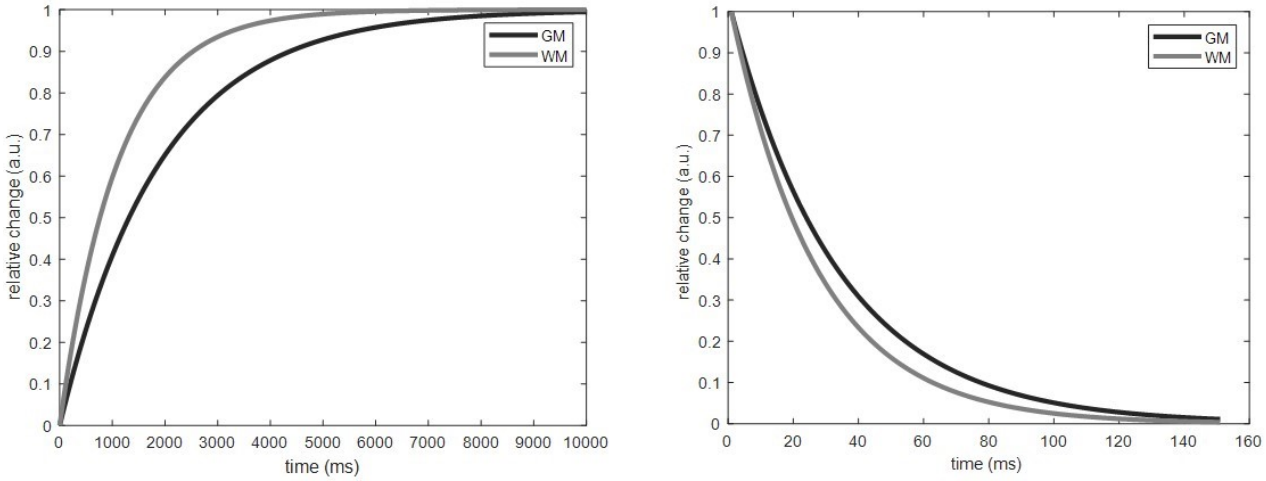

Figure 1.1-3: **Longitudinal regrowth and transversal decay of magnetization** for white matter and gray matter at 7T.

We see here that $M_x(\infty) = 0$, $M_y(\infty) = 0$ and $M_z(\infty) = M_0$ meaning that the net magnetization realigns itself with the static B_0 field. Figure 1.1-3 displays the longitudinal regrowth and the transversal decay of the magnetization for white and gray matter at 7T. From 1.7, 1.15 and 1.16 we have $|M_+(t)| = e^{-t/T_2}\sqrt{M_x(0)^2 + M_y(0)^2}$.

M_z and M_+ follow a first order dynamic with time constant T_1 and T_2 respectively. These time constants depend on the chemical species excited and the field strength and will be at the origin of image contrast allowing the radiographer to distinguish one tissue from another.

Actually, spins do also undergo local static field inhomogeneities that shorten the decay time of transversal magnetization. The total decay time is then noted T_2* and is expressed by

$$\frac{1}{T_2*} = \frac{1}{T_2} + \frac{1}{T_2'} \tag{1.18}$$

where T_2' represents the contribution of field inhomogeneities. This will be employed for functional MRI to measure indirectly neuronal activity.

1.1.4 Reception and Image Reconstruction

Precessing transversal magnetization can be for example measured with a wire loop through induction.

For simplicity, we can neglect the decay factor e^{-t/T_2} and refer directly to the measured and demodulated signal $s(t)$ as

$$s(t) = \iiint \rho(x,y,z)e^{i\varphi(x,y,z,t)}dxdydz \tag{1.19}$$

where φ is the accumulated phase from the precession

$$\varphi(x,y,z,t) = \int \omega(x,y,z,t)dt \tag{1.20}$$

and ρ refers to the spin density.

At this step, the signal comes from one slice or from all the sample depending on the nature of the RF excitation (2D or 3D). As for excitation, gradients will be used to assign

a relationship between space and spin precession frequency and angular phase. With the presence of gradients, equation 1.20 becomes

$$\varphi(x,y,z,t) = \int \omega(x,y,z,t)dt \tag{1.21}$$

$$= -\gamma(x\int G_x dt + y\int G_y dt + z\int G_z dt) \tag{1.22}$$

Gradients are used for two encoding techniques:

- *Frequency encoding*: It consists in setting gradients during the reception of the signal (i.e. when the ADC acquires the signal), the precessing frequency of the spins is then different from one point of the space to another. This allows to distinguish two points in one spatial direction. This gradient plays the role of 'readout' gradients.
- *Phase encoding*: It consists in adding a gradient moment prior to signal reception. For a brief moment, spins will not be precessing at the same frequency creating a phase difference between each other. Again, this dephasing will be spatially dependent allowing to differentiate two data points along one direction.

By performing frequency encoding in one direction and phase encoding in the two others, it is possible to perform 3D imaging. From equation 1.19 and 1.20 we have then a spatial dependence provided by the different encoding.

$$s(k_x,k_y,k_z) = \iiint \rho(x,y,z)e^{-i(k_x x+k_y y+k_z z)}dxdydz \tag{1.23}$$

with

$$k_x(t) = -\gamma\int_0^t G_x(\tau)d\tau\ ,\ k_y(t) = -\gamma\int_0^t G_y(\tau)d\tau\ ,\ k_z(t) = -\gamma\int_0^t G_z(\tau)d\tau \tag{1.24}$$

Equation 1.23 shows that the signal is the Fourier transform of the spatial distribution of spin density. The spin density spatial distribution (i.e. the image) can then be obtained by applying the inverse Fourier transform of s. k_x, k_y and k_z are spatial frequencies in $rad.m^{-1}$, their evolution across time is referred as a trajectory in the Fourier domain also called k-space. In this formalism, gradients are analogous to a displacement speed in the k-space.

1.2 Pulse sequence

The concept of pulse sequence or MRI sequence defines the use of RF pulses and gradients in order to acquire an image. Among the great variety of pulse sequences, for simplicity and relevance we will limit the scope of this chapter to the simplest sequences called gradient recalled echo (GRE), the spin-echo (SE) and the echo-planar imaging sequence (EPI) and few useful B_0 and B_1 mapping sequences that were used extensively throughout this thesis.

1.2.1 Gradient Recalled Echo

After the end of the RF excitation, the net magnetization will immediately return to its original orientation along $\vec{B}_0$. The transversal magnetization will shrink in a first order dynamic with a time constant T_2^*. This is the free induction decay (FID) signal and it is at the core of MR spectroscopy.

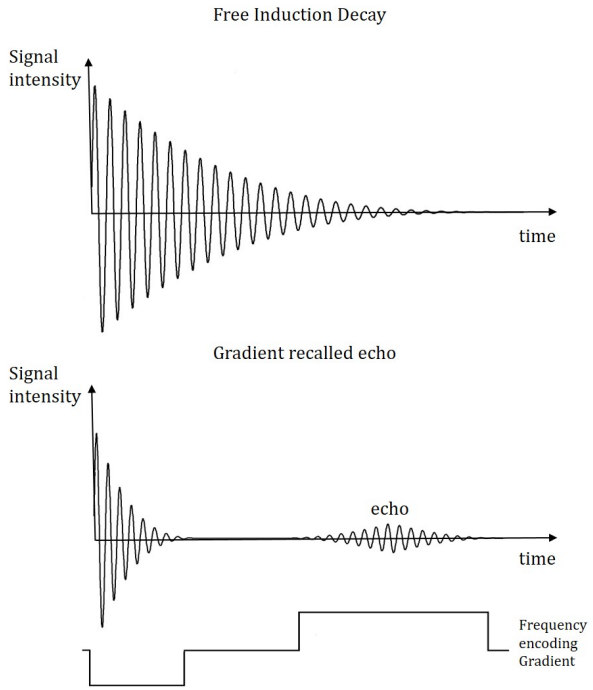

Figure 1.2-4: **Free induction decay signal amplitude versus Gradient recalled echo signal**: the FID signal is oscillating because it is modulated at the Larmor frequency, it is decreasing in a T_2*. The GRE uses two gradient lobes to dephase and rephase again the spins leading to an 'echo'.

Principle

Gradient Recalled Echo consists in creating an 'echo' signal. Figure 1.2-4 shows the evolution of the signal intensity and the frequency encoding gradient for a GRE compared to a FID. A first gradient is applied after the RF excitation to dephase the spins and then a second gradient of opposite polarity is applied that rewinds the phase evolution. Only the spins that were dephased by the first gradient lobe are rephased. Complete rephasing occurs when the net gradient field moment is equal to zero, thus forming an echo. The time between the end of the RF pulse and this instant is the echo time (TE) and can be set up by the user. The period between two RF excitations is the repetition time (TR). In order to ensure the symmetry of the measured echo, the integral of the second gradient (also called read out gradient) is the double of the dephasing gradient. The second gradient lobe also acts as a frequency encoding gradient and the ADC is switched on during this period.

Since gradients are used to generate the echo, we can also describe the sequence from a k-space perspective. Indeed, k-space position is defined by gradients: the first gradient lobe corresponds to a k-space trajectory that goes along a given k-space line from 0 to $-k_{max}$ and the second gradient lobe correspond to a displacement going from $-k_{max}$ to $+k_{max}$. The maximum signal is measured at $k = 0 rad.m^{-1}$. Only one k-space line is here acquired, other lines are acquired by repeating the cycle of RF and gradients. A supplementary gradient moment is used for phase encoding allowing the acquisition of a different k-space line at each TR. Figure 1.2-5 illustrates the relation between the gradients and the k-space trajectory they yield.

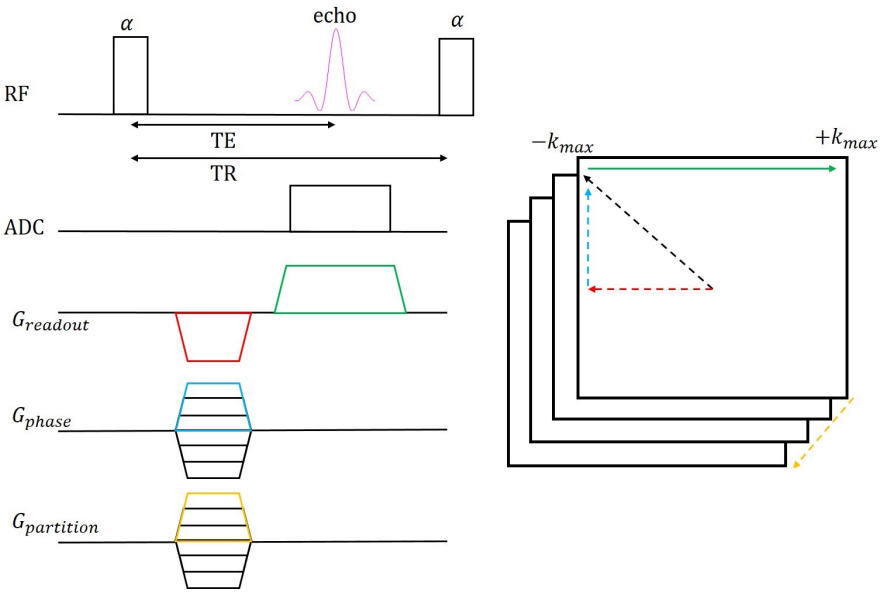

Figure 1.2-5: **3D-GRE chronogram**: Event through time for the GRE are summarized in a chronogram with RF, ADC and gradient events. In the GRE, only one k-space line per TR is acquired. Each line is encoded with the help of phase encode gradient G_{phase} and $G_{partition}$. The color of each gradient is represented by a movement of the same color (arrows) in k-space.

Steady state Magnetization

After the excitation, longitudinal magnetization regrowth follows this expression

$$M_z(t) = M_z(0)e^{-t/T_1} + M_0(1 - e^{-t/T_1}) \tag{1.25}$$

Because regrowth takes time, if the following excitation is performed too early, the signal measured will be weaker from one repetition to another until it stabilizes in the so called steady-state magnetization. The signal measured is weaker because the longitudinal component of the magnetization does not have enough time to regrow completely. For a flip angle α we have after an excitation at $t = 0$ a longitudinal magnetization defined by

$$M_z(0^+) = M_z(0^-)\cos(\alpha) \tag{1.26}$$

After multiple cycles of excitation and relaxation the longitudinal magnetization reaches a steady state $M_{z,ss}$ defined by

$$M_{z,ss} = M_z(TR) = M_z(0^+) \tag{1.27}$$

$$M_{z,ss} = M_{z,ss}\cos(\alpha)E_1 + M_0(1 - E_1) \tag{1.28}$$

$$M_{z,ss} = \frac{M_0(1 - E_1)}{1 - E_1\cos(\alpha)} \tag{1.29}$$

with $E_1 = e^{-TR/T_1}$. Therefore, the transversal magnetization becomes

$$M_{+,ss} = \frac{M_0(1 - E_1)}{1 - E_1\cos(\alpha)}\sin(\alpha) \tag{1.30}$$

This magnetization reaches its maximum at what is defined as the Ernst angle

$$\alpha_E = \arccos(E_1) \tag{1.31}$$

The Ernst angle allows to get the highest signal possible for a given T_1 and TR.

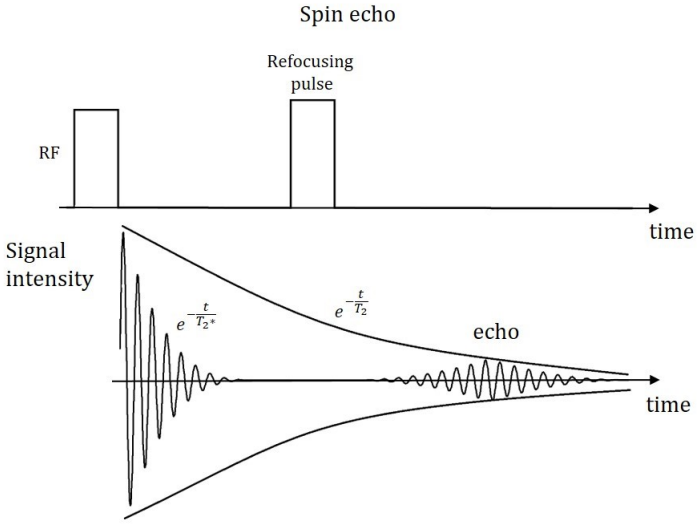

Figure 1.2-6: **Spin echo signal amplitude**: the spin echo allows to recover the T_2 by cancelling the effects static field inhomogeneity on the decay of the transversal magnetization.

1.2.2 Spin-Echo

Principle

The FID signal decreases in a T_2^* dynamic, but it is possible to recover the true T_2 by applying an additional 180° RF pulse between the first RF excitation and the readout. Figure 1.2-6 shows the evolution of the signal intensity and RF excitations for a spin-echo sequence. If we consider a spin isochromat at the emission of the first RF pulse, spins start dephasing because of their interaction with other spins (T_2 decay) and because of local static field inhomogeneities (T_2'). At the emission of the 180° RF pulse, spins' phases are flipped. Slower spins who were behind in phase are now ahead and the faster ones are behind. Because T_2' related static field inhomogeneities remain, the faster spins catch up with the slower spins and the dephasing caused by local field inhomogeneities is cancelled. The acquisition of the signal is similar to the GRE with two gradient lobes yielding the same k-space trajectory.

1.2.3 Echo-Planar Imaging

Principle

Echo-Planar Imaging (EPI) refers to sequences able to acquire one k-space plane with only one excitation. During MRI developments, electronics and gradients became powerful and fast enough to enable the acquisition of a whole k-space plane in one TR. Many k-space sampling schemes and trajectories have been introduced, but the most common one is the Echo Planar Imaging (EPI) sampling scheme. After the RF excitation, the gradients are played in a GRE fashion but in order to acquire a *train* of echos. The second half of each readout gradient acts conveniently as a dephasing gradient for the following gradient echo. By placing gradient blips for phase encoding accordingly, the following readout gradient

will be encoding a new k-space line. Therefore, through a succession of frequency encoding and phase encoding gradients it is possible to travel through the k-space plane after one RF excitation. The acquisition time can be reduced by acquiring data points during gradient ramps. Figure 1.2-7 illustrates the 3D echo planar imaging acquisition.

Important considerations

It is worth noting that the acquisition of odd and even lines is performed with gradients of opposite polarities. Because these commutations can be very fast and with high amplitudes, the EPI technique has two practical shortcomings:

- *N/2 ghosting*: The quick ramping of gradients can induce eddy currents and can induce a time mismatch between the frequency encoding and the ADC resulting in a time shift of the odd versus even echos. This time shift will be positive or negative towards the 'real' echo time and will result in a mismatch of refocalisation between odd and even k-space lines. N/2 ghosting is typically corrected by acquiring two reference scans of the same k-space line but with frequency encoding gradients of opposite polarity. A cross-correlation operation is performed on both signals, the maximum of the cross-correlation is an estimation of the effective time mismatch between both echos and is then used to center back the echoes.

- *Gradient vibrations*: EPI sequence is a notoriously noisy sequence. This noise comes from the interaction of gradient coils with the static field B_0. The quick commutations of the gradients generates strong mechanical vibrations. If their frequency reaches mechanical resonances, the gradient can be damaged. The sequence is thus forbidden to run particular receiver bandwidths that might damage the gradients.

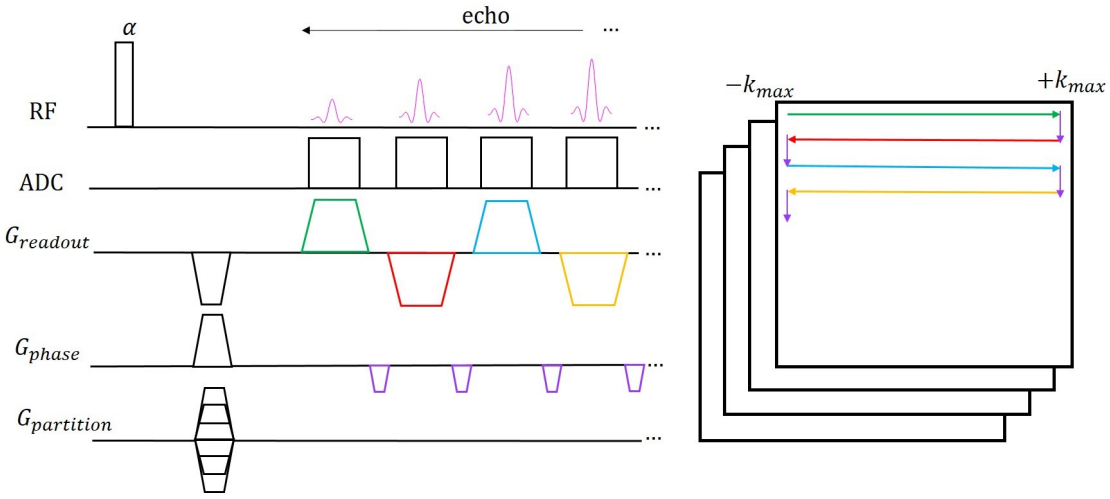

Figure 1.2-7: **3D-EPI chronogram**: Like the 3D-GRE, the 3D-EPI uses two phase encoding gradients. The EPI consists in the sequential acquisition of each line of the k-space plane in a single TR.

Which EPI to choose?

The EPI acquisition technique coupled with the GRE has been the major sequence used for fMRI [Ugu14; PS18] and will be at the core of the developments in this thesis. However, there are many EPI sequences to choose from.

EPI is employed for its speed required to correctly sample signal changes while the GRE is T_2^* weighted for optimal sensitivity to the BOLD signal. GRE based fMRI suffers from spatial inaccuracies because of large vein contributions in the BOLD signal. On the other hand, the intravascular effect are lower at ultra-high field because blood T_2^* is much smaller than the one of intravascular origin. Because spin-echo is less sensitive to extravascular influence, T_2 weighted spin-echo approach has been employed too [De +13]. However, spin-echo requires a 180°refocusing pulse which poses two challenges. On one hand, the high flip angle required can be demanding in SAR. On the other hand, it is harder to get a correct inversion at ultra-high field because of B_1 transmit inhomogeneities. For these reasons, but also for its higher sensitivity, the technique chosen for this thesis will be a GE-EPI.

The other choice that needs to be made is the one between a 2D and a 3D approach. More specifically, one of the most common 2D techniques for EPI is the simultaneous multi-slice (SMS) method. It consists in an excitation of multiple slices with a multiband RF excitation. The acquisition requires only one phase encoding gradient and the aliased slices are separated during the reconstruction step with parallel imaging [Pru+99; Gri+02]. SMS-EPI allows acceleration determined by number of simultaneously excited slices (multiband factor) while under sampling techniques [Pru+99; Gri+02] can be employed along the phase encoding gradient. The resulting noise penalty for the multi slice acceleration is reduced with a controlled aliasing brought by blipped CAIPIRINHA [Set+12]. On the other hand, the 3D approach consists in the repeated excitation of a 'slab'. At each TR, a gradient readout and phase encoding acquire a k-space plane while a second phase encoding gradient enables acquisition of a different k-space plane at each TR. Parallel imaging as well as CAIPIRINHA is available along the two phase encoding gradients offering the same acceleration possibilities as the SMS-EPI. After a time $TR.N_{slices}$ the whole 3D volume is obtained from a 3D Fourier Transform leveraging parallel imaging.

The advantage of 2D single shot EPI is that the image can be obtained after one TR making it less sensitive to physiological noise and motion. However, multiband RF pulses comes with an inherent need of a higher flip angle excitation and higher SAR compared to classic 3D excitation. Indeed, because the effective TR in 2D in the GRE signal equation is equivalent to the TR_{vol} (i.e. the acquisition time of a single volume), the Ernst angle is larger. The need for specific RF pulse spectral profiles also adds energy demands. On the other hand, 3D-EPI benefits from an intrinsic higher SNR from the higher number of data points contribution in the 3D Fourier transform compared to 2D, when spatial resolution is sufficiently high [Pos+10]. A thorough in vivo comparison study with the same fMRI protocol, same volunteers and similar sequence setting between the 3D-EPI and the SMS-EPI showed no clear difference in detecting visual, motor or auditory activations [Le +19]. Finally, the simpler parallel transmission sequence implementation of the 3D-EPI provides presumably more robustness when operating an investigational device such as the 11.7T Iseult MRI. Finally, the absence of gradients during non-selective pulses or more moderate gradients for slab excitations than for slice excitations contributes to less acoustic noise and less peripheral

nerve stimulations.

Therefore, for this thesis the chosen sequence was a 3D-GE-EPI.

1.2.4 Magnetic fields mapping

In order to assess the quality of an RF pulse or correct for distortions, mapping of the static field inhomogeneities ΔB_0 or flip angle maps yielded by a given RF pulse is of great importance for RF pulse design, quality control and troubleshooting.

Bo mapping

B_0 mapping can be used for pulse design and distortion corrections. It is estimated from a GRE sequence with several echo times. The measured phase expression is

$$\phi(x, y, z, TE) = \phi_0 - \gamma \Delta B_0(x, y, z) TE \tag{1.32}$$

with ϕ_0 the phase offset caused by conductivity and permittivity distributions as well for the initial phase of the RF pulse. By acquiring the same GRE image at two echo times ΔB_0, can be estimated as

$$\Delta B_0(x, y, z) = \frac{\phi(x, y, z, TE_2) - \phi(x, y, z, TE_1)}{\gamma(TE_2 - TE_1)} \tag{1.33}$$

Double angle method

The double angle is an indirect method that yields an estimated flip angle map which is a function of the B_1 field strength. It consists in acquiring two images of flip angle α and 2α with a gradient echo or spin echo technique. The flip angle is then recovered with the ratio of both images $s(\alpha)$ and $s(2\alpha)$

$$\alpha = \arccos \frac{s(2\alpha)}{s(\alpha)} \tag{1.34}$$

This technique needs a long $T1$ ($T1 > 5TR$ at least) in order to have a complete regrowth of the longitudinal magnetization and avoid a bias with $T1$.

Actual Flip angle Imaging

Another more accurate and faster flip angle mapping approach [Yar07] consists in a double GRE sequence acquired at two interleaved repetition times TR_1 and TR_2 followed by a spoiling. Repetition times are set up such that $TR_1 < TR_2 < T_1$ and $TR_2 = nTR_1$ with $n = 5$ for our applications. In this configuration, the ratio of the signals from both repetitions s_1 and s_2 can be approximated by

$$r = \frac{s_2}{s_1} \approx \frac{1 + n\cos(\alpha)}{n + \cos(\alpha)} \tag{1.35}$$

The flip angle is then recovered by

$$\alpha \approx \arccos \frac{rn - 1}{n - r} \tag{1.36}$$

1.2.5 Contrast

In order to distinguish between different biological tissues, it is important to choose the right contrast. T_1 and T_2 relaxation are dependent on the tissue type, and it is possible to 'weigh' the image in T_1, T_2 or spin density. The contrast for a 90° flip angle is defined by the difference of signals of two voxels from two tissues of interest A and B by

$$C_{AB} = s_A(TE) - s_B(TE) = \rho_{0,A}(1 - e^{-TR/T_{1,A}})e^{-TE/T_{2,A}} - \rho_{0,B}(1 - e^{-TR/T_{1,B}})e^{-TE/T_{2,B}} \tag{1.37}$$

where s is the spin-echo signal (replace T_2 by T_2^* for GRE) acquired at repeated TR. Image contrast can be set to be mainly dependent on three parameters:

- *Proton density*: By choosing $TR \gg T_1$ and $TE \ll T_2$ we have $(1 - e^{-TR/T_1}) \longrightarrow 1$ and $e^{-TE/T_{2,A}} \longrightarrow 1$ and thus $C_{AB} \longrightarrow \rho_{0,A} - \rho_{0,B}$. Proton density scales the intensity of the voxels by the proton concentration on the voxel. Typically, water-rich soft tissues will be brighter than bones.

- *T1 weighting*: By choosing $TE \ll T_2$ we have $e^{-TE/T_{2,A}} \longrightarrow 1$ and $e^{-TE/T_{2,A}} \longrightarrow 1$. Thus, $C_{AB} \longrightarrow \rho_{0,A}(1 - e^{-TR/T_{1,A}}) - \rho_{0,B}(1 - e^{-TR/T_{1,B}})$. The contrast has a dependence only on $T_{1,A}, T_{1,B}$ and $\rho_{0,A}, \rho 0, B$.

- *T2 weighting*: By choosing $TR \gg T_1$ we have $(1 - e^{-TR/T_1}) \longrightarrow 1$ and thus $C_{AB} \longrightarrow \rho_{0,A}e^{-TE/T_{2,A}} - \rho_{0,B}e^{-TE/T_{2,B}}$. The contrast has a dependence only on $T_{2,A}, T_{2,B}$ and $\rho_{0,A}, \rho_{0,B}$.

1.3 Imaging the Brain and BOLD contrast

MRI is one of the preferred modalities for exploring brain function. Although methods like EEG and MEG have a better temporal resolution, MRI achieves higher spatial resolutions up to sub millimeter isotropic resolutions.

1.3.1 Anatomy and physiology

Brain structure

The brain is the main organ of the central nervous system. It is mainly composed of two cell types, glial cells and neurons. While glial cells have a critical support role in the metabolism of the brain, neurons are the basic processing unit of the activity of the brain by integrating and transmitting information through electrochemical signals. The brain forms thus a complex neuronal network. There are various types of neurons, but they are almost all composed of a cell body that contains its nucleus and mitochondria. It has arborescent dendrites that allow the neuron to receive signal from other neurons and an axon which is a long fiber able to send electrochemical signals to its neighbors. From a macroscopic point of view, the brain is composed of white matter, gray matter, cerebrospinal fluid and fat tissue with a rich vascularization. White matter is composed of axon fibers while gray matter is made of neuron body cells and dendrites. Figure 1.3-8 shows the brain at different scales and schematic view of the neuron.

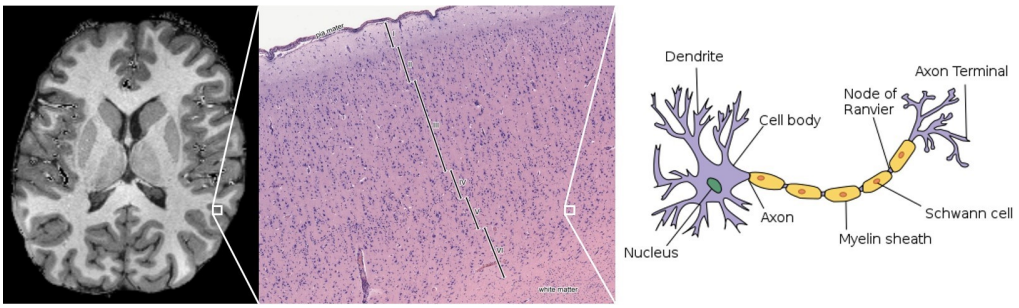

Figure 1.3-8: **The brain from a macroscopic to a microscopic scale**: From left to right, the brain in axial view, the cortex, a neuron.

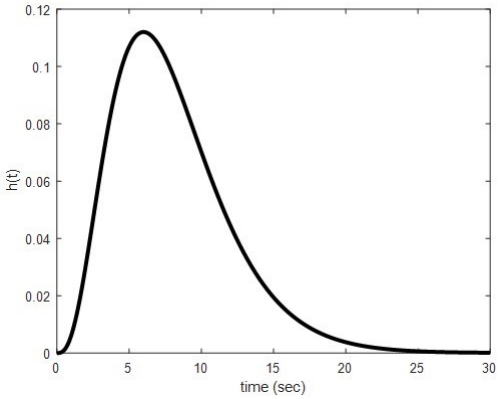

Figure 1.3-9: **The canonical hemodynamic response**: some models also include a signal dip at the beginning and at the end of the spike.

Blood Oxygenation Level Dependent signal

The neuronal activity is correlated to a variation in blood oxygenation meaning that a change in blood flow and in blood volume will occur to bring more oxygen through oxyhemoglobin. It is followed by the consumption of the oxygen resulting in a local increase of deoxyhemoglobin concentration. While oxygenated hemoglobin is diamagnetic, deoxygenated hemoglobin is paramagnetic. Consequently, their relative change in concentration will result in a local change in static B_0 field which is then visible through the local change in T_2' decay. In order to maximize the sensitivity to the BOLD contrast, the GRE echo time is chosen to be equal to the T_2^*. Ogawa et al. [Oga+90] showed that this hemodynamic response could be detected in the MRI signal. The signal change is however of only a few percents of the signal amplitude making it difficult to measure. Figure 1.3-9 shows the signal change of the hemodynamic response through time. All developments and methods improving the quality of the image acquisition, and the post-processing are critical.

1.3.2 fMRI in practice

fMRI experiment and post-processing

Although GRE sequences have been extensively used for fMRI, BOLD signal changes last only 3 or 4 seconds. A fast acquisition sequence like the EPI is needed to respect the Shannon criteria for the temporal resolution allowing a good depiction of the signal change.

There are two major types of fMRI experiments:

- *Task-based*: In order to be able to link neuronal activity in a brain region to a specific function, an experiment is set up where the volunteer has to perform a task or receives visual and/or auditory stimuli while running an MRI acquisition. The set of tasks and onsets can be organized either by blocks creating an on/off paradigm or can be randomly spread throughout the scan in case of event-related paradigms.
- *Resting state*: No task is performed by the subject during the MRI acquisition. This allows to reveal connectivity information between different brain areas by studying the correlations of their respective neuronal activity [Bis12].

fMRI analysis consists in the study of signal variations in the brain across time. However, before the proper analysis, several post-processing steps need to be performed:

- *Motion correction*: functional acquisitions are performed in vivo, and it is important to correct for motion of the volunteer for voxel consistency [Jen+02]. Motion parameters can be estimated with rigid body models and be taken into account as regressors further in the General Linear Model (GLM) analysis. Motion effects on the signal can also be removed with ICA method [BS04] or by adopting prospective approaches using field monitoring techniques for example [Vio+21].
- *Distortion correction*: EPI sequence suffers from B_0 inhomogeneities creating image distortions. The ear canals and sinuses are typical regions with high susceptibility artifacts resulting in signal loss. The first approach to correct for the distortions is to estimate a ΔB_0 field map and compute the resulting distortion and use it to correct the image. The second method consists in acquiring a volume with an inverted phase encoding direction than the functional acquisition. This image will be distorted in the opposite direction. From both phase encoding directions it is possible to recover an undistorted image which is in middle between the two (see example fig. 1.3-10 with topup algorithm from [ASA03]).
- *Registration* : In order to compare results between different brains of different shapes and sizes, each volume is normalize to fit into a generic brain atlas [Kle+09].
- *Filtering*: A temporal high pass filter can be used to remove low frequency signal drifts. A spatial Gaussian filter is also employed to ensure the gaussianity of the noise in the signal at the cost of reducing spatial resolution and inflating statistical results.

Statistical inference and General Linear Model

After a task-based fMRI experiment and pre-processing, the temporal signal in each voxel is compared to the onset of the tasks to assess whether the correspond brain area is involved in the task. More precisely, the detection of BOLD signal in fMRI exploits the General Linear Model [WF95], which describes the temporal signal of the voxel I with a design matrix D containing the explanatory variables such as the onsets of the stimuli convolved with a canonical hemodynamic response function and motion correction regressors. The GLM fit is formulated as

$$I = D\beta + \varepsilon \tag{1.38}$$

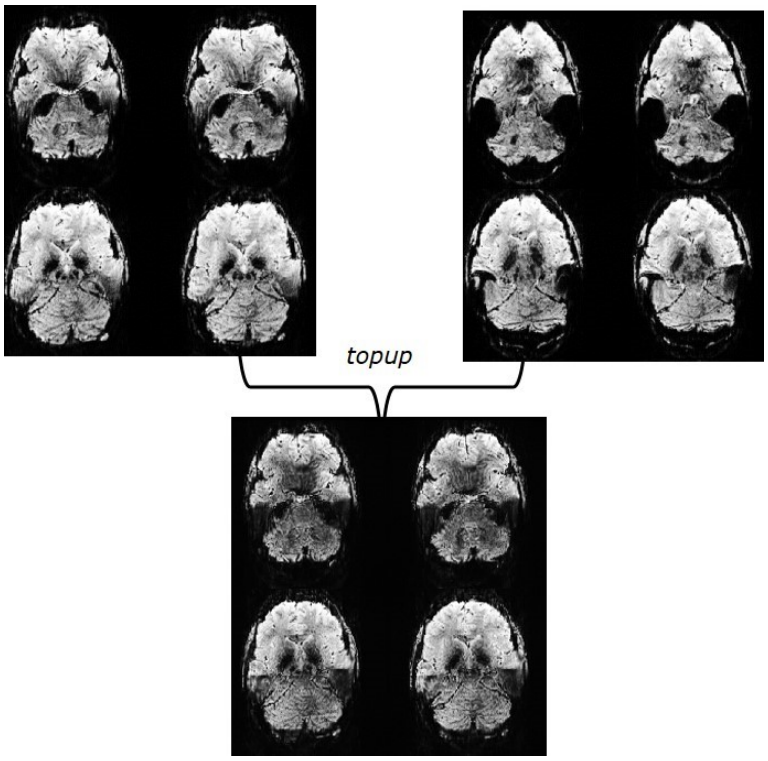

Figure 1.3-10: **An example of distortion correction**: illustrated here the method using two scans of opposite phase encoding direction. The correction is performed with the topup algorithm [ASA03] from the FSL library (FMRIB, Oxford UK).

with β, the regression coefficients estimated via least squares method and ε the residual of the estimation assumed to follow a centered Gaussian distribution. Their expressions are

$$\beta = (D'D)^{-1}D'I \tag{1.39}$$

$$\varepsilon = I - D\beta \tag{1.40}$$

where Id is the identity matrix and D^+ is the pseudo inverse of D. The typical method to infer on neuronal activity uses t-score statistics to assess the significance of a set of explanatory variables on the signal. For each test, a question regarding the size effect of an element of the model has to be specified. These questions are expressed by the use of contrasts c which are vectors that are multiplied by the estimates β. For example the contrast $c = (1\,0\,\cdots\,0)'$ tests if the first regressor has a positive effect on the signal. The expression of the t-score of the test is

$$t = \frac{c'\beta}{\sigma_\varepsilon \sqrt{c'(D'D)^{-1}c}} \tag{1.41}$$

with σ_ε the standard deviation of the residual signal. t follows a Student's t-distribution with $\nu = N - n$ degrees of freedom with N the number of observations and n the number of regressors. fMRI data generally counts more than 100 repetitions, thus the t-distribution can be approximated with a Gaussian distribution of zero mean and variance equal to one if the number of explanatory variables in practice is less than $N - 30$. The scores are then

thresholded by a p-value and overlaid on an anatomical image.

* * *
* *
*

Chapter 2

Imaging the brain at high resolution

Chapter Outline

2.1 Stakes and challenges of high resolution imaging 27
2.1.1 Spatial resolution vs Acquisition time vs SNR 28
2.1.2 Parallel imaging 29
2.1.3 High resolution fMRI 31
2.2 Benefits and challenges of ultra high field imaging 32
2.2.1 Increased SNR and increased BOLD CNR 32
2.2.2 B0 and B1 effects 34
2.3 Tackling RF transmit field inhomogeneities at ultra-high field 36
2.3.1 Parallel transmission free approach 37
2.3.2 Parallel transmission approach 38

Functional MRI needs high spatial resolution to explore in more details cortical structures. On the other hand, other brain regions are also investigated such as the cerebellum, the basal ganglia or the brain stem that are notoriously harder to acquire due to their small size, or the signal drop-outs they suffer because of the susceptibility and B_1 artifacts.

In this chapter, we first describe the link between SNR, acquisition time and spatial resolution. We then describe parallel imaging and its role in high resolution imaging with a limitation to Cartesian and 3D imaging. Next, we will introduce the benefits of ultra-high field imaging to fMRI and the challenges that come with it. Finally, we will describe specific parallel transmission RF pulse design techniques that are used to overcome these challenges.

2.1 Stakes and challenges of high resolution imaging

One of the most important quality criteria for any image is its resolution which is defined by the minimum distance at which two objects can be distinguished. In the case of MRI, image resolution comes with a sacrifice in acquisition time and/or SNR. In functional MRI and with the current gradient systems, acquisition time of an entire 3D volume remains too long. This acquisition time if often reduced at the cost of a lower signal to noise ratio (SNR). The SNR is defined by

$$SNR = \frac{S}{\sigma} \tag{2.1}$$

with S the signal amplitude and σ its fluctuations (noise). Several methods for SNR measurement are available. The most straightforward method consists in computing the ratio of the mean values of a small Region of Interest (ROI) located on the sample and a standard deviation (corrected from Rician distribution if performed on magnitude image) from a ROI in the background. Despite its simplicity it lacks reliability when used in MRI images, it is highly sensitive to the location of the ROI and the presence of ghosting in the background can bias the estimation of noise. When it is weak, SNR is typically considered equal to the temporal SNR (tSNR) [KG01] which is computed from an acquisition of multiple repetitions with the ratio of the temporal mean of the voxel value and its standard deviation. A more simple but still reliable approach consists in computing the voxel-wise temporal mean term using the repetitions and computing the σ term from the spatial standard deviation of a noise only image. The noise image is obtained by setting the transmit voltage to zero. The noise term has to be corrected from the bias due to its Rician distribution in magnitude images and also by the number of receive coils in the case of multi-receive RF coils [CAM97].

2.1.1 Spatial resolution vs Acquisition time vs SNR

Setting a high resolution fMRI protocol can be challenging because the user must set up the desired spatial resolution and the right TE without sacrificing SNR and acquisition time.

After RF excitation, an echo is acquired. A gradient readout performs a frequency encoding while the Analog to Digital Converter (ADC) is switched on during the gradient readout to measure and convert the signal. The ADC is open for a duration T_s, the sampling time. Depending on the size Field Of View (FOV), the echo is decomposed into multiple sample points that are acquired for a duration D, the dwell time. For an image matrix of size N_s in the frequency encode direction, we thus have $T_s = N_s D$. The receive bandwidth is defined by

$$BW_{receive} = \frac{1}{D} \tag{2.2}$$

On the other hand, there is an inverse relation between the FOV, the pixel size (i.e resolution), the Fourier domain sample size Δk and the k-space FOV defined by $k_{FOV} = 2k_{max} = N\Delta k$ defined by

$$\Delta k = \frac{1}{FOV} \tag{2.3}$$

$$\Delta x = \frac{1}{k_{FOV}} \tag{2.4}$$

From 1.24, Δk can also be expressed as

$$\Delta k = \gamma G_{readout} D \tag{2.5}$$

therefore,

$$\Delta x = \frac{1}{\gamma G_{readout} N D} \tag{2.6}$$

For a fixed matrix size and readout gradient, we can see here that resolution can increase by increasing the dwell time.

The SNR in a given voxel is proportional to the volume of the voxel, the square root of the number of samples and the dwell time

$$SNR_{voxel} \propto \Delta x \Delta y \Delta z \sqrt{N_x N_y N_z D} \tag{2.7}$$

This expression shows that an increase in SNR comes at the cost of spatial resolution and acquisition time.

2.1.2 Parallel imaging

Using an RF coil with multi receive channels has allowed the use of techniques reducing drastically the acquisition time without compromising the SNR too much. The acceleration comes from the fact that part of k-space is not acquired. This acceleration is described by the *reduction factor* $R \in \mathbb{N}$ meaning that only one data point out of R is acquired. Reconstructing data from such under sampled k-space results inevitably in aliasing. However, with prior knowledge of receive sensitivity, it is possible to recontruct an unaliased image.

Undersampling can be beneficial to the EPI technique because it reduces the loss of signal due to T_2^* decay and the length of the echo train resulting in less distortions.

There a two commercially available parallel imaging techniques, SENSE and GRAPPA.

SENSE versus GRAPPA

Sensitivity encoding (SENSE) [Pru+99] uses prior knowledge of coil sensitivities to 'disentangle' folded voxels. It relies on the fact that the aliasing is dependent on the reception (or sensitivity) profile of each reception coil.

After having performed an under sampled acquisition followed by a reconstruction, an aliased image per reception channel is obtained. Knowing the sensitivity of each coil, it is possible to build a sensitivity matrix S of size $N_c \times N_p$ (N_c the number of channels and N_p the number of superimposed voxels) that contains for one column, the contribution in the aliasing of each receive channel. We have thus

$$SI = A \tag{2.8}$$

with I vector of size N_p containing the separated pixel values and A vector of size N_c of aliased pixel values for each coil. The unfolded image is then recovered with least squares method

$$I = (S^H \Psi_0^{-1} S)^{-1} S^H A \tag{2.9}$$

With Ψ the noise covariance matrix ($N_c \times N_c$). This procedure is repeated for each voxel to recover the true image.

Generalized Autocalibrating Partially Parallel Acquisitions (GRAPPA) [Gri+02] performs an estimation of the missing k-space data points (target point) before the inverse Fourier transform reconstruction step yielding thus an unaliased image. In this method, missing k-space points are estimated from the dot product of acquired neighboring points (source points) and precomputed weights. The k-space area containing source points is commonly referred as kernel. The estimation is simply performed by a matrix product

$$X = WK \tag{2.10}$$

with X vector of size N_c containing the estimated missing k-space points for a given kernel, K a vector matrix of size $N_k = N_c N_s$ containing all sampled k-space points in the kernel. N_s is the number of source points in the kernel for each receive coil. The weights are obtained from auto-calibration scans (ACS) performed typically at the beginning of the acquisition.

Therefore, in opposition to SENSE, no sensitivity profile is required. ACS is a portion of k-space (generally the central lines of the k-space) that is fully sampled on which the weights are learnt. Weights are thus defined by

$$X_{ACS} = WK_{ACS} \tag{2.11}$$

with the X_{ACS} the k-space point acquired in the ACS scans (the same will be skipped further in the acquisition) and K_{ACS} k-space points from the ACS scans that are in the kernel. Finally W is estimated via least-squares method

$$W = X_{ACS}K_{ACS}^{H}(K_{ACS}K_{ACS}^{H})^{-1} \tag{2.12}$$

In the end, GRAPPA and SENSE techniques in their simplest forms are mathematically similar except that the first one is performed in the image domain while the latter is performed in the Fourier domain.

The GRAPPA method is performed on the sub image reconstructed from each receive channel, the sub images are then combined by computing the Sum of Squares (SoS) (Roemer et al 1990) of each sub image

$$I_{SoS} = \sqrt{S^{H}S} \tag{2.13}$$

Noise enhancement

These techniques are limited by a white noise enhancement depending on the amount of acceleration and the coil design. The acceleration comes with a penalized SNR [Pru+99] expressed by

$$SNR = \frac{SNR_0}{g\sqrt{R}} \tag{2.14}$$

with SNR_0 the signal-to-noise ratio for a fully sampled k-space, R the acceleration factor and g the geometry factor scaling larger than 1 quantifying the influence of receive coil disposition and their intrinsic receive sensitivity profiles. On one hand, the more accelerated the acquisition is and the stronger is the aliasing artifact, on the other hand, the coil geometry has an influence on the conditioning of the SENSE and GRAPPA equations. More precisely, these methods rely on linear algebra with a matrix inversion for the estimation of the missing k-space samples or the unaliased image. The conditioning of the equations has an important influence on the inversion and small signal variations (i.e. noise) can be amplified. The conditioning is typically determined by the similarity between each equation, which can be here materialized by receive channels with sensitivity profiles that are too similar. Moreover, reduced FOV acquisition decreases the number of coils actually receiving a significant amount of signal limiting the conditioning of the equations. Generally, a g-factor under 1.2 is considered as tolerable. Because of these penalties, acceleration factors rarely exceed 3 along one phase encoding direction if they are not used with controlled aliasing methods.

Controlled aliasing in parallel imaging

Actually, the g-factor is also dependent on other parameters such as the coil loading, the FOV and importantly, the sampling pattern. The aliasing depends on the under sampling pattern, and the stronger the aliasing the stronger the noise penalty.

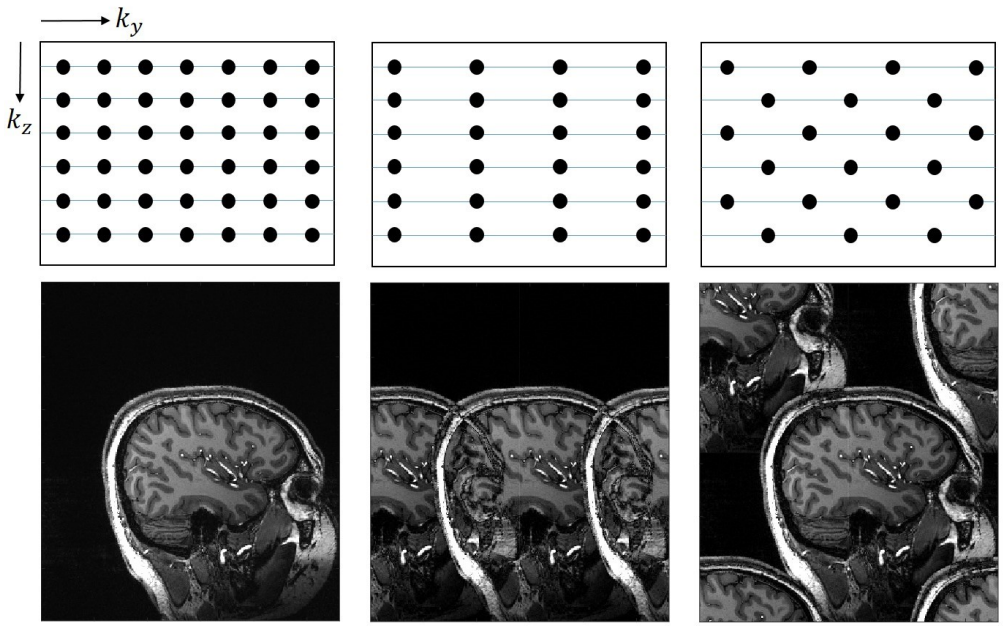

Figure 2.1-1: **Fully sampled k-space compared to aliasing from GRAPPA and CAIPIRINHA for an acceleration factor of 2**: From left to right, fully sampled k-space, GRAPPA sampling, CAIPIRINHA sampling scheme. In bottom the corresponding reconstructed image. Aliasing is less severe with CAIPIRINHA than GRAPPA.

Originally introduced to improve simultaneous multi slice imaging reconstruction, CAIPIRINHA [Bre+06] consists in modifying the under sampling pattern to reduce aliasing and by the same token, improve the conditioning of the SENSE/GRAPPA inversion. Figure 2.1-1 shows the reduced aliasing brought by CAIPIRINHA compared to GRAPPA for the same acceleration factor. In the case of 3D imaging, 2D-CAIPIRINHA distributes the under sampling in phase and partition encoding directions leading to the so called controlled aliasing in the image domain. Consequently, the g-factor is reduced allowing thereby higher acceleration factors.

Since the original publication, the method has seen multiple evolutions, the first one was the blipped-CAIPIRINHA [Set+12] which used gradient blips instead of phase shifts for aliasing control. An alternative named wave-CAIPIRINHA [Bil+15] adds sinusoidal gradients in phase and partition during gradient readouts to generate a spring shaped readout trajectory. This allows to spread the under sampling to the readout dimension reducing further the g-factor and enabling even higher accelerations. More recently the skipped-CAIPIRINHA [SS21] approach enables greater protocol flexibility by allowing a segmentation of the blipped CAIPIRINHA trajectory, keeping the same under sampling pattern but changing the trajectory.

2.1.3 High resolution fMRI

Despite the speed of the EPI and the various acceleration methods, it remains difficult to scan a whole brain at sub millimeter resolution while respecting all the sequence settings criteria for an fMRI scan. Although reaching a high spatial resolution is possible, the gradient limitations do not allow having an acquisition fast enough to reach the required echo time of 25ms (for 7T fMRI) or/and volume acquisition time lower than 2 seconds. Indeed, the current gradient systems (on Siemens conventional 7T and on the 11.7T MRI) allow a maximum

amplitude of 70 mT.m^{-1} and a slew rate of 200 mT.m^{-1}.ms^{-1}. Moreover, employing massive acceleration factor (with $R \geq 8$) would eventually help meeting all these criteria but at the cost of increasing noise penalty. Therefore, we opted to focus the work on slab-selective RF pulses to allow smaller FOV and thus reduce the acquisition time. Typically, the scan will be performed on a judiciously positioned slab instead of a FOV covering the full brain. Furthermore, this also alleviates the logistical problem of high volume data management problem raised by high resolution scans.

2.2 Benefits and challenges of ultra high field imaging

Ultra-high field (uhf) MRI refers to devices operating at $B_0 \geqslant 7$ Tesla. Installed in 1998, the first 8T system was then followed by more than 70 systems with a few reaching 9.4T and now a unique 11.7T at NeuroSpin. Previously limited to research purposes, 7T MRI machines are now available for clinical applications leading to a likely increase of 7T systems in the coming years.

2.2.1 Increased SNR and increased BOLD CNR

Signal to Noise Ratio

The amount of magnetization depends on the strength of the static field B_0. We have described in the first chapter a relation between both as

$$M_0 = \frac{\rho_0 \gamma^2 \hbar^2}{4kT} B_0 \tag{2.15}$$

with ρ_0 the proton density, γ the gyromagnetic ratio of water, k the Boltzmann constant, the temperature T and of course the magnetic static field B_0. We also saw that the signal is also proportional to the net magnetization. The higher the B_0, the higher the measured signal. This is amplified by Faraday's law of induction which gives an extra factor in the dependence of the SNR versus B_0. SNR relation with B_0 field has been subject to early investigation, Hoult for example simulated the B_1 field and noise on a spherical water phantom at different field strengths [HP00]. He showed analytically that the image profile gets less homogeneous towards higher magnetic fields. In more recent work [PSS16], SNR measurements were performed at 3, 7 and 9.4T with RF coils of similar designs showing a supra linear gain in SNR with field strength. Moreover, the concept of ultimate intrinsic SNR [OA98] provides an upper bound of coil design and therefore a theoretical limit at a given B_0 field. Shortly after, Guerin and al. [Gue+17] proposed a uiSNR in a realistic head model. They confirmed the supra linear relation between SNR and field strength but also showed that minimum achievable g-factor (ultimate g-factor) decreases with $B_0 \geq 7$. This could be explained by the fact that sensitiviy maps become more complimentary as field strength increases. More generally, the SNR increase is supposed to be the strongest in the center of the head.

Sensitivity and Specificity

fMRI has been from the start a major motivation for ultra-high field imaging. Since fMRI analysis often consists in a voxel wise temporal signal processing, the tSNR is often considered

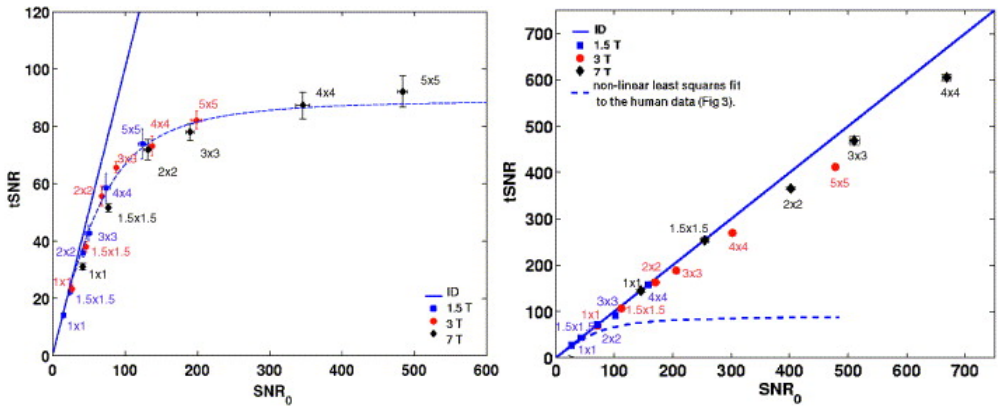

Figure 2.2-2: **tSNR versus SNR plot.** Different voxel sizes and magnetic fields are used. On the left, for an in vivo experiment and on the right on phantom. The physiological noise provokes a stalling of the tSNR at very high SNR. From [Tri+05].

as quality measure. It is defined by

$$tSNR = \frac{\bar{S}}{\sigma} \tag{2.16}$$

with $\bar{S}$ the temporal mean of the voxel and σ its standard deviation. tSNR therefore defines the stability of the signal overtime. Following Krueger and Glover's model [KG01], the noise term can be viewed as the quadratic sum of thermal noise and physiological noise. The thermal noise is originating from the electronics that can be represented as a white noise whose fluctuations follow a Gaussian distribution. The physiological noise refers in this model to the fluctuations originating from the patient (like breathing) and is generally proportional to signal strength. At low signal strengths, the tSNR is equal to the SNR and the noise is dominated by its thermal component. However, higher SNR comes with higher physiological noise leading to a saturation of the tSNR. Figure 2.2-2 from [Tri+05], shows experimentally the stalling of tSNR at very high SNR. This relationship is expressed by

$$tSNR = \frac{SNR}{\sqrt{1 + \lambda^2 SNR^2}} \tag{2.17}$$

with lambda a term quantifying the effect of physiological fluctuations [KG01; Tri+05].

Along an increased SNR at higher B_0, the functional contrast-to-noise ratio (fCNR) is also higher. Definition of fCNR is diverse throughout the literature, but the most common one is

$$fCNR = \frac{A}{\sigma_{noise}} \tag{2.18}$$

with A the amplitude of the activation and σ_{noise} the standard deviation of the noise. One can also refer simply to the percent signal change relative to the mean of the signal [WR13]. The signal change represented by A is typically of only few percent of the overall signal amplitude.

The BOLD signal change occurs when the relative concentration in deoxyhemoglobin in the blood changes, which is measured via the local change in magnetic susceptibility. All susceptibility effects increase with field strength. The influence of intravascular blood is limited at higher fields because its T_2 decay is also shortened much more than the extravascular T_2 leaving room for the BOLD signal to be detected more easily [UMU09]. An increase

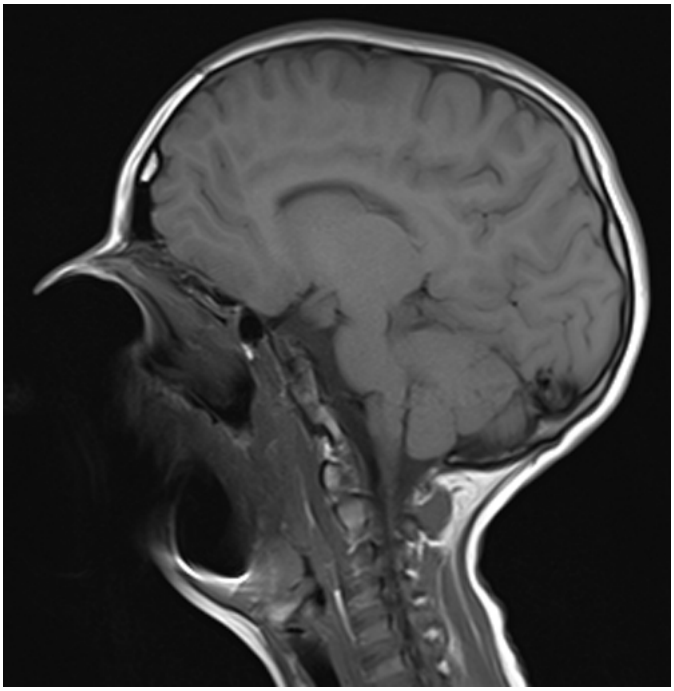

Figure 2.2-3: **Extreme susceptibility artifact due to braces.** From mriquestions.com.

of the functional contrast has been experimentally demonstrated [Yac+01; Zwa+09]. This increase in contrast can be invested in increasing spatial or temporal resolution. Moreover, increasing the spatial resolution has two benefits. First, it can improve functional specificity by reducing the undesirable influence of venous blood with partial volume effect. Second, increased spatial resolution will also put the signal in a thermal noise dominated regime benefiting the fCNR [OY11].

2.2.2 B0 and B1 effects

Benefits of ultra-high field come also with technical challenges.

Magnetic susceptibility

Noted χ, magnetic susceptibility measures the extent of a tissue to be magnetized when placed in a magnetic field. Most tissues are diamagnetic while air is slightly paramagnetic, iron for exemple is paramagnetic. As mentioned in the previous paragraph, susceptibility effects are increased by the magnetic field and can be either an opportunity like in fMRI with BOLD signal or be undesirable. More precisely, susceptibility creates field distortions because of changes in precession frequency of the sample leading to a wrong spatial encoding of the MR signal. The resulting artifact is characterized in the image by spatial distortions and signal loss. An example of such artifact is displayed in figure 2.2-3. The EPI sequence is particularly sensitive to it because during its long readout spins have more time to dephase. Anatomical regions around the sinuses, the ear canals or lungs are notoriously hard to image because of the presence of air. Quantification of these inhomogeneities is performed via ΔB_0 mapping sequences. Susceptibility effects can be alleviated by scanning at shorter TE, so spins have less time to dephase or by using spin-echo instead of gradient echo technique.

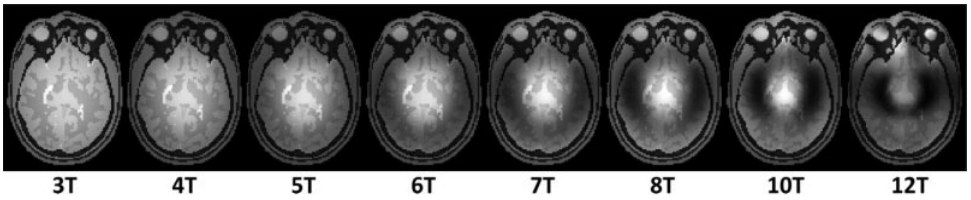

Figure 2.2-4: **Simulated B_1 inhomogeneities effect with field strength.** Simulated gradient echo with a birdcage coil [WC10].

B1 inhomogeneities

The B_1 field is increasingly inhomogeneous at higher magnetic field (see fig. 2.2-4). Indeed, at ultra-high field the RF wavelength λ is of the same order as the human head or torso leading to a dielectric effect of the B_1 field [Yan+02]. Figure 2.2-5 shows the wave effect in vivo on 7T compared to 3T. With a typical coil (birdcage for example) the production of the B_1 field generates electric currents in the sample. If the sample is symmetric (e.g. the brain), then constructive interferences occur at the center of the sample and destructive interferences at roughly $1/4$ of the RF wavelength [WC10]. Moreover, the attenuation of the RF amplitude due to the conductivity shortens even more the wavelength, thereby worsening the effects [Yan+02]. The expression of the wavelength λ of an electromagnetic wave in a medium of relative permittivity ϵ_r and magnetic susceptibility χ:

$$\lambda = \frac{c}{f_0\sqrt{\epsilon_r(1+\chi)}} \tag{2.19}$$

With c the speed of light in vacuum. Permittivity is a depends on the conductivity of the medium and the frequency of the RF wave. Typically, if we consider an average human head of 14 cm wide with a weak susceptibility ($\chi = 0.5e-6$) and a relative permittivity ϵ_r of 68 at 1.5T and 45 at 7T [GSC96] we get $\lambda_{3T} \approx 56cm$ and $\lambda_{7T} \approx 15cm$. This puts the destructive interference at $14cm$ so right at the outskirts of the head at 1.5T and 3.75 cm, roughly near the middle of each brain hemisphere at 7T.

Specific Absorption Rate

Energy deposition for the RF excitation also needs to be considered. In order to apply a given flip angle to the spins, energy is emitted and part of it is absorbed by the sample, converting into heat. This can be measured by the Specific Absorption Rate (SAR) and its units are watts per kilogram. SAR is determined by the time average of the instantaneous energy deposition:

$$SAR(r) = \frac{1}{T}\frac{\sigma(r)}{\rho(r)}\int_0^T \|E(r,t)\|_2^2\,dt \tag{2.20}$$

with E the RMS electric field produced by the RF coil, σ the electrical conductivity and ρ the density of the sample and the time of integration T. SAR is strictly regulated for mobile phones and MRI. Because σ and ρ can significantly change from one tissue to another and the electrical field is not necessarily uniform, the International Electrotechnical Commission (IEC) has specified in its guideline IEC 60601-2-33 (also adopted by the FDA) that the SAR should be controlled globally over the sample as well as locally over 10g (or 1g) of tissue. Moreover, different limitations are given depending on the level of supervision and risk (normal, first level and second level modes).

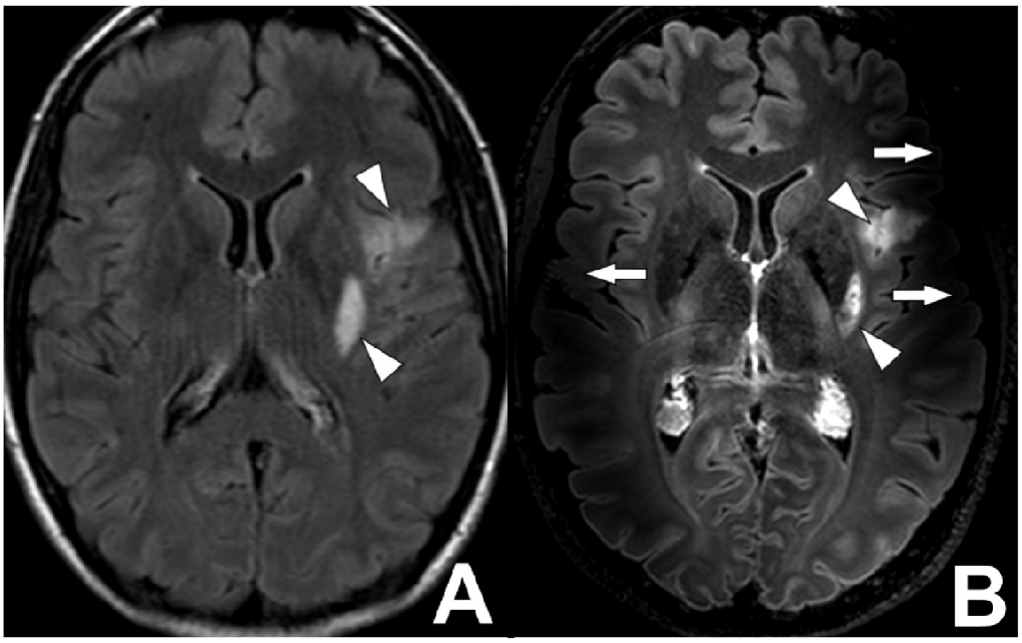

Figure 2.2-5: B_1 **inhomogeneities 3T versus 7T in vivo.** Same patient suffering from ischemic stroke (arrow heads) scanned at 3T (A) and 7T (B) with a FLAIR sequence. Despite slight differences in protocol settings signal dropouts are clearly visible on the temporal regions for the 7T scan (arrows). From [De +18].

Table 2.1: SAR limits as defined by the IEC, the limit for the partial body global SAR depends on the ratio exposed patient mass and patient mass.

	Global SAR (W/kg)			**Local SAR 10g (W/kg)**		
Operating Mode	Whole body	Partial body	Head	Trunk	Extremities	Head
Normal	2	2-10	3.2	10	20	10
1st level	4	4-10	3.2	20	40	20
2ns level	>4	>(4-10)	>3.2	>20	>40	>20

Since the early days of MRI, scanning at fields higher than 0.24T was considered as unlikely to happen because RF depth penetration was considered as insufficient [HL79]. According to the authors this limit was explained by the current imaging techniques relying on the acquisition of the magnitude FID instead of a symmetric echo and the perceived difficulty to design an RF coil for 10Mhz excitations (corresponding to 0.24T) and above [HP00]. Robitaille et al. successfully scanned in 1998 an in vivo brain at 8T with a gradient echo sequence [Rob+98]. The RF pulses used to perform a 90° flip angle excitation required only 0.085J instead of the 2J expected. Cao et al. [Cao+15] performed a comparison of SAR distribution in simulation for a 90° pulse performed at magnetic fields from 1.5T to 14T. They show a less than quadratic relationship between SAR and B_0 confirming Robitaille et al. results. Figure 2.2-6 shows the local SAR distribution on the brain at different frequencies. At higher frequencies, the energy deposition focuses at the center of the brain.

2.3 Tackling RF transmit field inhomogeneities at ultra-high field

At ultra-high field MRI, B_1 inhomogeneities related artifacts become severe. In order to tackle this problem, parallel transmission has been introduced. Figure 2.3-7 illustrates

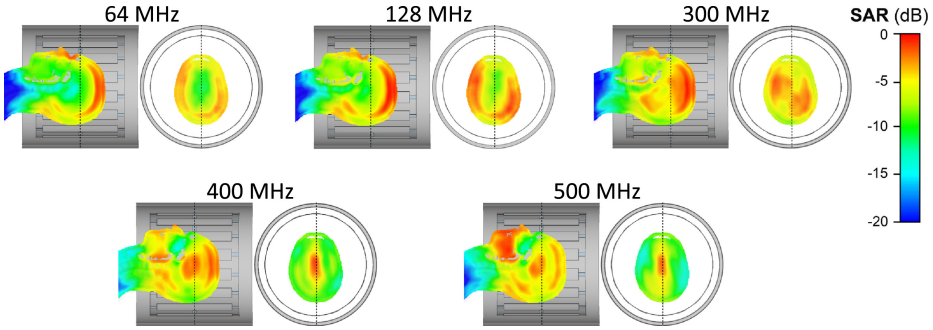

Figure 2.2-6: **Local SAR distribution for different frequencies.**: 10g SAR distribution for a birdcage coil in CP mode. SAR focuses in the center of the sample at frequencies. From Fiedler et al. [FLB18].

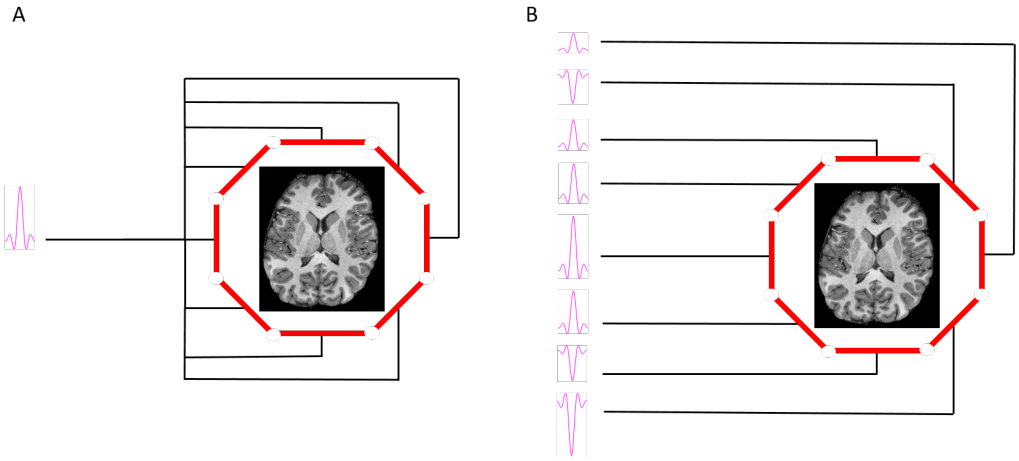

Figure 2.3-7: **Conventional versus Parallel transmission.** Conceptual differences between conventional transmission (A) and parallel transmission (B). In conventional transmission the same RF pulse is amplified and splitted between channels. In parallel transmission, each transmission channel can be driven independently.

the conceptual difference between conventional and parallel transmission. When using a multi transmit RF coil, the RF excitation is programmed independently for each channel, in amplitude and phase through time, resulting in more degrees of freedom for RF pulse design and B_1^+ field control. Currently, most MRI vendors propose 2 channels transmit RF body coils on their 3T systems.

B_1^+ field homogeneity is often assessed via flip angle measurements. A common metric measuring flip angle homogeneity is the Normalized Root Mean Square Error (NMRSE) defined by:

$$NRMSE = \frac{\sqrt{\frac{1}{N}\sum_{v=1}^{N}(FA_v - FA_{target})^2}}{FA_{target}} \tag{2.21}$$

with FA_v the flip angle yielded by the RF excitation for the voxel v, FA_{target} the target flip angle and N the number of voxels considered.

2.3.1 Parallel transmission free approach

RF field inhomogeneity is a long standing problem for which many methods not requiring parallel transmission have been developed.

- *Adiabatic pulses*: These pulses are insensitive to B_1^+ field inhomogeneities. They consist in a gradual variation of the frequency around ω_0 of the RF. If these changes are slow enough the magnetization $\overrightarrow{M}$ follows the effective magnetic field $(\overrightarrow{B_0} + \overrightarrow{B_1})$ experienced by the spins during the frequency sweep [TG97].

- *Dielectric pads*: Dielectric pads are small pouches filled with dielectric materials. Because of their electrical properties, they can distort and shape the B_1^+ field distribution. Practically, their very high permittivity alters the B_1^+ field wavelength (see eq.2.19) reducing the shadow areas in the image if judiciously placed [Yan+06; Web11]

- *Dedicated RF coils*: RF coil engineering proposed several solutions for high frequency RF coil. For example, Alsop and colleagues [ACM98], designed a spiral shaped RF coil and demonstrated in vivo higher B_1 homogeneity at 4T compared to a conventional birdcage RF coil.

When optimizing a pulse, the resulting flip angle is the result of the total rotation of the magnetization overtime. Methods optimizing B_1 fields to manipulate the magnetization rely on solving Bloch equations making the implementation of optimization algorithms difficult. However, Pauly et al. [PNM11] demonstrated that assuming a small tip angle of the magnetization the transverse magnetization M_{xy} can be simplified as

$$M_{xy} = i\gamma M_0 \int_k W(k)S(k)e^{ixk}\,dx \tag{2.22}$$

where $W(k)$ is a weighting function and $S(k)$ a spatial frequency sampling function derived from the trajectory in the k-space wich is introduced here as

$$k(t) = -\gamma \int_t^T G(\tau)\,d\tau \tag{2.23}$$

It is interesting to note that the integration interval is different from Eq.1.24 for the transmission case.

This result has been applied by Saekho et al. [Sae+06] for RF pulse design. They used the small tip angle approach to optimize series of multiple slice selective RF pulses for a gradient trajectory for localized k-space "spokes" (also called fast-k_z pulses) along z and crossing the $k_x - k_y$ plane. In this framework, one spoke is equivalent to a classic selective pulse, the "multi-spoke" approach allowed an increased number of degrees of freedom for the pulse optimization. Overall, the optimized pulses were spatially selective and yielded a higher field homogeneity than the classic slice selective pulse. These RF pulses were penalized by B_0 inhomogeneity because of their overall duration.

2.3.2 Parallel transmission approach

Static RF shimming

One of the first application of parallel transmission for B_1^+ homogeneization is called static RF field shimming. It consists in optimizing the RF amplitude and phase on the different channels to yield the most homogeneous B_1 transmit field. The RF waveform remains the same between channels. The RF coefficients are computed via an optimization problem approach by minimizing a cost function subject to SAR constraints. Mao et al. [MSC06]

explored the limits of static RF shimming in simulation modelling a 16 and 80 channel transmit array design at 300MHz ($\sim 7T$) and 600MHz ($\sim 14T$) on a 3D human head model of 23 different tissue types and their own electrical properties. Single slices were homogenized successfully at both frequencies but at the cost of very bad signal on other slices. The 80 transmit design showed better performance because of the higher degrees of freedom provided by the high number of channels. However, the method fails for an optimization on the whole brain with signal dropouts around 10% at 300MHz and even 40% at 600MHz.

Other approaches takes into advantage the wave behavior of the B_1 field to improve its homogeneity. Time Interleaved Acquisition of Modes (TIAMO) by Orzada and colleagues [Orz+10] is a technique using a couple of RF pulses with different B_1 excitation modes. By choosing conveniently a pair of complementary RF pulses yielding a complementary excitation pattern (and complementary B_1 artifact pattern), they combined both images to get a homogeneous image. Because this method supposes a doubling of acquisition time, they applied a GRAPPA acceleration of two to have no extra scan time compared to conventional acquisition schemes.

Transmit SENSE

Using the small tip angle approximation combined with the combination of parallel transmission and the knowledge of transmit sensitivity profiles, Katscher et al. [Kat+03] optimized pulses to get tailored excitation for a desired excitation profile $P_{des}(x)$. They defined the problem as

$$P_{des}(x) = \sum_{n=1}^{N_c} S_n(x) P_n(x) \tag{2.24}$$

with N_c the number of transmit channels, S_n the sensitivity profile of transmit channel n and P_n its spatial excitation pattern. The problem can then be transposed into the Fourier domain

$$p_{des}(k) = \sum_{n=1}^{N_c} S_n(k) * P_n(k) \tag{2.25}$$

P_n and S_n are concatenated as s_{full} and p_{full} so the previous equation becomes

$$p_{des}(k) = s_{full} p_{full} \tag{2.26}$$

p_{full} is then determined through a regularized matrix inversion of s_{full}. Because of its similarity with SENSE, this technique is called transmit SENSE. The method enabled them to have either shorter pulses, or a more homogeneous flip angle profile within a chosen region of interest.

k_T-points and Universal Pulses

Inspired from the k_z-spokes, Cloos et al. [Clo+12] extended the approach to 3D excitation and with the use of parallel transmission. The k_T-points technique consists in optimizing an RF pulse where k-space points are optimized with a multi-pulse RF. The optimization benefits from the shape of these pulses which cumulates degrees of freedom from the number of RF sub-pulses (the number k_T-points), from the number of transmission channels and the 3D position of the $k_T - points$ in k-space. Unlike the k_z-spokes where the k-space points positions are optimized only in 2D for a 2D excitation, the k-space points locations are

optimized over the 3D k-space for a better flip angle homogeneity. The pulse shape consists in a cascade of RF square shapes and k-space displacements (see example fig. 2.3-8). The k_T-point optimization problem is formulated as

$$\min_{x,k} \|A(x,k) - \alpha_t\|_2,\ (x,k) \in \mathbb{C}^{N_c N_{kT}} \times \mathbb{R}^{3N_{kT}} \tag{2.27}$$

$$s.t.\ c_G(x) \leq SAR_{G,max} \tag{2.28}$$

$$s.t.\ c_{10g,m}(x) \leq SAR_{10g,max}, 1 \leq m \leq N_{VOPs} \tag{2.29}$$

$$s.t.\ c_{Pw,n}(x) \leq P_{\max},\ 1 \leq n \leq N_c \tag{2.30}$$

$$s.t.\ |x_j| \leq V_{\max},\ 1 \leq j \leq N_c \times N_{kT} \tag{2.31}$$

where x are complex RF coefficients, k contains k-space positions, A the Bloch operator returning the flip angle generated from the RF and gradients corresponding to x and k, α_t the target flip angle, N_c the number of transmit channels and N_{kT} the number of k_T-points. The optimization problem is subject to several constraints [Hoy+14; Dup+15; Gra+15]. 2.28 is the global SAR constraint, 2.29 is the 10g local SAR constraint which is expressed via the virtual observation point (VOP) compression method as a set of N_{VOP} SAR matrices [EG11; Lee+12]. In order to preserve the RF coil from warming up and drifting, an average power limit $P_{\max}$ is also applied. Finally, 2.31 represents the maximum peak voltage $V_{\max}$ for each transmit channel allowed by the coil manufacturer. The flip angle yielded by x and k is computed via a Bloch simulation and requires B_1^+ maps. ΔB_0 maps are also taken into account to taken into account off-resonance. Acquisition of ΔB_0 and B_1^+ maps represent non-negligible extra scan time during an MR session. More time is also required to compute the pulse and load it into the sequence.

Thankfully, there is relatively limited inter subject variability of ΔB_0 and B_1^+ profiles. This represents an opportunity to employ a k_T-points pulse approach which can be robust to inter subject differences, and mitigate the RF field inhomogeneity problem on a large population. One can then optimize a pulse on a group of subjects yielding thereby a 'universal' solution. The problem is redefined as

$$\min_{x,k}(\underset{1\leq i\leq N_s}{mean} \|A_i(x,k) - \alpha_t\|_2),\ (x,k) \in \mathbb{C}^{N_c N_{kT}} \times \mathbb{R}^{3N_{kT}} \tag{2.32}$$

with N_s the number of subjects in a database of field maps representative of a population. The constraints remain the same. In this framework the returned solution is less optimal than a subject specific tailored k_t-point pulse but yet yields significantly better NMRSE than RF shimming [Gra+17b] and single channel excitation. The advantage of Universal Pulses compared to tailored approaches is that they require no extra scan and requires no online pulse design thus simplifying imaging protocols and optimizing scanner time.

* * *
* *
*

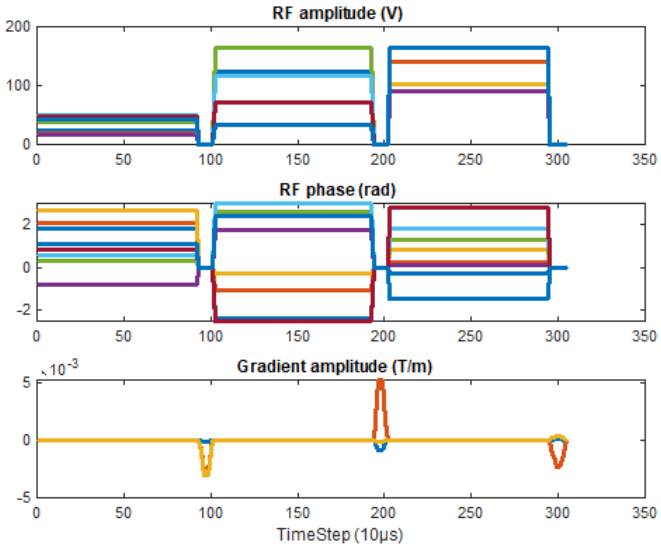

Figure 2.3-8: **Result of a 3 k_t-points design.** On the right RF amplitude, phase (each color represent a different transmission channel) and gradients blips (each color represent a gradient). On the left, k-space trajectory yielded by the gradient blips.

Part II

Methodological Developments

Chapter 3

RF pulse design

Chapter Outline

3.1 Slab selective Universal pulse design 46
3.1.1 Theory and method 46
3.1.2 Results 48
3.1.3 Discussion 48
3.2 Gradient delay correction 51
3.2.1 Introduction 52
3.2.2 Theory 52
3.2.3 Methods. 54
3.2.4 Results 56
3.2.5 Discussion and Conclusion 58

The first part of this chapter shows how slab selective Universal Pulses are generated from classic Universal Pulses followed by a demonstration of their performance via Bloch simulation as well as an experimental validation on phantom at 7T. We motivate the need of using bipolar over unipolar gradient shapes with Bloch simulations along a comparison with RF shimming. Slab-UP yielded a better flip angle homogeneity than RF shimming and bipolar slab-UP outperformed unipolar slab-UP in high susceptibility regions like the ear canals.

Bipolar slab selective multi spoke RF pulses are sensitive to gradient time mismatches. It results in a dephasing of the following RF spokes proportional to the slab-selection gradient amplitude and the distance of the slice center from the magnet isocenter. Accordingly, adding a trim blip along the corresponding gradient axis between the spokes compensates for the same dephasing cancelling the gradient delay effects, regardless of slab position and orientation. Pulses corrected with trim blips greatly reduced gradient delay effects. Moreover, flip angle acquisition performed in vivo with the slab selective UP showed good fidelity with simulations whether corrected with trim blips or not. Unlike time or phase-shifting approaches, this trim-blip-based method applies to all slab scenarios such as slice excitations, slab excitations and anisotropy in the gradient delays.

3.1 Slab selective Universal pulse design

3.1.1 Theory and method

Redefining the UP problem

In order to alleviate RF inhomogeneities, parallel transmission can be employed. As introduced in chapter 2, the k_T-point parametrization allows optimizing a homogeneous flip angle RF pulse. Unfortunately, this tailored approach supposes for the user to perform additional B_0 and B_1 map acquisitions as well as a time dedicated to the optimization. To bypass this problem, we decided to adopt the Universal Pulse approach [Gra+17b] of the k_T-points that requires no extra scan time. Although a pulse optimization can be performed on a specific brain region for an optimal performance, we choose to target a full brain acquisition to get a single RF pulse with a good performance on all brain regions to avoid handling a cumbersome pulse library. Therefore, the RF pulse is optimized using the same algorithm as for Universal pulses [Gra+17b].

Afterwards, getting the slab selective feature consists then simply in a conversion of the pulse shapes into apodized sinc shapes and the addition of a slab-selective gradient shape. The duration of the RF pulses must remain the same in order to introduce no strong bias with ΔB_0. However, for a same flip angle and the same pulse duration, the peak voltage is higher for a sinc pulse than a rectangle shape and the converted pulse can in the end exceed peak voltage and power constraints. The constraints must then take into account the fact that the outputted RF pulse (rectangles) will be converted into sinc shapes. The problem is thus redefined as

$$\min_{x,k}\Big(\underset{1\leq i\leq N_s}{mean}\|A_i(x,k)-\alpha_t\|_2\Big),\ (x,k)\in\mathbb{C}^{N_cN_{kT}}\times\mathbb{R}^{3N_{kT}} \tag{3.1}$$

$$s.t.\ c_G(x)\leq SAR_{G,max}\frac{SAR_{G,rect}}{SAR_{G,sinc}} \tag{3.2}$$

$$s.t.\ c_{10g,m}(x)\leq SAR_{10g,max}\frac{SAR_{10g,rect}}{SAR_{10g,sinc}}, 1\leq m\leq N_{VOPs} \tag{3.3}$$

$$s.t.\ c_{Pw,n}(x)\leq P_{\max}\frac{P_{rect}}{P_{sinc}},\ 1\leq n\leq N_c \tag{3.4}$$

$$s.t.\ |x_j|\leq V_{\max}\frac{\max(rect)}{\max(sinc)},\ 1\leq j\leq N_c\times N_{kT} \tag{3.5}$$

with $SAR_{G,rect}$ the global specific absorption rate of a rectangular pulse of amplitude 1V and $SAR_{G,sinc}$ the global SAR of its sinc version. Similarly, $SAR_{10g,rect}$ and $SAR_{10g,sinc}$ are the local SAR of the rectangular RF shape and its equilavent sinc shape. P_{rect} and P_{sinc} are the average power of the rect RF shape and its sinc equivalent respectivelly. We have $\max(rect)=1$, therefore $\max(sinc)$ is the maximum value of the sinc shape. We see here that optimizing for slab-selective Universal Pulses (slab-UP) has tighter constraints than kT-points because of sinc pulses are more energy-demanding. Generally, the adapted average power and peak voltage constraints were strong enough to prevent the design to exeed the SAR constraints without having to adapt them specificly. In order to obtain a sharp slab profile, the Time-Bandwidth Product (TBP) has to be high. Since pulse duration must remain unchanged, the RF bandwidth must then be higher which result in higher peak voltage and average power constraining even more the optimization. Moreover, higher RF

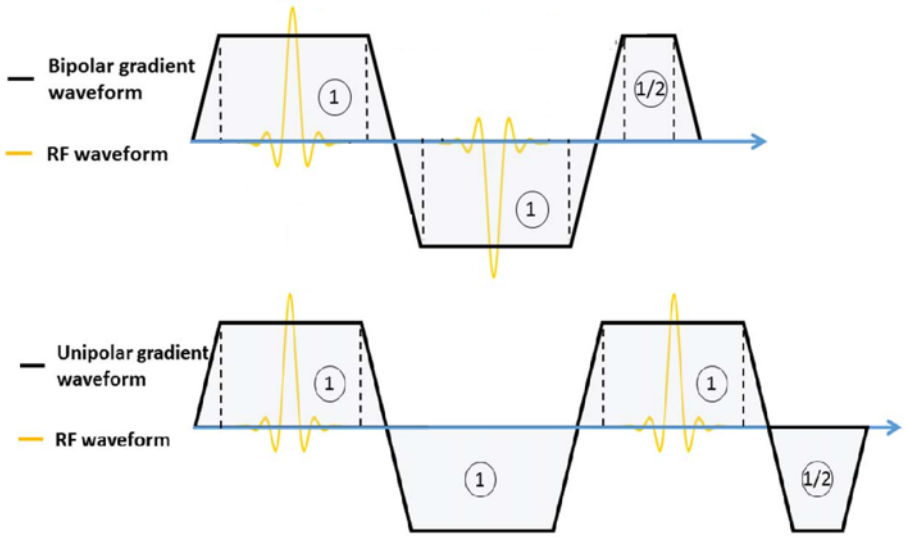

Figure 3.1-1: **Bipolar versus unipolar slab-selective gradient shapes.** The extra rephasing lobe makes the unipolar configuration less time efficient and less robust to ΔB_0 effects.

bandwidth increases the number of lobes on the sinc shape bringing the necessity of shorter sample time than the 10 μs available on the system to play the RF correctly.

There are two possible slab-selective gradient shapes, bipolar and unipolar (3.1-1). For this work, bipolar pulses were privileged for their shorter duration making them more robust to ΔB_0 inhomogeneities. The extra duration of unipolar shapes also increases minimum achievable TE and TR which can hinder setting up challenging high resolution fMRI protocols.

Experimental validation

Experimental Validation was performed with an agar gel phantom on a parallel transmission-enabled 7T Siemens (Siemens Healthcare, Erlangen, Germany) Magnetom VB17 system equipped with a 8Tx/32Rx Nova head coil (Nova Medical, Wilmington, MA)

The Slab-UP optimization was performed on a database of 20 3D B_1/B_0 field maps [Gra+17c]; this enabled the generation of a single universal pulse, applicable, although suboptimal, to any slab position and orientation with a satisfying level of flip-angle homogeneity. This simple approach therefore facilitated the automation of the RF pulse solution for arbitrary slab acquisitions, sparing the need to optimize a new pulse for each slab orientation, thickness and position, and offering at the same time an alternative to tailored pulse design. To demonstrate the feasibility of the approach, a Slab-UP was optimized consisting in three 0.92 ms long pulses of TBP = 10 and targeting a flip angle of 30°. Peak amplitude of (16.48V) and constraints (0.8697W total and 0.1631W per transmit channel) were enforced explicitly [Hoy+14] to respect the real hardware constrains of 165V (peak voltage) and 8w/1.5W (power) after conversion to sinc RF pulses. The k-space trajectory is optimized as well [Gra+15]. Bloch simulation of the pulse was perfomed for the non selective and slab selective (axial, 5cm thickness) pulses on one of the B_1/B_0 brain maps from the database to ensure that the performance the UP remains the same when converted into Slab-UP. Eventually, the pulse was inserted into an AFI ($TR_1 + TR_2 = 200ms$, $TR_2/TR_1 = 7$, i-PAT

= 2, resolution = $3 \times 3 \times 4mm^3$, matrix = $64 \times 64 \times 40$) sequence and the returned flip angle maps were compared to Bloch simulations.

Finally, to motivate the use of bipolar pulses, robustness against B_0 inhomogeneity for bipolar pulses was tested by comparing their simulated flip-angle maps with those from unipolar and RF shim pulses on the field-map database. The unipolar slab-UP was obtained from a dedicated optimization where the duration between each subpulse has been extended to insert the rephasing lobes of the unipolar slab-selective gradient. The RF shim pulse was made of a single sinc shape of 3 ms duration with TBP 10. The simulations were performed over axial slabs, incorporating large B_0 offset regions.

3.1.2 Results

Figure 3.1-2 shows the result of the pulse design on the left column with its slab-UP conversion on the right column. the new constraints allowed the sinc RF to be under hardware limits. The slab-UP duration is slightly longer because of the rephasing gradient lobe. An NMRSE of 9.1% over the database was achieved by the pulse and the similarity of the flip angle maps between the non-selective UP and the slab-UP indicating the conservation of performance after convertion. Outer slices have smaller flip angle indicating that the BTP of 10 could be increaded further to improve the sharpness of the slab profile.

Figure 3.1-3 reports Bloch simulation of the designed slab-UP for two slab positions versus the flip angle measured with the AFI sequence on a phantom. A good agreement between the simulation and the experiment is indicated by the same flip angle profiles for the AFI acquisition and the Bloch simulation. Therefore, faithful flip angles obtained via simulation on brain maps should be expected experimentally. Flip angle homogeneity was suboptimal here because the pulse was optimized on the database of field maps acquired on volunteers but tested on phantom.

Figure 3.1-4 is an example displaying a 0.8 mm resolution slab-UP acquired with an EPI sequence masked (tresholding) and overlaid on an MPRAGE image.

3.1-5 shows simulated flip-angle maps with the designed bipolar and unipolar slab-UP as well as RF shim pulse on 4 subjects of the 20-field map database. First, multi-spoke pulses performed better than RF shim (9.1% and 10.9% mean NRMSE across subjects versus 20.0%) for flip-angle homogeneity, as they provide more degrees of freedom for optimization. In addition, bipolar pulses yielded more homogeneous maps, as they suffered less from B_0 inhomogeneity. Despite relatively similar NRMSEs, the figure highlights important differences close to the large B_0 offset regions (here the ear canals).

3.1.3 Discussion

slab-UP were designed using the Universal Pulse k_T-point optimization algorithm with adapted constraints. Bloch simulations of the slab-UP on the brain maps yielded a better performance than RF shimming. Bloch simulations and experimental AFI flip angle maps were in good agreement, thereby strengthening confidence in the NMRSE performance of the pulse on the brain.

The slab-UP was optimized across the whole brain instead of optimizing a pulse for every slab configuration avoiding having a cumbersome pulse library. However, in order to be played by the sequence, the slab-UP pulse is inserted in the sequences through a text file containing

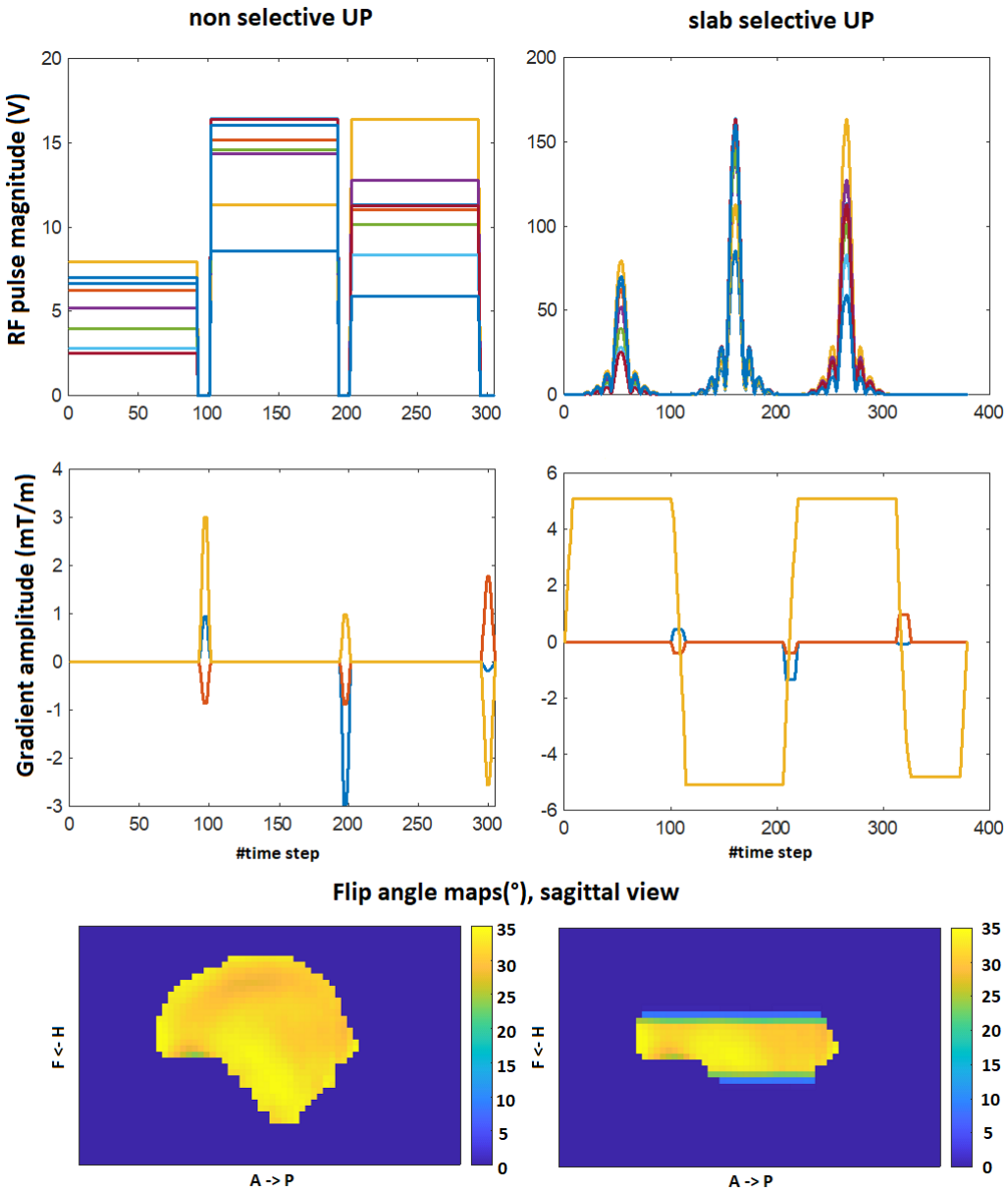

Figure 3.1-2: **Conversion from the non-selective UP to a slab-UP(axial), target FA = 30°.** Comparison between a non-selective UP (left) versus its slab selective pulse conversion (right). Each color represents a different transmit channel (top) and different gradient axis (middle). The blips in z axis (yellow) are played during the ramps of the slab-selective gradient. Notice the effect of the constraint peak voltage on the amplitude of the RF shapes. In this case, the maximum voltage was set up to 16.48V so the sinc RF shapes (BTP=10) respect the 'real' hardware constraint fixed at 165V. The bottom figures are simulated flip angle maps yielded by both excitations (whole brain NMRSE 9.1% over the database). The flip angle profile in the selected region by the slab-UP is the same as in the full brain flip angle map.

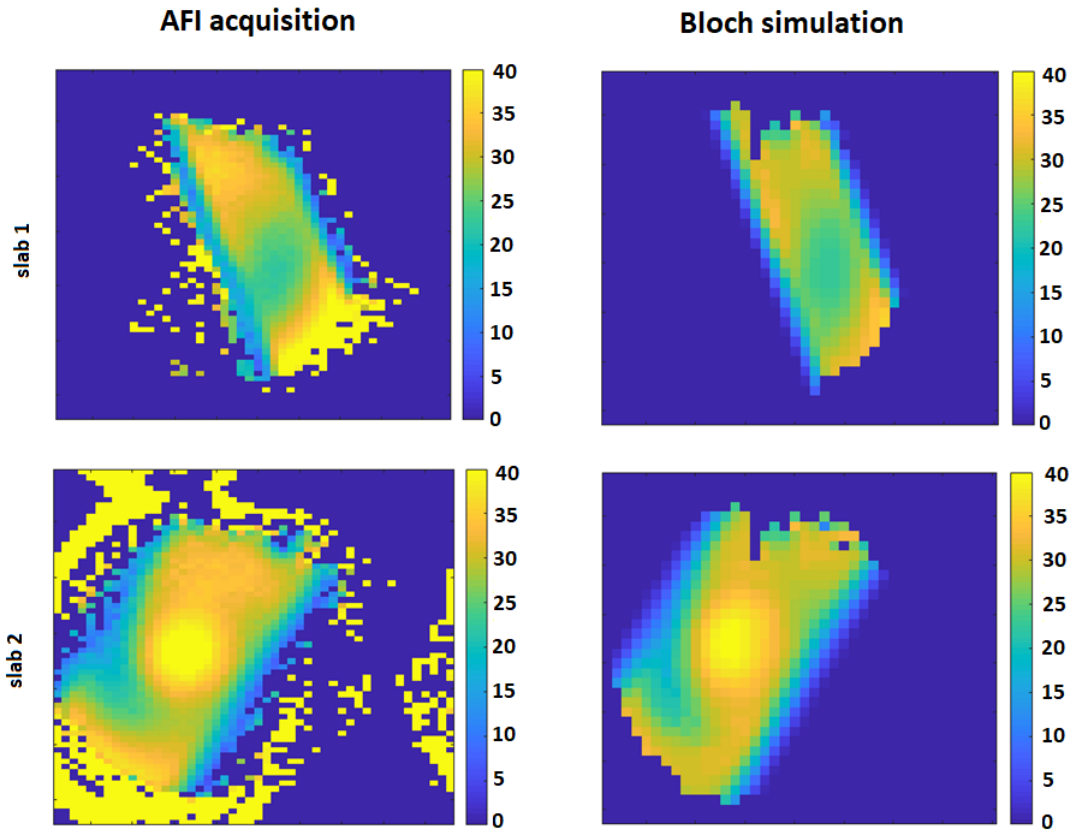

Figure 3.1-3: **Experimental Flip angle maps versus simulation with a slab-UP on phantom for two slab configurations. Sagittal view.** The similarity between the acquisition and simulation images show a good agreement between the theory and the experiment. Yellow pixels around the slab in the AFI acquisition are due to a wrong estimation of the flip angle because the signal is too weak.

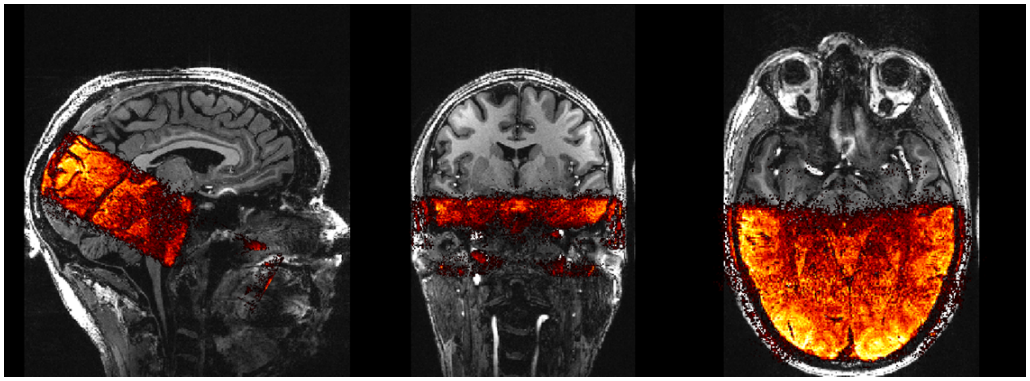

Figure 3.1-4: **0.8 mm, 4.5 cm thick tilted slab-UP.** The slab (hot colomap) is thresholded and overlaid on an anatomical MPRAGE scan.

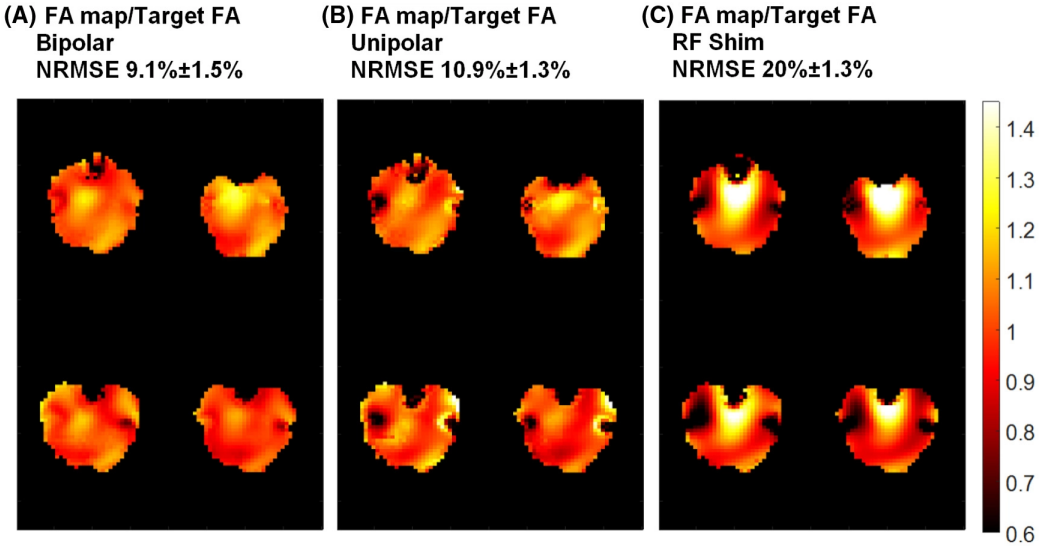

Figure 3.1-5: **Three simulated flip-angle (FA) maps from k_T-point solution for bipolar, unipolar, and RF shim configurations on the database, axial view.** Field maps over 4 subjects of the 20 found in the database are shown. The maps were normalized by the target flip angle. Bipolar pulses give more homogeneous maps than unipolar and RF shim pulses. Bipolar (A), unipolar (B), and RF shim (C) scenarios are shown. Abbreviation:NRMSE, normalized RMS error.

metadata and pulse shapes. Since slab configuration has an influence on the slab-selective gradient, an input text file is needed for each slab configuration putting the user into the pulse library pitfall again. Therefore, in order to have the original plug-and-play philosophy of Universal Pulses, a sequence integrated module was developed which generated/adapted the slab-UP to the desired FOV. This work is described in chapter 4.

Finally, although the robustness of bipolar compared to unipolar pulses has been demonstrated, bipolar pulses are sensitive to gradient delays with respect to RF that can raise from the fast slab selective gradient commutations or hardware imperfections. This leads to artifacts characterized by signal dropouts in the image. The following section describes a method to correct for them.

3.2 Gradient delay correction

The work in this section has been published in a peer reviewed journal:

R. Jamil, F. Mauconduit, V. Gras and N. Boulant. 'General gradient delay correction method in bipolar multispoke RF pulses using trim blips'. In: *Magnetic resonance in medicine* 85.2 (2021), pp. 1004–1012

The purpose of this section proposes a general method correcting for gradient delays using bipolar RF pulses using trim blips. Trim blips a referred as gradient lobes of small integral. The method described here allows a correction for any slab position and orientation as well as for different gradient delay scenarios.

3.2.1 Introduction

In MRI experiments, eddy currents occur in conductors surrounding the sample during fast gradient commutations, generating secondary fields and affecting the impulse response function of each gradient axis [AB98]. Despite pre-emphasis, this can result in a remaining gradient delay induced by low-pass filtering effects, while delays can also be caused by time mismatches in the experimental chain. In this context, anisotropic delays have also been reported in the literature,[AB98; RHU18] whereby they could distort k-space trajectories severely during acquisition readout, leading to ghosting and blurring [AB98]. Likewise during RF transmission, the effects of gradient delays have been studied for multi-dimensional pulses to show the distortion of the excited patterns [AB98; Oel+04; RFF02; RFF02]. In RF field inhomogeneity mitigation at ultrahigh field (UHF), multispoke [Sae+06] bipolar selective RF excitation performance also can suffer dramatically from gradient delays [Jan+10; TWP17; Gra+17a].

Unipolar spoke pulses are immune to these imperfections but are less time-efficient, and therefore less robust versus B_0 offsets because of their extra rephasing/prephasing gradient lobes increasing the time between subpulses. The poorer time efficiency also can impact minimum TEs and TRs in MRI acquisitions, such as affecting functional contrast-to-noise ratio in functional MRI. Based on prior knowledge about the delays, conceptually the most straightforward approach is to temporally shift the RF pulse waveform [TWP17]. This method, however, is not strictly applicable to tilted slices or slabs in case of anisotropic gradient delays. Instead, shifting the different axis gradient waveforms individually would address the problem but would require for high accuracy a dwell time smaller than typically available on most systems. The gradient delay can also be corrected by adding a phase to every other spoke for slice excitations [Gra+17a]. Nevertheless, because this phase correction depends on the distance from the slice to the isocenter, it remains suboptimal for slab excitations because a unique phase correction cannot address the problem across all locations in the slab.

However, as shown in Gras et al,[Gra+17c] the fact that the delays effectively induce a dephasing that is proportional to that distance implies that it can be canceled with so-called gradient "trim-blips" [Oel+04], initially reported to correct for N/2 ghosts in tilted echo-planar 2D-selective RF excitation pulses, including in the presence of anisotropy. In this work, we report experimental and successful demonstrations of this technique with parallel transmission bipolar spokes in vivo at 7 T. The method is shown to be general in the sense that it is applicable to any gradient delay and slab-orientation configurations.

3.2.2 Theory

Throughout this note, gradient delays—regardless of their origin—refer to the time mismatch between the gradient and RF pulse waveforms and are denoted as Δt_j along axis j. As shown in Gras et al,[Gra+17a] we can characterize and illustrate the effect of a gradient delay on bipolar-spoke pulses using a simple double RF subpulse experiment. Details can be found in Gras et al,[Gra+17a] but for clarity, the key aspects are reminded here. Axial slices are considered here for the first equation, but calculations apply to the other orthogonal orientations as well. For demonstration purposes, RF pulses are padded with zeros. This padding is applied only during gradient plateaus for a duration Tp. Even if in practice there

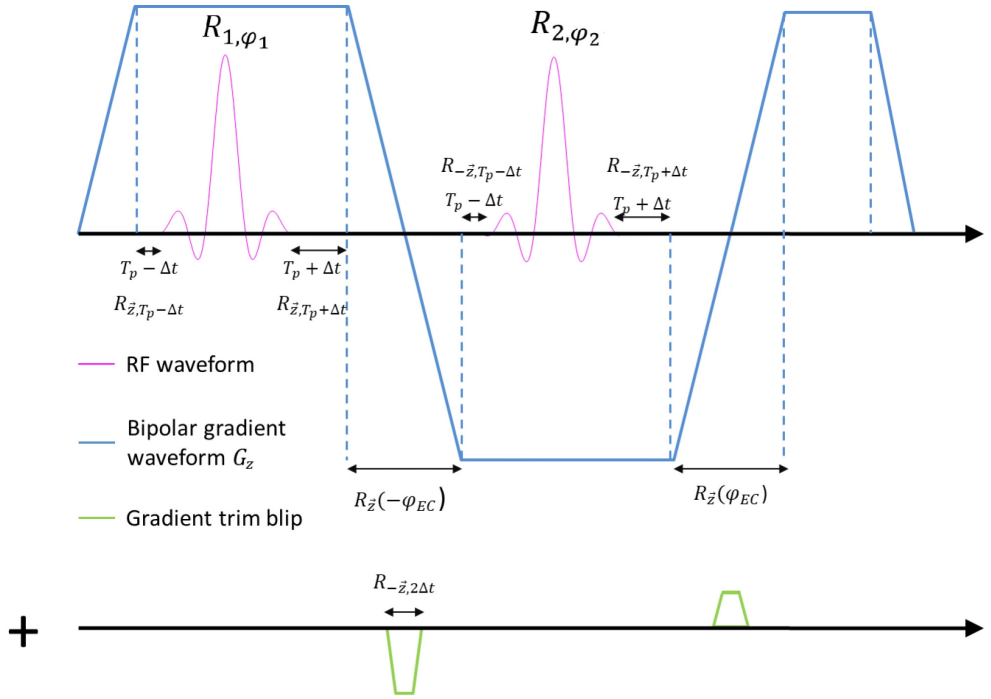

Figure 3.2-6: **Double RF subpulse experiment used to characterize gradient delays.** Gradient-induced rotations are displayed. Because of eddy currents and gradient delays, unwanted rotations arise. They can be corrected by a trim blip (green) between the two RF pulses. The second blip ensures intravoxel phase refocusing.

is no such padding, apodization of the RF pulses makes it a good simplifying approximation. Eddy currents occur during gradient slopes, but the first and last slope eddy currents are ignored because they do not affect the flip angle.

Figure 3.2-6 shows the spin rotations corresponding to the series of events. Without gradient delay ($\Delta t = 0$), gradient plateaus during padded periods generate a rotation around the $\overrightarrow{z}$ axis of angle $\pm\gamma G_z z T_p$, noted $R_{\overrightarrow{z}}(\pm\gamma G_z z T_p)$ with γ being the gyromagnetic ratio of water, G_z being the slice-selection gradient amplitude, and z being the spin location. The eddy currents generated by the second and third gradient slopes are modeled here as spatially constant, zero-order rotations along $\overrightarrow{z}$ of angle $\pm\varphi_{EC}$. The RF pulses lead to rotations noted as R_{1,φ_1} and R_{2,φ_2}, assumed to be purely transverse, with φ_1 and φ_2 being their respective phases. Their axis of rotation is determined by the gradient period during which the RF is on. By using the relation $R_z(\theta)R^{\perp}_{\varphi}R_z(-\theta) = R^{\perp}_{\theta+\varphi}$, where $R^{\perp}_{\varphi}$ is a purely transverse rotation around an axis $\cos(\varphi)\overrightarrow{x} + \sin(\varphi)\overrightarrow{y}$ and assuming no gradient delay, the total rotation R_{tot} is

$$R_{tot} = R_{\overrightarrow{z}}(\varphi_{EC})R_{\overrightarrow{z}}(-\gamma G_z z T_p)R_{2,\varphi_2}R_{\overrightarrow{z}}(-\gamma G_z z T_p) \tag{3.6}$$

$$R_{\overrightarrow{z}}(-\varphi_{EC})R_{\overrightarrow{z}}(\gamma G_z z T_p)R_{1,\varphi_1}R_{\overrightarrow{z}}(\gamma G_z z T_p), \tag{3.7}$$

$$= R_{\overrightarrow{z}}(-\gamma G_z z T_p)R_{2,\varphi_2+\varphi_{EC}}R_{1,\varphi_1}R_{\overrightarrow{z}}(\gamma G_z z T_p). \tag{3.8}$$

With an additional gradient delay Δt_z, durations T_p are shifted by plus or minus Δt_z, as depicted in Figure 1. The equation in this case becomes

$$R_{tot} = R_{\overrightarrow{z}}(-\gamma G_z z(T_p + \Delta t_z))R_{2,\varphi_2+\varphi_{EC}}R_{\overrightarrow{z}}(2\gamma G_z z \Delta t_z)R_{1,\varphi_1}R_{\overrightarrow{z}}(\gamma G_z z(T_p - \Delta t_z)). \tag{3.9}$$

which can be recast as

$$R_{tot} = R_{\vec{z}}(-\gamma G_z z(T_p - \Delta t_z))R_{2,\varphi_2+\varphi_{EC}-2\gamma G_z z\Delta t_z}R_{1,\varphi_1}R_{\vec{z}}(\gamma G_z z(T_p - \Delta t_z)). \quad (3.10)$$

For flip-angle computation purposes, because the first and last terms do not affect the flip angle, we see here that eddy currents and gradient delays can be pictured as effectively generating a phase shift of the second subpulse, valid in the small and large flip-angle regimes. The phase shift induced is proportional to gradient amplitude and spin position, and therefore is amplified for locations far from isocenter and for pulses with large time-bandwidth products (TBPs) and/or thin slices. For example, with $G_z = 30mT.m^{-1}$, a position $z = 3cm$ and a delay of $3\mu s$, the second subpulse is shifted about $83°$, which can be disastrous for bipolar spoke performance. This equation shows that the phase compensation method reported in Gras et al. [Gra+17a] works for slice selection when the position of the spins is relatively well defined (ie, with fixed position as in slice excitations), while it is not the case for slab-selection because of the broader range of spin positions. Time-shifting the RF waveforms [TWP17] can also work but requires better than $1 - \mu s$ discretization for high accuracy and is inapplicable for tilted slices with anisotropic delays. In the case of tilted slab acquisitions with anisotropic delays, the previous formula for inclination, such as towards the left-right axis, can be written as

$$R_{tot} = R_{\vec{z}}(-\gamma G_z z(T_p + \Delta t_z))R_{\vec{z}}(-\gamma G_y y(T_p + \Delta t_y))R_{2,\varphi_2+\varphi_{EC}}R_{\vec{z}}(2(\gamma G_z z\Delta t_z + \gamma G_y y\Delta t_y)) \quad (3.11)$$

$$R_{1,\varphi_1}R_{\vec{z}}(\gamma G_z z(T_p - \Delta t_z))R_{\vec{z}}(\gamma G_y y(T_p - \Delta t_y)). \quad (3.12)$$

where φ_{EC} this time denotes the combined zero-order eddy current of the y and z gradients. It is therefore clear now that inserting the appropriate gradient trim blips between the two spoke RF pulses can cancel the effect of the anisotropic gradient delays, regardless of the position. The zero-order eddy current phase can still be corrected with a phase shift on the second pulse. For more than two bipolar spokes, the same principle can be applied by introducing trim blips before each subpulse of even rank number. If initial gradient ramps evolve at maximum slew rate, they may have to be lengthened by a few tens of microseconds, to insert the trim blips without violating gradient constraints. Alternatively, the gradient ramps can be a bit longer from the start, so that the insertion does not modify the timing, which was the approach selected in this work. By the same token, this same formalism can be used to show that unipolar pulses, because they have the same gradient polarity, are immune to gradient delays,[Gra+17a] in the limit of the assumptions made in this model. They are, on the contrary, less robust to B_0 offsets and have an effect on minimum achievable TEs and TRs because of their poorer time efficiency, which worsens with the number of subpulses (spokes).

3.2.3 Methods

RF pulse design

Slab selective Universal Pulses (Slab-UP) were generated following the method described in 3.1, the key steps are reminded here. Pulses were generated using the Universal pulse parametrization [Clo+12], returning RF and gradient coefficients for 3D non-selective excitations

but applicable to spoke slab selection regarding the power constraints. These coefficients were then applied to sinc shapes with superposed gradient-selection waveforms to get slab-selective RF pulses. For the in vivo experiments, two pulses were generated: the first one (pulse 1, ie, the one used for the simulations comparing the bipolar approach with the unipolar and RF shim ones in 3.1) was used for higher SNR flip-angle measurement, and the second pulse (pulse 2) was used for temporal SNR (tSNR) measurement and was made of two subpulses of 0.52-ms length each, 10° flip angle, and a TBP of 25.

Bloch simulations

Several Bloch simulations were performed on measured in vivo B_1/B_0 maps to show the superiority of the trim-blip correction. Flip-angle performance of phase correction, RF waveform time-shifting, and trim blips on a tilted slab with different delay configurations were simulated with pulse 2, with the field map measured on one volunteer. Delay on y was fixed at 4 μs (the measured value), and delay on $\vec{z}$ was increased by steps of 2 μs from 2 μs to 6 μs. The flip angle on the same slab (30° tilted, 4-cm thickness, 5-cm shift) was simulated each time. The flip-angle maps were divided by a flip-angle reference map simulated without delays. Because other methods are not strictly compatible with oblique slabs in the presence of anisotropic delays, an optimal value of the delay for the phase correction and RF waveform time-shifting methods was determined by the sum of the delays on $\vec{y}$ and $\vec{z}$ weighted by the square of the cosine and sine of the inclination.

Experimental validation

Experiments were carried out on a parallel transmission-enabled 7T Siemens (Siemens Healthcare, Erlangen,Germany) Magnetom system equipped with an SC72 gradient (42 mT/m maximum amplitude, 200 mT/m/ms slewrate). A Nova head coil (Nova Medical, Wilmington, MA) was used for parallel transmission (8 channels) and reception (32 channels). Gradient delays were measured on each axis on an agar gel phantom with a gradient-echo 2D sequence following the method proposed in Gras et al. [Gra+17a]. It consists of implementing the two-pulse experiment shown in Figure 3.2-6 with 180° phase shift between the two pulses plus another incremental phase offset on the second pulse. When there is no delay, the signal returned is minimal when the phase offset is zero. But according to Equation 3.10, a nonzero phase offset that minimizes the signal is equal to $-\varphi_{EC} + 2\gamma G_z z \Delta t_z$. The delay can therefore be recovered by linear regression by varying z.

The in vivo experiments were approved by a local ethics committee, and written informed consent was obtained from all volunteers. The delay correction method was validated experimentally on 2 healthy volunteers by using the actual flip-angle imaging method[Yar07] (AFI) ($TR_1 + TR_2 = 200ms$, $TR_2/TR_1 = 7$, i-PAT = 2, resolution = $3 \times 3 \times 4mm^3$, matrix = $64 \times 64 \times 40$) as well as by measuring the tSNR with the 3D-EPI sequence (TR_{vol} = 1950 ms, i-PAT = 4×2, isotropic resolution = 1.2 mm, matrix =$160 \times 160 \times 52$ matrix) [Pos+10]. Tilted axial slabs about ±20° on left-right axis, 4-cm-thick and shifted by 4.5 cm from isocenter were acquired for each volunteer, with uncorrected then corrected bipolar and unipolar pulses, for the flip-angle measurements. Because unipolar pulses are immune to gradient delays, they were used as an experimental reference. For the tSNR measurements, a 4-cm-thick axial slab shifted 3 cm downward was acquired on volunteer 1 to compare unipolar

pulses with corrected bipolar pulses over regions of large B_0 offsets, whereas for volunteer 2 the same tilted acquisition as for the AFI sequence was performed. Measured flip-angle maps were compared to Bloch simulations obtained with measured B_1 and B_0 maps for retrospective control. Because in our setup the delays measured were in fact similar on $\vec{y}$ and $\vec{z}$, the AFI acquisition on volunteer 1 was performed with an enforced anisotropy for the demonstration. For that purpose, the gradient waveform along the z-axis was shifted by the smallest time step possible ($10\mu s$) for pulse 1. Still for the AFI measurement, pulse 2 was used on volunteer 2 with the measured, isotropic, gradient delays to attempt verifying the flip angle implemented for the tSNR measurements.

The tSNR maps were calculated by taking the ratio of the temporal mean over standard deviations over 50 volumes for the 2 volunteers. Images were aligned using the McFlirt [Jen+02] routine of the Oxford FMRIB Software Library before tSNR computation. A histogram of the ratio of the tSNR map pooled on both volunteers from the delay-corrected acquisition on the noncorrected one was also calculated. A mask was used to exclude nonbrain voxels.

3.2.4 Results

Optimization of the k_T-point solution returned 9.1% normalized RMS error (NRMSE) for pulse 1 and 13.2% for pulse 2, on average, over the brain and over the 20 subjects of the pulse design database, making the solution applicable for every slab configuration (although suboptimal). The homogeneity performance of pulse 2 here for a small tip angle pulse was worse than in other work [Clo+12]. This is due to the smaller number of subpulses (two versus typically five), a high TBP, and a short pulse duration (1.2 ms total), engendering saturation of the peak power constraints. The 13% performance remains in any case comparable to the field inhomogeneity measured at 3T in the brain in circularly polarized mode[BLA08] and better than the RF field homogeneity that can be obtained at 7 T in the same mode (20%) [BMA09]. Delays on the $\overrightarrow{x}$, $\overrightarrow{y}$, $and \overrightarrow{z}$ axes of 3.5 μs, 4 μs, and 4 μs were measured with zero-order eddy-current phase offsets of 7°, 8° and 18°, respectively. The time gain for the pulse from unipolar to bipolar was 2.1 ms for pulse 1 and 1.2 ms for pulse 2.

Figure 3.2-7 shows by means of simulation the performance of phase correction, RF waveform time-shifting, and trim blips on a tilted slab with different delay configurations. On the top left, the flip-angle map without any delay represents the reference, while the other maps are the flip-angle ratio with delay (corrected or not) and the latter reference. According to Equation 3.11, the delays generated phase shifts ranging from 104° to 242° over the 4-cm thickness, and therefore cannot be accurately compensated with a constant phase shift [Gra+17a]. This is why phase correction strictly works for one slice position only. As expected, RF waveform time-shifting works perfectly in the case of isotropic delays (4-µs delay on each axis), but its performance drops when anisotropy is present. Only trim blips allows perfect correction for all delay configurations, yielding a ratio map uniformly equal to 1. Importantly, one can observe significant deviations from the reference, even in the case of more realistic anisotropies than enforced experimentally in this study.

Figure 3.2-8 shows the flip-angle maps acquired on the 2 volunteers with the AFI sequence. Effective delays on y and z for the measurement on volunteer 1, respectively, were 4 μs and 14 μs, as anisotropy was added, whereas they were both 4 μs (the measured values) for

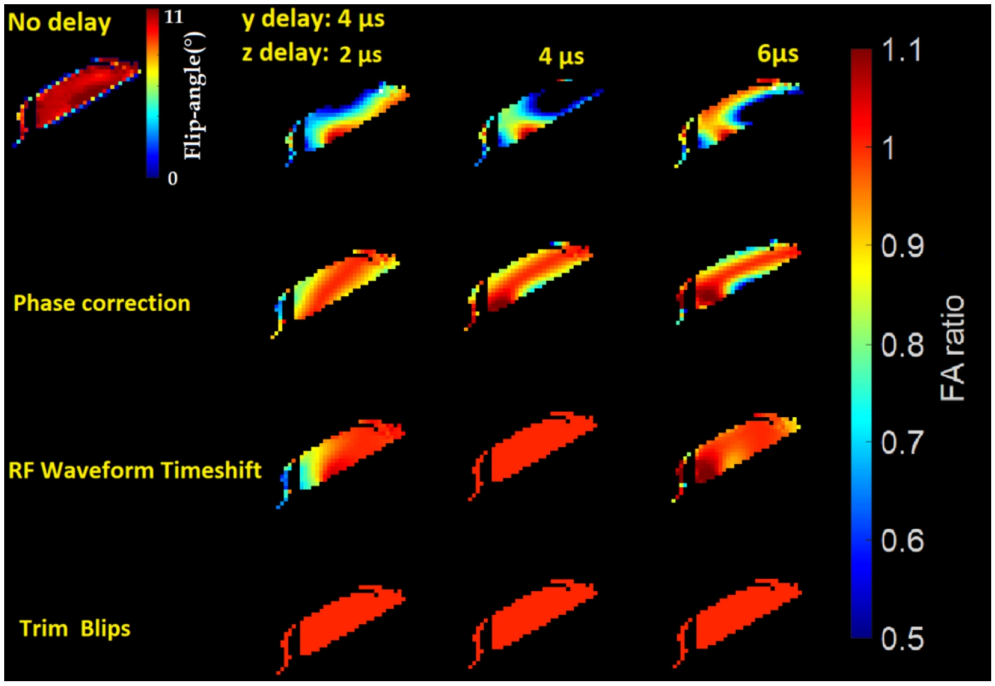

Figure 3.2-7: **Flip-angle ratio maps of phase correction, RF waveform time shift, and trim blip corrections for different delay configurations.** From left to right: simulations with delays of 4 μs on y and 2, 4, and 6 μs on z. From top to bottom: simulations without correction, with phase correction, RF waveform time-shifting, and trim blips. Each slab is compared with the no-delay reference-simulated flip-angle map on the top left with a ratio. Phase correction performs poorly for off-centered regions. The RF waveform time-shifting performs perfectly for isotropic delays, but only trim blips shows perfect correction for every configuration.

the second volunteer. Trim blips appear to efficiently correct gradient delays by recovering the expected flip-angle maps as the ones obtained with unipolar pulses. The latter was used as a reference, as it is supposed to be immune to gradient delay effects. In general, Bloch-simulated flip-angle maps are in good agreement with the experimental data in the case of oblique slabs and even in anisotropic configurations (Figure 3.2-8A). For the second volunteer (Figure 3.2-8B), in some regions, measured flip angles in the uncorrected bipolar scenario were incorrect (inversion of the signal flip-angle relation of the AFI technique led to imaginary values) due to the lack of SNR induced by a too-small flip angle and were therefore masked. Residual differences can still be observed between the simulations and the measurements, which can be attributed to finite accuracy of B_0/B_1 maps and possible motion between the field map acquisitions and flip-angle measurements.

Figure 3.2-9 reports the calculated tSNR maps from the 3D-EPI acquisitions overlaid on MPRAGE images. As expected, in agreement with the flip-angle measurements and simulations, a remarkable amount of signal was recovered in the cerebellum (volunteer 1) and in the parietal lobe (volunteer 2) (see white arrows). For the first volunteer, the figure also confirms experimentally the superior robustness versus B_0 offsets of the bipolar approach (pink arrows). The histogram in Figure 3.2-9C shows that for most voxels, the ratio between the tSNR map acquired with trim blips with the one acquired without is above 1, meaning that the correction allows an overall increase in tSNR, which is here about 28%. Voxels in which the gain is inferior to 1 can arise because of interscan and intrascan motion as well as

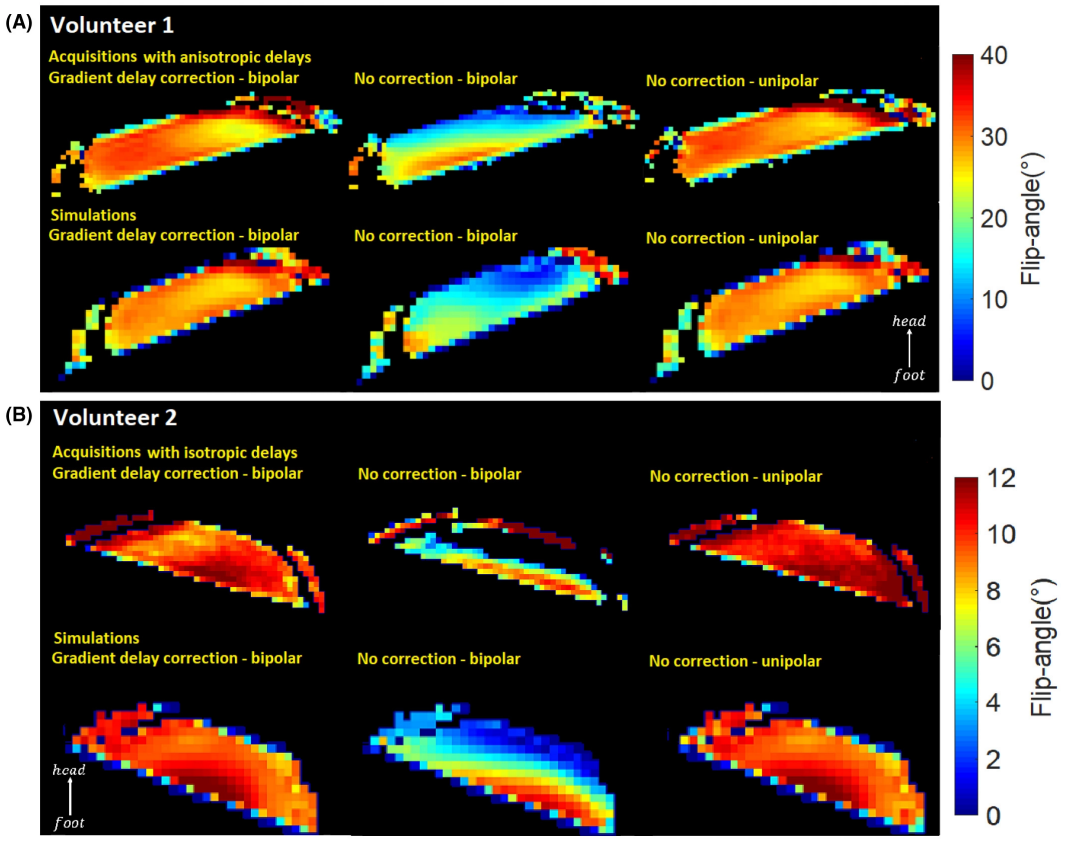

Figure 3.2-8: **Measured flip-angle maps versus Bloch simulations. For each volunteer, the top row displays AFI slab acquisitions, on the bottom row, Bloch simulations.** A, For volunteer 1, a $+20°$ tilted slab was acquired with pulse 1 and enforced gradient anisotropy. B, For volunteer 2, a $-20°$ tilted-slab pulse was acquired with pulse 2, with the measured, isotropic, gradient delays. We see good agreement between simulations and acquisitions, so that corrected pulses with trim blips alleviate effectively gradient delay effects.

imperfect masking procedure, keeping voxels out of the brain.

3.2.5 Discussion and Conclusion

We have described in this work a general method to correct for gradient delays occurring during multispoke bipolar excitations. These gradient delays are caused primarily by eddy currents through a low-pass filtering effect or possibly a time mismatch from hardware imperfections.

As shown in the simulations (Figure 3.2-7), previous methods from the literature are suboptimal either for slab excitations (phase adaptation method) or for anisotropic delays (time-shifting method) in tilted acquisitions, whereas the gradient trim blip method is applicable to any configuration. The correction consists of placing after every odd rank subpulse a gradient blip along each axis used for slab or slice selection, thereby canceling unwanted phase shifts.

From the sequence programming standpoint, such trim-blips can be hard-coded and implemented according to the measured delays and the amount of gradient strength along each axis, but regardless of the slab position. Chapter 4 describes the sequence implementation of gradient delay measure and correction tool in the sequence. Furthermore, from a practical

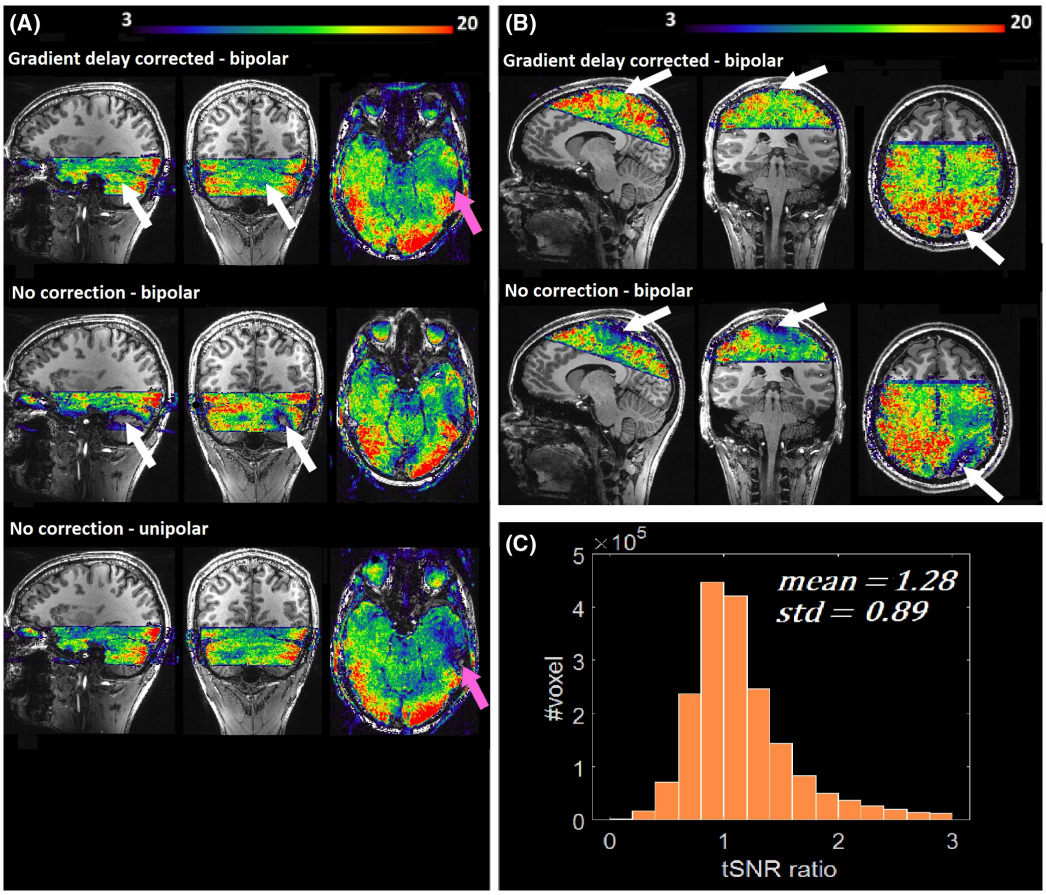

Figure 3.2-9: **Temporal SNR (tSNR) maps from 3D-EPI acquisitions superposed on anatomical images and histogram of the ratio of the tSNR maps.** The double RF spoke pulse from the same design was used on the 2 volunteers with delay-corrected bipolar pulses (top row) and bipolar uncorrected pulses (bottom row). The pulses used are double-spoke RF pulses with axial (A) and $-20°$ (B) tilted orientations derived from the universal kT-point solution. White arrows show regions where severe delay artifacts were corrected with trim blips. Pink arrows in (A) point toward large B_0 offsets (ear canals), where corrected bipolar pulses outperform the unipolar ones. C, Histogram of the tSNR ratio (bipolar corrected over bipolar uncorrected) pooled over the 2 subjects.

perspective, it is also interesting to observe again that one kT-point coefficients solution over the whole brain appeared sufficient to yield satisfying performance over the selected slabs, especially for small interpulse TR, in which the signal variation versus flip angle deviation is null to first order at the Ernst angle, thus facilitating future automation of the universal pulse approach for slab excitations. This automation would consist in taking the returned kT-point coefficients and simply apply them to the spoke subpulses with appropriate sinc-like shapes, while the gradient waveforms are adjusted automatically by the sequence to select the desired slab for each volunteer. This framework will be described in chapter 4.

In vivo experiments showed very good results in removing gradient-delay effects without extra scan time, provided that prior knowledge of the gradient delays is available and that the values are stable over time. The latter stability was confirmed in other work [Gra+17a], but can be controlled at regular maintenance checks. In this study, the correction method also assumed that the delay on each axis was independent of events on other axes. However, agreement between the simulations and the measurements in the case of different

orientations, and therefore with different gradient polarities on one axis supports this as a correct assumption. The NRMSE score of bipolar and unipolar pulses was close over the whole brain, calling again into question the necessity of bipolar pulses, but we have highlighted in previous simulation (Figure 3.1-5) and now experimentally (Figure 3.2-9A) that the NRMSE is a global metric and that noticeable differences can still be observed in large B_0-offset regions.

Finally, although the gain in volume TR of the bipolar versus the unipolar parametrization in our functional MRI demonstration can be considered marginal ($52 \times 1\text{-}2$ ms = 52-104 ms), the shorter duration of the former approach can have much larger impact in other slab-selective anatomical[Lou+15] and functional MRI [SE16] sequences. It is worth stressing that the correction made here was in addition to the manufacturer's correction. Measured delays were up to 4 μs, but as demonstrated, they can have a drastic effect on flip-angle excitation and SNR. The level of the effect increases with gradient strength and position with respect to isocenter. Acquisition parameters for the 3D-EPI sequence were relevant for functional MRI routine (TR $<$ 2 seconds, isotropic resolution of 1.2 mm). The results show that gradient delays cannot be ignored in the bipolar-spoke situation.

* * *
* *
*

Chapter 4

Sequence implementation

Chapter Outline

4.1 Implementation of the pulses in the sequence . . . 61
4.1.1 Methods . . . 61
4.1.2 Preliminary results . . . 64
4.1.3 Discussion . . . 66
4.2 Gradient delay diagnostic tool . . . 66
4.2.1 Principle and methods . . . 66
4.2.2 Results . . . 67
4.2.3 Discussion and perspectives . . . 68

This chapter describes the implementation of the slab-UP into the 3D-EPI sequence and the implementation of a simple diagnosis and correction tool for gradient delay artifacts. The manufacturer's framework and its limitations will be briefly described to motivate the current implementation choices of the slab-UP. The implementation described here has the benefit to be easily applicable to other sequences. Finally, for both sections, preliminary results are shared and discussed.

4.1 Implementation of the pulses in the sequence

4.1.1 Methods

Background

The Universal Pulse framework brings the benefits of parallel transmission without its difficulties. Indeed, parallel transmission allows designing pulses mitigating RF field inhomogeneity while keeping SAR under safety limits. However, parallel transmission has failed to be fully adopted in routine by the community because of its additional hardware and mostly because of its cumbersome workflow. First subject-tailored approaches needed the information of transmit field maps and therefore relied on time-consuming B_1^+ mapping acquisition, despite recent progress. Then, an optimization algorithm on the fly was executed to yield pulses that are eventually played on the scanner. Universal Pulses propose a plug-and-play approach where the pulse design is performed once and for all on a database of previously

acquired B_1^+ maps assuming limited variations in transmit field maps between individuals. Consequently, no additional calibration is needed for the user.

Following Universal Pulses developments, Gras et al. [Gra+19; Mas+22] introduced a package of anatomical sequences employing Universal Pulses (Pasteur package) including 3D-GRE, MPRAGE, FLAIR, DIR and SPACE sequences. Pulses are optimized for an upper bound flip angle but can be scaled down to avoid having a pulse for each target flip angle. The pulses are directly embedded into the sequences as a text .ini arbitrary file that is read by the sequence on the scanner. In the manufacturer's parallel transmit framework the arbitrary files are traditionally organized into three sections:

- `pTxPulse`: This section contains metadata regarding the pulse. Different fields specify the number of transmit channels, the maximum voltage reached by the RF pulses or the flip angle among others.
- `Gradient`: This section contains gradient temporal waveforms to be played, in the case of kT point or spoke Universal Pulses, gradient blips.
- `pTXPulse_chN`: Similarly to the Gradient section, it contains the RF magnitude and phase time-courses for channel N. There is such a section for each transmit channel.

The system will read all gradient and RF shapes and put them into RF pulse objects that are executed by the scanner. Depending on the slice or slab orientation, the system can project the provided gradient shapes into other axes with a rotation matrix. However, gradient blips must remain invariant with regard to slice orientation in order to provide the right k-space trajectory for RF transmission. Therefore, a rotation compensation matrix has been implemented to counteract the systems' intervention on the gradient shapes.

Adding the slab-selective feature

The parallel transmission implementation of the 3D-EPI sequence was done on the SIEMENS IDEA environment version VE12 in the object-oriented C++ programming language, building upon the single channel version coded by Rudiger Stirnberg (DZNE, Bonn, Germany). Adding the slab-selective Universal Pulses involved the addition of several features while several technical choices were made to counteract the system's current limitations.

First, in order to avoid having a different arbitrary file for each slab thickness and orientation, a function generating the slab-selective gradient was implemented. The slab-selective gradient is defined and declared in an independent object. Therefore, a rotation gradient can be freely employed on the slab-selective gradient without modifying the gradient blips. It uses information from the system for the slab thickness and orientation as well as information from new fields added in the arbitrary ini file specifying the ramp time, the flat top time for the gradient lobes and the number of lobes. These durations remain constant.

Second, since gradient blips and slab selective gradient are played separately, a slew rate watchdog has been implemented to avoid sequence crashes. The function computes and checks the gradient time derivatives for the FOV orientation and thickness set up by the user.

The phase management is performed by a numerically-controlled oscillator (NCO). This digital 'clock' can accumulate phase and is employed by the frequency synthesizer to control

RF frequency and phase. It is also used for phase modulation to change slab position with a phase defined by

$$\phi(t) = \gamma z \int_0^t G_{ss}(\tau)d\tau + \phi_0 \tag{4.1}$$

with γ the gyromagnetic ratio of water, z the center position of the slab and G_{ss} the slab-selective gradient amplitude and ϕ_0 a phase offset. In the case of slab-selective multi spoke RF pulses the phase of the NCO must cross the origin at the middle period of each sub-pulse. Consequently, the NCO phase accumulation must be ignored when no RF is played, in this case, during gradient blips. Otherwise, equation 4.1 shows that, in the case of the slab-UP, the blip will introduce a phase bias thereby spoiling the performance of the composite pulse shape.

Unfortunately, the system does not allow introducing NCO instructions while an RF object is executed. This limitation resulted into important design choices. First, one arbitrary pulse is considered by the system for each single RF sub-pulse throughout the composite pulse shape, with short time interleaved periods during which the RF is at zero volt (to play the gradient blips). Each RF subpulse was then executed as a separated RF pulse object, so that NCO instructions could be executed between each RF subpulse. Furthermore, the system can execute multiple RF objects sequentially but need an idle period between each of them. This supposes that the gradient blips needed to be executed independently from the RF pulse objects. As a workaround, gradient blip information was integrated into the arbitrary files as a matrix k containing k-space positions. This matrix would then be used to compute gradient blips directly in the sequence. This implementation also offers the benefit of facilitating the application of the trim blip correction for the gradient delays by simply correcting for the k-space positions instead of changing the whole gradient shapes.

Experimental validation

This implementation was integrated into the 3D-EPI sequence from DZNE Bonn (referred as 3D-EPI-UP) and the AFI sequences and tested on a parallel-transmission enabled 7T Siemens (Siemens Healthcare, Erlangen, Germany) Magnetom Terra VE12 system equipped with a 8Tx/32Tx Nova head coil(Nova Medical, Wilmington, MA). A Slab-UP of three sub pulses of 0.92 ms duration each, BTP 25 and target flip angle 15° was designed. A phantom tailored kt-point pulse with the same parameters as the slab-UP was generated as well.

Experiments consisted first in flip angle map comparison between Bloch simulation and the modified AFI to ensure that the arbitrary pulses were played correctly. Two slabs were acquired in vivo on two healthy volunteers with the 3D-EPI-UP at 1.6 mm isotropic resolution (TR/TE 55/22ms, FOV 208mm, acceleration factor 2x4, skipped-CAIPI (stirnberg et al. 2020) Δk_z=2, BW = 1832 Hz/Px). The first slabs were shifted to acquire specific regions. The first slab was aligned with the occipital lobe and the central sulcus, the second slab was aligned with the cerebellum and the frontal lobe. For demonstration, a flip angle of 5° was chosen to be in the linear regime (lower than the Ernst angle) to accentuate the effects of flip angle inhomogeneities and translate directly into tSNR differences in the EPI sequence. tSNR maps were computed from 50 3D-EPI volumes acquired with the slab-UP and in combine (CP) mode.

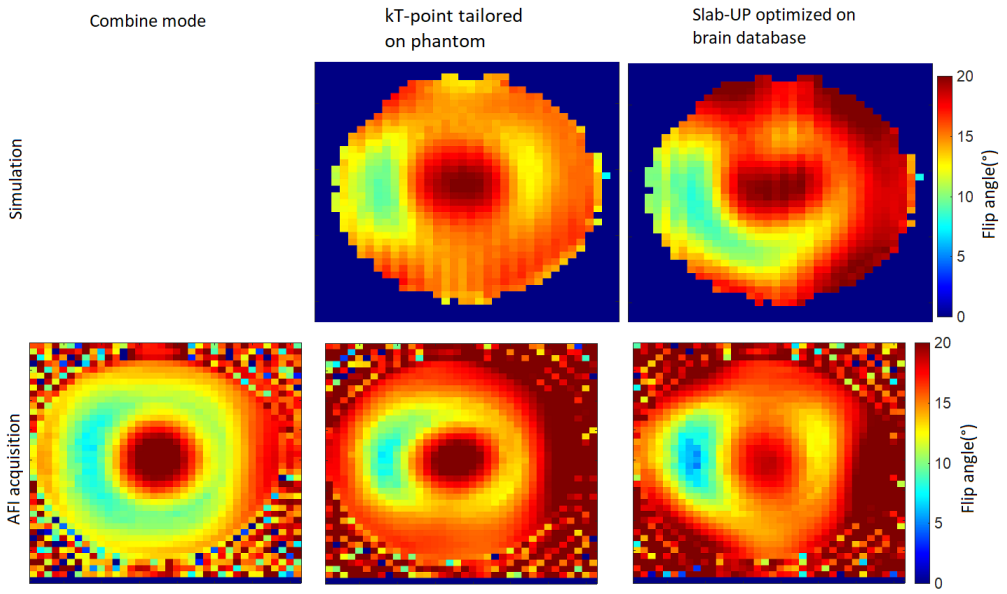

Figure 4.1-1: **Bloch simulations versus AFI flip angle maps (Target Flip angle = 15°, sagittal view).** Flip angle maps between Bloch simulations and acquisition with the modified AFI are in an acceptable agreement meaning that the implementation runs the pulses correctly.

4.1.2 Preliminary results

Figure 4.1-1 shows the flip angle maps yielded by the modified AFI in combine mode, with a k_T-point optimized for the phantom and a slab-UP compared to Bloch simulations with the same pulses. Unsurprisingly, the slab-UP outperforms the combine mode in flip angle homogeneity. The combine mode excitation yields a typical pattern where a vast region has a flip angle under the target resulting in a weaker signal. Similarity between Bloch simulations and AFI acquisition is not perfect because the sequence lacks precision when employed for flip angle excitation lower than 30° (for example, we can see a degradation of precision of the AFI in 3.2-8 between 30° and 10°). On the other hand, flip angle overshoot on right side of the AFI acquisitions comes from increased δB_0. Another explanation is the limited accuracy of the B_0/B_1 maps. The level of flip angle inhomogeneity in this phantom experiment can be acknowledged to be relatively high, even for the kT-point tailored implementation. This, however, is the result of increased field inhomogeneity on a spherical water phantom with large relative permittivity (≈ 72) compared to the human brain and the low number of k_T points used. This phantom experiment thus above all aimed at verifying the good implementation of the RF solutions in the sequences with agreement between experimental results and simulations.

Figure 4.1-2 displays tSNR maps for the two slab acquisitions in combine mode and with the slab-UP. Multiple brain areas have a better tSNR with the slab-UP compared to the combine mode. It is particularly noticeable in the cerebellum that is recovered thanks to the RF field inhomogeneity mitigation yielded by the slab-UP. These differences are emphasized by the small flip angle used, putting the signal in a linear regime under the Ernst angle. The typical flip angle undershoot of the combine mode excitation translates here into a lower tSNR.

Figure 4.1-3 displays a tSNR map of the slab acquisition overlaid on an EPI anatomical

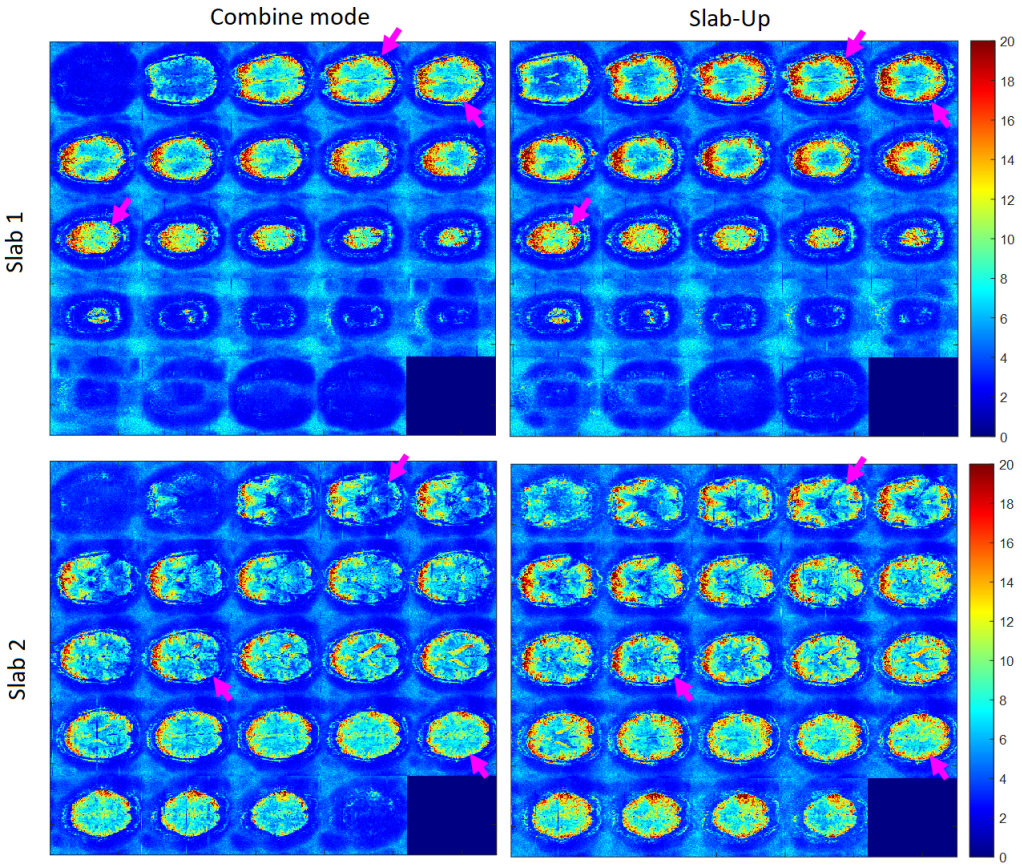

Figure 4.1-2: **tSNR maps from the 3D-EPI-UP in vivo for two slab configurations.** Images acquired on combine mode are displayed on the left and with the Slab-UP on the right. Pink arrows indicate areas where the Slab-UP yields a tSNR clearly superior then in combine mode.

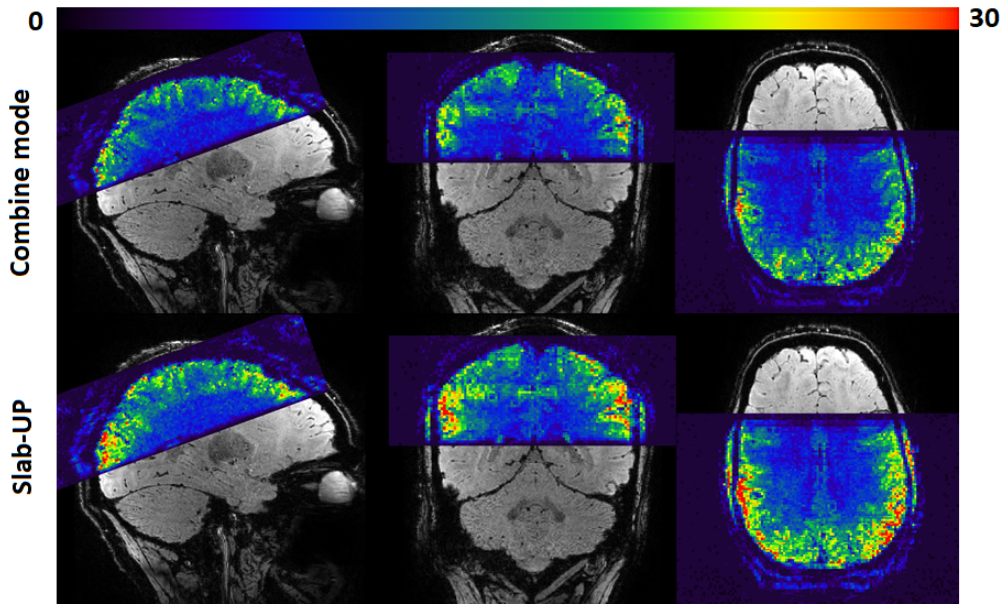

Figure 4.1-3: **tSNR maps overlaid on an anatomic EPI scan.** Top correspond to slab acquired in combined mode versus a slab acquired with a slab-UP in bottom. Here again the tSNR is clearly for the slab-UP acquisition is superior than combined mode. The slab thickness does not exceed the FOV. The high BTP of the slab-UP yields sharp slab profile compared to figure 3.1-2.

scan. Here again the tSNR from the slab-UP performs better than the combine mode. The acquired slab fits perfectly on the FOV and the high BTP allows a sharp profile of the slab, the signal quickly decreases at the edges of the slab allowing the FOV to be thinner, thereby reducing the acquisition time of few TRs. This will be especially beneficial at high resolution where the signal decrease will span more slices requiring thus more TRs to be acquired.

4.1.3 Discussion

We showed that the implementation installed on the 3D-EPI and the AFI allowed to play the slab-UP through modified arbitrary .ini files. After we showed via flip angle mapping that the slab-UP was correctly played and outperformed the combine mode. The improved RF field homogeneity was therefore in coherence with the improved tSNR maps acquired by the 3D-EPI-UP. However, AFI acquisition on the brain with the slab-UP performed on same areas as the two acquired EPI slabs would be preferable to link directly the tSNR (SNR) improvement brought by the slap-UP with its improved flip angle distribution over the brain.

This integrated framework required only three .ini files (one for each RF sub-pulse) instead of an overwhelming library of hundreds of .ini files with each one corresponding to a specific slab position, orientation and thickness. The central strategy in this approach hence was motivated by simplicity and robustness. The target was to have 3 k_T point pulses with reasonable durations homogenizing the whole 3D-brain, thus over any potential slab. The square sub-pulses then simply needed to be converted into sinc-like shapes superposed with slab-selection gradients to address the slab of interest. The latter was adapted dynamically with the position, orientation and thickness of the FOV with no influence on the gradient blips. The high TBP of the pulse resulted in a sharp slab profile which reduced the acquisition time by sparing the need to acquire more slices located at the slab edges. Otherwise, these slices must be acquired to avoid aliasing but are not exploitable due to their smaller signal.

4.2 Gradient delay diagnostic tool

Slab-UPs are sensitive to gradient delay artifacts because of their bipolar waveform parametrization. Unipolar shapes are immune to these effects but suffer from longer pulse durations and B_0 offst artefacts. These artifacts have been corrected with trim blips, but this correction depends on the slab orientation. Since the slab-selective gradient is generated dynamically by the 3D-EPI-UP sequence, the trim blip correction needs to be performed dynamically as well. This section introduces a simple online diagnosis tool to measure and correct for gradient delays. The concept is presented and is followed by preliminary results.

4.2.1 Principle and methods

The principle of this tool stems from the original delay measurement method from Gras and colleagues [Gra+17c] where a slice is acquired with a double spoke RF pulse. The two RF subpulses are dephased by 180° from each other meaning that they cancel each other out from a magnetization flip angle standpoint. Consequently, no signal ideally should be measured following such a pulse. However, in presence of gradient delays, the second RF subpulse experiences an additional phase offset ϕ_0 and the subpulses are dephased by $180° + \phi_0$ which result in a measurable signal. In the case of a 3D slab-selective excitation with no gradient

delay, the phase shift is not constant through the slices and the signal reaches a minimum only in the central slices where the phase difference is effectively 180°. In presence of gradient delays the signal is not minimal at the central location anymore.

The tool implemented consists simply in a slab selective double spoke RF pulse dephased by 180° in combine mode on which the user can apply an additional phase on the second pulse via the sequence protocol GUI. Practically it is performed by adding a gradient blip between the subpulses using the function generating the gradient blips (4.1.1). By acquiring images at different phase shifts and measuring the position where the minimum signal is reached, it is possible to roughly estimate the gradient delay for the specific axis on which the slab-selective gradient is run. From [Gra+17c] and 3.2.2, the phase offset that minimizes the signal (for an axial orientation) is

$$\phi_1 = 2\gamma G_{ss} z_1 \Delta t_z - \phi_{EC} \tag{4.2}$$

with γ the gyromagnetic ratio, z_1 the slice position, Δt_z the delay and ϕ_{EC} the zero order phase offset generated by eddy currents. If the experiment is reproduced with a different phase ϕ_2 then the minimum will be reached at a position z_2. Accordingly, the gradient delay is obtained by

$$\Delta t_z = \frac{\phi_1 - \phi_2}{2\gamma G_{ss}(z_1 - z_2)} \tag{4.3}$$

For a precise measurement of z_1 and z_2, the gradient amplitude must be high, and the slab position must be the furthest possible from the isocenter. To correct for the gradient delays, the user simply needs to choose the right phase offset that will put the minimum signal back at the central location of the slab. This phase offset is then saved and applied as trim blip to the slab-UP. It can be determined accordingly for each gradient axis. $\phi_E C$ is not corrected by this tool but can be estimated by placing the slab at the isocenter and using the same method as described above.

A phantom experiment was performed where the delay was measured and corrected on the axial direction. An axial slab of 6.5 cm thickness and shifted by 4.5 cm in the head direction was acquired at 2.5 mm isotropic resolution (TR/TE= 100/49.4 ms) with the tool implemented in the 3D-EPI sequence. Subsequently, tSNR maps of the same slab were then acquired (2.5 mm isotropic, TR/TE=54/28 ms) with and without trim blips applied to the slab-UP to illustrate the benefits of the gradient delay correction. Because the T1 of the phantom was unknown, it was not possible to set the RF excitation at the Ernst angle. Therefore, the goal of the experiment was to assess the homogeneity of the map rather than its value.

4.2.2 Results

Figure 4.2-4 shows the double RF spoke experiment with two different phase offsets, 180° and 180°+50°. The blue cross represents the center of the FOV and the axial view displays the middle slice of the FOV. The minimum signal is reached at the middle of the FOV when the phase offset is around 230° because the axial image has a low intensity compared to the acquisition with 180° phase shift. From both images we have $\phi_1 = 0°$, $z_1 = 3.87cm$, $\phi_2 = 50°$, $z_2 = 4.5cm$ and $G_{ss} = 9.82mT/m$. From equation 4.3, gradient delay on z axis is thus estimated to be $\Delta t_z = 2.66\mu s$. The estimation of z_1 and z_2 is made visually, the

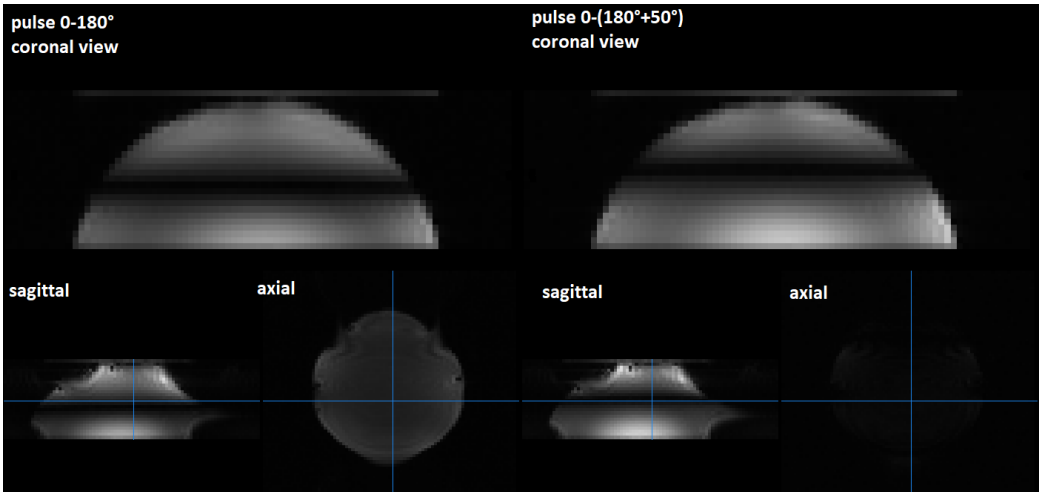

Figure 4.2-4: **Double RF spoke experiment with two different dephasing offsets.** On the left, the experiment is performed with a 180° net dephasing and on the right with a dephasing of 230°. The blue cross represents is located at center of the FOV. The axial view represents the middle slice of the FOV.

precision of the estimation relies on the resolution of the image and the intensity of the gradient delays which makes the dark band on the image thinner.

Figure 4.2-5 displays tSNR maps acquired with a slab-UP and a slab-UP with delay correction based on the trim blip method and the gradient delay measurement tool. We see here that the tSNR profile from the slab acquired with the gradient delay correction is more homogeneous. At such tSNR, the signal is in the thermal noise dominated regime meaning that the tSNR is a direct estimation of the SNR [TPW11]. The better SNR homogeneity suggests therefore a better flip angle homogeneity thanks to the trim blips, aside from inhomogeneous receive contributions. Because the slice orientation is purely transversal, only the estimation of the gradient delay along axis z was necessary for the correction.

4.2.3 Discussion and perspectives

We have described the concept of an integrated tool allowing to measure and correct for (potentially) anisotropic gradient delays in bipolar spoke waveforms. It relies on a double RF spoke pulse dephased by 180° experiment described earlier by [Gra+17c]. The tool allows to visually correct for the dephasing yielded by the gradient delays. The demonstration was performed on the axial orientation with an estimation of the delay on the z axis at 2.66 μs. In order to benchmark the performance of the correction, tSNR maps were acquired with a 3D-EPI sequence using the slab-UP with and without correction. As an estimation of SNR, the homogeneity of the maps was improved when employing trim blips. In this work, the Ernst angle was unknown, edge slices showed a higher tSNR meaning that the chosen flip angle was probably higher than the actual Ernst angle. Therefore, higher tSNR regions on the tSNR profile correspond to smaller flip angles.

* * *
* *
*

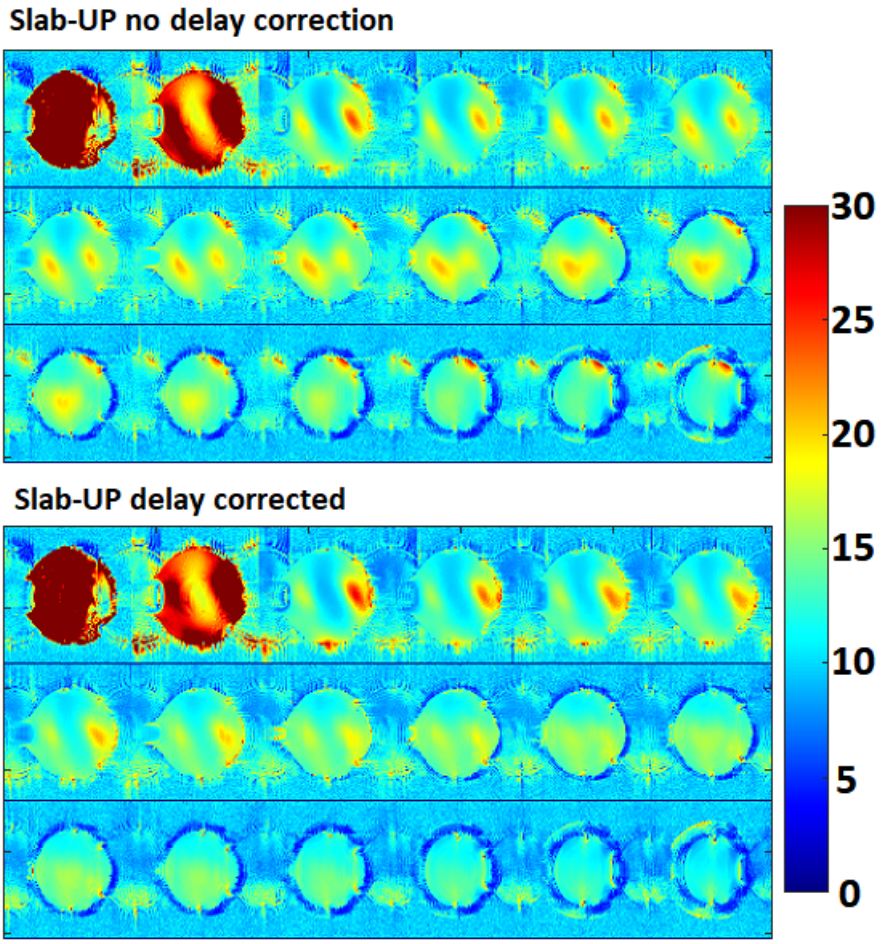

Figure 4.2-5: **tSNR map acquired with a slab-UP and with a slab-UP corrected for gradient delays. Axial view.** Top mosaic corresponds to the slab-UP acquisition and bottom one corresponds to the slab-UP with gradient delay correction. The tSNR map acquired with delay correction is smoother suggesting a smoother SNR and thus a more homogeneous RF magnetic field.

Chapter 5

Temporal SNR optimization through RF coil combination in fMRI: The more, the better?

Chapter Outline

5.1 Introduction . . . 72
5.2 Theory . . . 73
5.3 Materials & methods . . . 76
5.3.1 Sequence, pulse design and fMRI paradigm . . . 76
5.3.2 Data analysis and comparison strategy . . . 77
5.4 Results . . . 78
5.5 Discussion . . . 82
Contributions . . . 87

The work in this section has been published in a peer reviewed journal:

R. Jamil, F. Mauconduit, C. Le Ster, P. Ehses, B. A. Poser, A. Vignaud and N. Boulant. 'Temporal SNR optimization through RF coil combination in fMRI: The more, the better?' In: *PloS one* 16.11 (2021), e0259592

The purpose of this chapter is an attempt to optimize the tSNR through RF coil combination. Indeed, for functional MRI with a multi-channel receiver RF coil, images are often reconstructed channel by channel, resulting into multiple images per time frame. The final image to analyze usually is the result of the covariance Sum-of-Squares (covSoS) combination across these channels. Although this reconstruction is quasi-optimal in SNR, it is not necessarily the case in terms of temporal SNR (tSNR) of the time series, which is yet a more relevant metric for fMRI data quality. In this chapter, we investigated tSNR optimality through voxel-wise RF coil combination and its effects on BOLD sensitivity. An analytical solution for an optimal RF coil combination is described, which is somewhat tied to the extended Krueger-Glover model involving both thermal and physiological noise

covariance matrices. Compared experimentally to covSOS on four volunteers at 7T, the method yielded great improvement of tSNR but, surprisingly, did not result into higher BOLD sensitivity. Solutions to improve the method such as for example the t-score for the mean recently proposed are also explored, but result into similar observations once the statistics are corrected properly. Overall, the work shows that data-driven RF coil combinations based on tSNR considerations alone should be avoided unless additional and unbiased assumptions can be made.

5.1 Introduction

The blood oxygenation level-dependent (BOLD) functional MRI (fMRI) contrast increases with magnetic field strength [Zwa+09], but still represents only a few percent of signal change. Thermal noise, head motion, scanner instabilities and a variety of physiological phenomena such as breathing and cardiac pulsations potentially make the signal changes due to neural activations hard to detect reliably.

Current state of the art in MRI acquisition uses multi-receive channel RF coils to increase SNR [Roe+90] and benefit from parallel imaging [Pru+99; Gri+02]. In accelerated acquisitions that utilize GRAPPA, images from each receiver channel are often reconstructed individually, resulting in a multitude of images per time frame that are generally combined during reconstruction. The most standard coil combination to reconstruct a single image per time frame is the root Sum-of-Squares (SoS), due to its convenient implementation and SNR quasi-optimality [Lar+03]. A pre-whitening can be done at this stage for further performance by inserting the thermal noise covariance matrix computed from noise pre-scans [Roe+90; TPW11], a method labelled here covSoS. While solidly motivated by the theory in the thermal noise regime, the method however is not necessarily optimal in terms of temporal SNR (tSNR), indicative of signal stability and thus of more relevance for fMRI data quality. It has been well known that according to the model of Krueger and Glover [KG01], non-thermal sources of noise such as physiological noise and scanner instabilities can lead to a plateau of tSNR despite SNR boosts, even on phantoms [Zwa+09]. When benchmarking sequences with pilot tests before applying an fMRI paradigm on a cohort, as a result the temporal aspect of the signal or, ideally, the neural activations themselves should always be taken into account [Le +19]. Computed from the ratio of the activation spike amplitude over the standard deviation of the noise time-series, the functional Contrast to Noise Ratio (fCNR) is conceptually a very accurate metric to measure the quality of a task-based fMRI acquisition. However, because the location of the activations and their strengths are in theory unknown, tSNR has remained arguably one of the most popular metrics to guide the experimenter's choices [Tri+05].

tSNR mathematically consists of assessing signal stability through time for each voxel via the ratio of the mean to the standard deviation of the time-series. But because temporal-correlations may also exist [Bol+18], this metric has also been shown to be less well correlated with t-scores than the t-score for the mean, which in essence is the same as tSNR but after GLM analysis and thus taking temporal correlations into account [Cor+18]. Moreover, although the tSNR has already been shown to not correlate well with t-scores [Gei+07; DeD+16], it is still in general believed that the t-score versus tSNR relationship is an increasing function [Cor+18; MBB07].

Alternative coil combinations have already been proposed to specifically improve tSNR. Drawing the parallel with the thermal noise covSOS approach, Triantafyllou et al. [Tri+16] suggested considering the use of the time-series noise covariance matrix Ψ_t to account also for the physiological noise. Likewise, Huber et al. [Hub+17; Kas+18] proposed the STAbility weighted RF coil Combination (STARC) method consisting in a voxel wise tSNR optimized weighted sum of channels. Initially solved through a gradient descent method and thus hardly implementable into online reconstruction, we provide here an analytical solution to the problem, which turns out to exploit the total noise covariance matrix Ψ_t from Triantafyllou et al. [Tri+16]. Variants of this solution are also explored; the first consisted simply of optimizing the weights based on a pre-scan and then applying them to the fast-event fMRI scans. The second consisted of directly optimizing the t-score for the mean [Bol+18], which after GLM analysis, aimed at filtering out the activations while maximizing signal stability so that activations did not influence the computation of the weights. The revised STARC method and its variants are compared to covSoS through fMRI experiments on four healthy volunteers at 7T. Temporal SNR, activation maps, and scatter plots linking tSNR gains versus t-score gains are computed and compared. Example of optimization results with bar graphs and signal time courses are also provided to illustrate further the behaviour of STARC compared to covSoS.

5.2 Theory

Throughout this work, for a given image voxel K, we denote by $S_K(n)$ its $N_c \times 1$ complex signal vector at the volume repetition n through all receive channels with N_c the number of receive channels and A the matrix of dimension $N \times N_c$ concatenating the signal time courses from all coils of that voxel:

$$A = \begin{pmatrix} S_k(1)^H \\ \vdots \\ S_k(N)^H \end{pmatrix} \tag{5.1}$$

The tSNR is expressed as

$$tSNR = \frac{mean(I)}{std(I)} \tag{5.2}$$

where $mean(I)$ is the temporal mean of magnitude image voxel K, $std(I)$ its temporal standard deviation while I is the resulting voxel intensity after coil combination. The superscript H denotes Hermitian conjugate.

The SoS and covSoS combinations have their image voxel intensity computed as

$$I_{SoS}(n) = \sqrt{S_K(n)^H S_K(n)} \tag{5.3}$$

$$I_{covSoS}(n) = \sqrt{S_K(n)^H \Psi_0^{-1} S_K(n)} \tag{5.4}$$

The current gold standard is the covSoS approach where the $N_c \times N_c$ channel covariance matrix Ψ_0 computed from noise only pre-scans (scans without RF) is inserted between signal vectors. When Ψ_0^{-1} is decomposed into its Cholesky form, this operation can be seen as a pre-whitening process uncorrelating the channels and penalizing the noisiest ones.

In [Tri+16], Triantafyllou et al. extended the Krueger-Glover model by substituting to the scalar coefficient expressing the effective strength of the physiological noise with a

physiological noise covariance matrix Ψ_p such that the time-series covariance matrix Ψ_t, calculated from the covariance matrix of A, could be separated into $\Psi_t = \Psi_0 + \Psi_p$. The paper concluded by suggesting that Ψ_t could thereby be leveraged in the coil combination to optimize tSNR, just as the covSOS approach does for SNR, as intuition would dictate:

$$I_{covSoSt}(n) = \sqrt{S_k(n)^H \Psi_t^{-1} S_K(n)} \; with \; \Psi_t = \mathrm{Cov}\,(A) \tag{5.5}$$

Originally introduced by Huber et al.,STARC [Tri+16] is a voxel-wise data-driven tSNR optimization yielding a weighted sum of channels written as $I_{STARC} = AX$ with X the $N_c \times 1$ coil combination vector to determine for each voxel. Here A is concatenated with magnitude signal vectors:

$$A = \begin{pmatrix} |S_k(1)|' \\ \vdots \\ |S_k(N)|' \end{pmatrix} \tag{5.6}$$

The STARC problem was originally written as

$$X = \arg\max_X \frac{mean(I_{STARC})}{std(I_{STARC})} \tag{5.7}$$

The optimization had to be performed on each voxel independently via a gradient descent method and was thus time-consuming. However, it is possible to provide an analytical solution to this problem by recasting it as

$$X = \arg\min_X Var(I_{STARC}) \tag{5.8}$$

$$s.t.\; E(I_{STARC}) = b \tag{5.9}$$

where $E(I_{STARC})$ and $Var(I_{STARC})$ denote respectively the expectation and the variance values of the time signal ISTARC. Their respective expressions are

$$E(I_{STARC}) = u'X \tag{5.10}$$

$$Var(I_{STARC}) = \frac{1}{N} X'(A'A - uu')X \tag{5.11}$$

$$= X'\mathrm{Cov}\,(A)X \tag{5.12}$$

with u the $N_c \times 1$ columnwise (temporal) mean vector of A and $\mathrm{Cov}\,(A)$ is the covariance matrix of A. b is an arbitrary scalar and can be set to $b = mean(I_{SoS})$ so that after optimization the mean temporal image is conveniently the same as for SOS. As a result, the optimization problem is a quadratic program under a linear constraint whose solution satisfies the Karush-Kuhn-Tucker (KKT) conditions [Noco6]. The Lagrangian multiplier method yields for the Lagrangian

$$L(X, \lambda) = X'\mathrm{Cov}\,(A)X + \lambda(u'X - b) \tag{5.13}$$

with λ the Lagrange multiplier. The solution can be found by setting the derivatives of the Lagrangian with respect to X and λ to zero such that

$$\begin{cases} \frac{\partial L}{\partial x} = 2\Psi_t X + \lambda u = 0 \\ \frac{\partial L}{\partial \lambda} = uX - b = 0 \end{cases} \tag{5.14}$$

The solution then is $X = -\frac{\lambda \mathrm{Cov}\,(A)^{-1}u}{2}$ with $\lambda = \frac{-2b}{u'\Psi_t^{-1}u}$ to meet the constraint so that

$$X = \frac{b\Psi_t^{-1}u}{u'\Psi_t^{-1}u} \tag{5.15}$$

Conveniently in this final expression b and the denominators are scalars and therefore can be potentially omitted with no impact on the tSNR. The STARC voxel intensity thus finally simplifies to $I_{STARC} = A\Psi_t^{-1}u$.

This expression has some similarities with the one of covSOSt in that both exploit the time-series covariance matrix, but they are not identical. This result can already provide hints on the behaviour of STARC: because it uses the inverse of the time-series covariance matrix Ψ_t^{-1}, STARC will penalize the channels with the highest variability, regardless of its origin (neural activations or noise). We will experimentally show that this type of combination indeed greatly improves tSNR. But it comes at the cost of weaker t-scores because activation spikes are not dissociated from the rest of signal variability.

Therefore, in order to ignore activation-related signal fluctuations during the STARC optimization, a first simple solution would be to calibrate the weighting vector X based on a separated in vivo pre-scan acquisition with no stimuli and apply it to the fMRI acquisition, assuming reproducibility. We will denote this coil combination $STARC_{ps}$.

A second alternative consists of replacing the tSNR as cost function by the t-score for the mean described by Corbin et al. [Cor+18], yet still neglecting temporal correlations to preserve an analytical solution for simplicity. The t-score for the mean of a voxel is the ratio of the temporal mean of the signal by the standard deviation of its residual after the General Linear Model fit (GLM). For clarity, the key aspects are reminded here. The detection of BOLD signal in fMRI exploits the General Linear Model [WF95], which describes the voxel-wise fMRI signal I with a design matrix D containing the explanatory variables such that

$$I = D\beta + \varepsilon \tag{5.16}$$

with β,the regression coefficients estimated via least squares method and ε the residual of the estimation assumed to follow a centred Gaussian distribution. Their respective expressions are

$$\beta = (D'D)^{-1}D'I = D^{+}I \tag{5.17}$$

$$\varepsilon = I - D\beta = (Id - DD^{+})AX = PAX \tag{5.18}$$

where Id is the identity matrix and D^{+} the pseudo inverse of D. The matrix P defines a projection because $PP = P$. The typical method to infer on neuronal activations uses t-score statistics to assess the significance of given explanatory variables on the fMRI signal. The t-score is calculated with

$$t = \frac{c'\beta}{\sigma_\varepsilon \sqrt{c'(D'D)^{-1}c}} \tag{5.19}$$

where c is a vector selecting a specific contrast. σ_ε^2 is the variance of ε computed as

$$Var(\varepsilon) = \sigma_\epsilon^2 \tag{5.20}$$

$$= \frac{1}{N}X'((PA)'PA - u_{PA}u'_{PA})X \tag{5.21}$$

$$= X'\mathrm{Cov}\,(PA)X \tag{5.22}$$

$$= X'\Psi_{tsm}X \tag{5.23}$$

with u_{PA} the column-wise (temporal) mean of PA. By the same token, just like for the STARC optimization, consequently optimization of the t-score is written as

$$X^* = \arg\min_X Var(\varepsilon) \tag{5.24}$$

$$s.t.\ c'\beta = c'D^+AX = b \tag{5.25}$$

where b is again an arbitrary scalar. The t-score for the mean metric makes use of the expression of t where c is made of zeros everywhere except one at the index corresponding to the column of the design matrix fitting the mean of the signal (hence the name "t-score for the mean"). The t-score for the mean as a result can be interpreted as a tSNR where the standard deviation of the signal is calculated in the vector space orthogonal to the subspace spanned by the columns of D (i.e. its image). That way, noise evaluation elegantly disregards what is believed to be activations. The function to maximize here is the t-score for the mean, the solution is found to be

$$X = -\frac{\lambda \mathrm{Cov}\,(PA)^{-1}c'D^+A}{2} \tag{5.26}$$

$$= -\frac{\lambda \Psi_t^{-1}u_{tsm}}{2} \tag{5.27}$$

through the same Lagrangian multiplier method as for the STARC optimization. Finally, the expression for the coil combination optimizing for the t-score for the mean yields for image intensity $I_{STARCtsm} = A\Psi_{tsm}^{-1}u_{tsm}$ (omitting again scalar coefficients with no impact on the t-scores). The pseudo-code for the t-score of the mean optimization is provided in Appendice.

Because this strategy actively uses the GLM design matrix D for denoising, the degree of double-dipping [Kri+09] to which $STARC_{tsm}$ is prone has to be determined. t-scores normally follow the Student's t-distribution, but in the case of a high number of degrees of freedom (>30), this distribution is in practice set to be equivalent to a standard normal distribution of mean zero and standard deviation of one when there is no activation (null hypothesis). Double-dipping bias will be confirmed if $STARC_{tsm}$ does not follow this distribution.

5.3 Materials & methods

5.3.1 Sequence, pulse design and fMRI paradigm

This study was approved by the local ethics committee and four healthy volunteers were scanned after providing written informed consent. In vivo experiments were performed on a Magnetom 7T (SiemensHealthineers, Erlangen, Germany) with software version VB17A step 2.3 and equipped with a parallel transmission (pTX) 8Tx/32Rx head coil (Nova Medical, Wilmington, MA, USA).

For each volunteer, anatomical scans were performed with a 0.8 mm isotropic resolution MPRAGE sequence and functional scans were acquired with 3D-EPI [Pos+10]. Imaging parameters for the MPRAGE were TR/TI/TE 2600/3.44/1100 ms, flip angle (FA) 4°, 192 sagittal slices, FOV 256 mm, acceleration factor 2 with GRAPPA. Parameters for the 3D-EPI were chosen to be as close as possible to the ones from the 7T Human Connectome Project (HCP) resting-state fMRI protocol. Parameters were: TR/TE 55/22 ms (TRvol

= 1.2 s), 88 sagittal slices, 1.6 mm isotropic resolution, FOV 208 mm, acceleration factor 2×4, partial-Fourier (PF) 7/8, CAIPI shift $\Delta k_z = 2$, BW = 1832 Hz/Px, Posterior to Anterior phase encoding, total acquisition time 5:26 mins for 260 repetitions. A brief 3D-EPI scan with the same parameters was acquired with an inverted phase encoding (Posterior to Anterior) for distortion correction.

To improve the RF transmit field, universal pulses [Le +19; Gra+17b] were specifically designed for the 3D-EPI sequence via an offline optimization algorithm, using a database of 20 B_1/B_0 field maps. Flip-angle normalized root mean square error was reduced from 21% in CP-mode to 12% with universal pulses. The optimized pulse was a three kT-points RF pulse of flip-angle 15° and 3 ms total duration for water selection [Le +19].

In order to assess the differences in BOLD sensitivity between the different RF coil combinations, a localizer fMRI paradigm was used [Pin+07]. It is a fast event-related fMRI paradigm consisting of a succession of ten types of stimuli such as checkerboard, auditory/visual sentences, calculations and right/left clicks.

5.3.2 Data analysis and comparison strategy

The 3D-EPI data were reconstructed with a custom GRAPPA reconstruction code and yielded uncombined channel images. The three dimensional time series obtained after each coil combination were normalized so that their mean temporal signal was set equal to the mean temporal of SoS and then saved into NifTI format. Image alignment, 2 mm3 FWHM Gaussian spatial smoothing and brain normalization on 2mm3 MNI were done with SPM12 [Fri+94]. A distortion correction was performed with topup [ASA03] from the FSL library (FMRIB, Oxford UK) between image realignment and registration steps. The GLM design matrix included task onsets convolved with a canonical hrf with their first derivative, signal drift, mean and six motion regressors (three translation, three rotations) obtained from the motion compensation post-processing step (after coil combination).

For all volunteers, we implemented the covSoS, STARC, $STARC_{ps}$ and $STARC_{tsm}$ combinations from the same acquisitions to ensure a fair comparison. Only the coil combination differed. An additional acquisition with the same sequence and parameters of 100 repetitions with RF but without any stimuli was performed in order to obtain optimised weights; the weights were then applied on the uncombined fMRI data to get the $STARC_{ps}$ reconstruction. tSNR maps were computed by taking the ratio of the temporal mean to the standard deviation over the 260 volumes. For each coil combination, boxplots of the tSNR distributions pooled on the four volunteers were also computed with a brain mask to exclude non-brain voxels. By fitting the post-processed data with the GLM, SPM returned t-score maps as indication of activation strength. Apart from visual qualitative analysis to ensure no absurd activated clusters, quantitative analysis consisted in the evaluation of the number of activated voxels for different p-values and for each coil combination strategy. In order to analyze the link between tSNR and t-score, we generated a scatter plot of the tSNR ratio STARC/covSoS versus the t-score ratio STARC/covSoS. Likewise, to determine whether an increase in t-score for the mean is sufficient to get an increase in t-score, we also generated a similar plot of the t-score for the mean ratio STARC/covSoS versus the t-score ratio STARC/covSoS. Activated voxels from motor and auditory contrast activation maps (covSoS) were considered. A regression coefficient was computed for each plot in which

all points were pooled together. Monte Carlo simulations were performed to evaluate the tendency of $STARC_{tsm}$ to double-dipping. 32 Gaussian random noise waveforms (one for each receive element) with 260 points each were generated. Their mean was uniformly and randomly distributed between 0 and 50 and the noise level was set to be 5% of the weakest signal mean. No correlations among the channels were imposed. The null hypothesis for t-score testing assumes no activation; therefore, no activations were added to the waveforms. These signals were combined with the covSoS method and $STARC_{tsm}$, as presented in the Theory section. The thermal noise covariance matrix input was the noise level squared times the identity matrix. Simulated covSoS and $STARC_{tsm}$ signals were then fitted with the GLM and a t-score was calculated for a single task contrast and saved. The design matrix used was the same as the one used for the in vivo experiment excluding motion regressors. This process was repeated 105 times to yield a smooth t-score probability density function for covSoS and $STARC_{tsm}$. In order to understand how STARC sets the weights for each channel, the mean, the standard deviation and the optimized weights for each channel were displayed by means of bar plots for two activated voxels. Scatter plots of the mean versus the standard deviation across receive channels were also displayed for each voxel, a linear fit including the ten strongest channels was plotted on top of them. Finally, the time series of two activated voxels (according to auditory and visual covSoS contrast maps $p<0.001$) were plotted for covSoS and STARC coil combinations. All time series had their mean previously normalized to allow a fair comparison. The time-series of the stimuli onsets convolved with the canonical hrf was likewise displayed to ease the distinction between noise and activations.

5.4 Results

Before exploring the results, we briefly remind for clarity the key principles of each coil combination. STARC is a weighted sum of channels optimized to yield the best tSNR for each particular run. The tSNR of a voxel is defined here by the ratio of its temporal mean and its standard deviation. Because neuronal activations have also an influence on the tSNR, two other modified STARC versions were investigated. STARCps consists in optimizing the weights on a task-free scan and then applying them to the fMRI scans. Finally, STARCtsm is a weighted sum of channels optimized to yield the best t-score for the mean. The t-score for the mean is similar to tSNR but normalized by the standard deviation of the residuals of the GLM. Believed neuronal activations are thus not included as noise.

Fig 1 reports the tSNR returned from covSoS, STARC, $STARC_{ps}$ and $STARC_{tsm}$ coil combinations. STARC showed the best overall tSNR performance up to a twofold tSNR increase compared to the gold standard covSoS. $STARC_{tsm}$ also greatly improved tSNR but not as much as STARC, indicating the influence of the potential activations on the tSNR evaluation. On the other hand, $STARC_{ps}$ did not improve tSNR at all compared to covSoS which shows that the optimized weights can be scan dependent.

Fig 2 displays activation maps, from the same volunteer as in Fig 1. While STARC yielded the highest tSNR, it performed poorly compared to the covSoS in terms of BOLD detection. Its activation map has smaller clusters and weaker t-scores. $STARC_{tsm}$ (without correction of the statistical bias induced by double-dipping) apparently improved the detectability since potential activations were removed before optimization. Given the fact that $STARC_{tsm}$ yields a slightly smaller tSNR, we see that part of the preserved variations is linked to

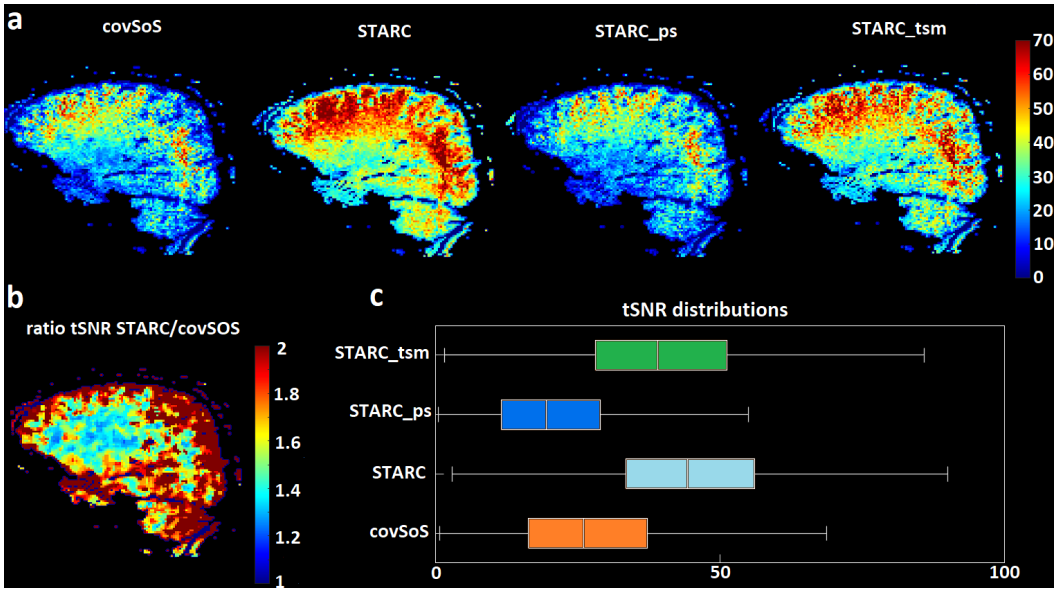

Figure 5.4-1: **tSNR results.** a - tSNR map from the same volunteer, scan and sagittal slice after covSoS, STARC, $STARC_{ps}$ and $STARC_{tsm}$ coil combinations. STARC yielded the highest tSNR map. b - Ratio of STARC and covSoS tSNR maps after median image filtering. STARC always improves tSNR, up to a factor 2. c - tSNR distributions pooled across all volunteers. Overall, STARC outperforms the other coil combinations in terms of tSNR. A brain mask was used to ignore non brain voxels.

neuronal activity. $STARC_{ps}$ shows again the lowest performance confirming that calculated weights here are irrelevant if used on different scans. Moreover, since the method is a voxel-based optimization, inter-scan motion can also make the weights suboptimal.

Fig 3 shows for each activated voxel the effect of tSNR improvement on BOLD detection. All plotted voxels have an improved tSNR thanks to STARC coil combination but their t-score is for most of them reduced. The regression coefficient of -0.41 suggests that tSNR not only is poorly correlated with t-scores but also indicates a negative trend when using such data-driven optimization approaches. An increase of tSNR with STARC can lead to an increase of t-score for the mean, though non-linear [Cor+18]. Yet again, Fig 3B shows in this case poor correlation between t-score for the mean and t-scores, when using the proposed strategy. The few voxels where the tSNR is reduced after STARC are likely due to the combination of no tSNR improvement and successive post-processing operations that slightly reduced the tSNR.

Fig 4 shows that the null hypothesis of $STARC_{tsm}$ seems to have a distorted distribution compared to covSoS with a higher variance. The distortion is significantly different to covSoS ($p < 0.05$). A simple solution consists in dividing the t-statistics of STARCtsm by the standard deviation characterized here under the null hypothesis, to enforce a standard normal distribution. This double-dipping correction reduced the number of activated voxels by almost a factor of 2.

Fig 5 shows by means of bar plots for two different voxels located in grey matter, how distributed the weights are across channels depending on the signal strength. Because there is a clear correlation between signal strength and signal variability, the STARC approach promotes channels with weak variance and thus of weak signal. Moreover, if the signals between two channels are highly correlated, e.g. when there are activations, then STARC can

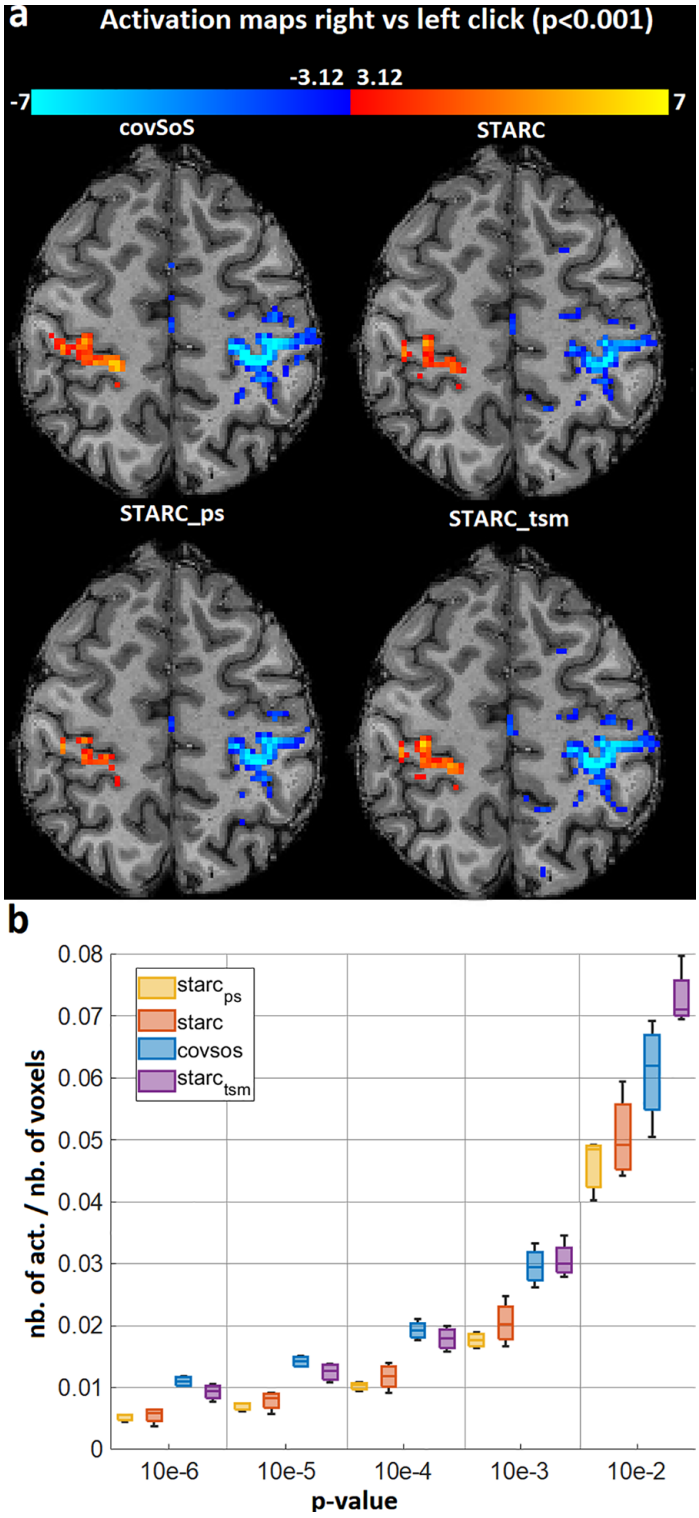

Figure 5.4-2: **Activation results.** a - Activation maps for the motor contrast at p<0.001 (no correction) for covSoS, STARC, $STARC_{ps}$ and $STARC_{tsm}$. No double-dipping correction was applied to $STARC_{tsm}$. The shown maps are from the same volunteer as in Fig 1. b - Total number of activated voxels relative to the total number of voxels at different p-values and for different coil combinations, pooled over the volunteers. $STARC_{ps}$ and STARC have the poorest performance in terms of BOLD detection. CovSoS has the highest number of activations for the lowest p-values but $STARC_{tsm}$ (without double-dipping correction) reports more activations for the highest p-values.

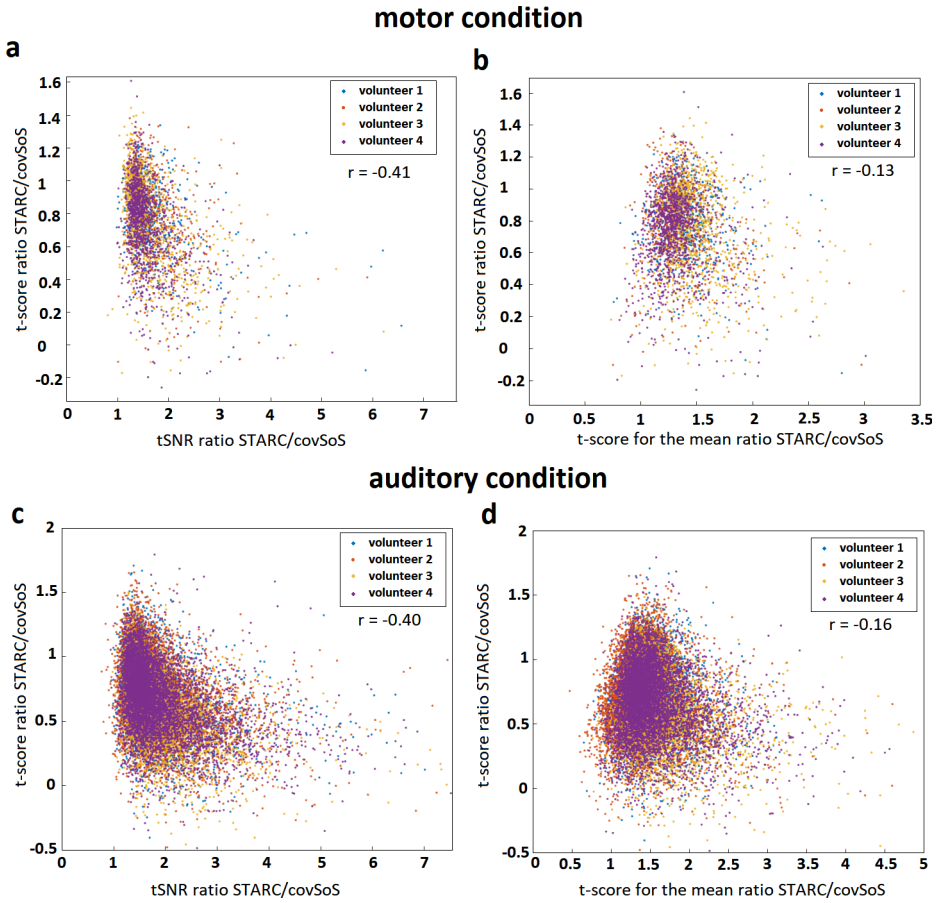

Figure 5.4-3: **t-score gains versus tSNR or t-score for the mean gains.** a - Scatter plot linking the activated voxels, the tSNR gain with STARC to its t-score gain for motor contrast. b - Scatter plot linking the t-score for the mean gain with STARC to its t-score gain for motor contrast. c - Same plot than a but with auditory contrast. d - Same plot than b but with auditory contrast. Each point corresponds to an activated voxel ($p<0.001$) according to the covSoS combination maps. In general, an increase of tSNR did not yield a better t-score.

subtract one to another to remove them. The linearity between mean and standard deviation in the scatter plots favours the physiological noise regime hypothesis because thermal noise is not proportional to signal strength. Here, the slope of the fit corresponds to a rough estimation of 1/tSNR. However, we see that the weakest channels have their respective points not aligned with the others suggesting that the weaker the signal, the more the noise will be in the thermal regime. Even is the combination was based on multiple voxels (say a roi of few centimeters), this result shows that the algorithm will fall into the same pitfall by promoting weaker receive channels.

Fig 6 plots the time series from covSoS and STARC combinations from the same activated voxels. covSoS time series yield the highest activation peaks but also has the highest variability. In the end, even if STARC has the highest tSNR (tSNR covSoS/STARC 35.4/67.6 and 67.2/85.0 for the first and second voxels respectively), the t-scores will be smaller than for covSoS (t-scores covSoS/STARC are 14.1/9.1 and 11.8/8.5 for the first and second voxel respectively). The chosen voxels here were strongly activated, which translates into very high activation peaks. These peaks representing the bulk of signal variability are thus reduced to increase tSNR with STARC.

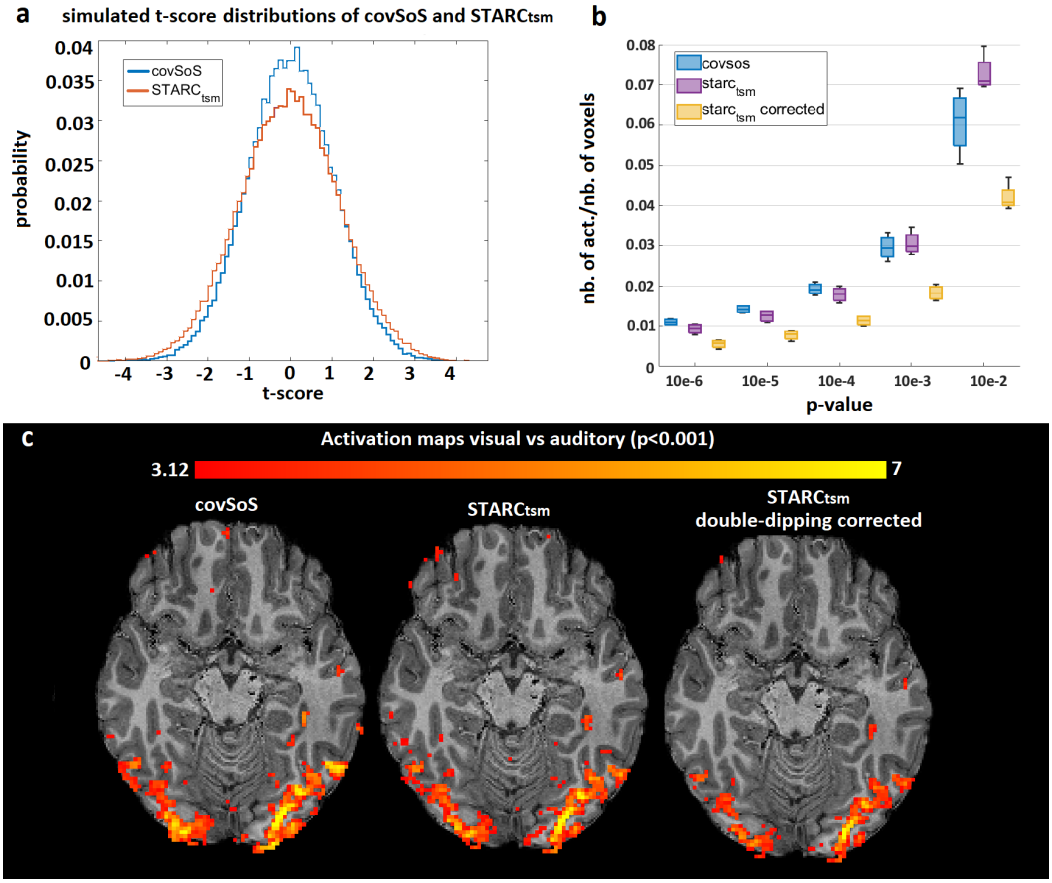

Figure 5.4-4: **Double-dipping results.** a - T-score distributions of covSoS and STARCtsm from noise signals and Monte Carlo simulations. The distribution of STARCtsm under the null hypothesis is distorted compared to covSoS because of double-dipping. b - Total number of activations relative to the total number of voxels at different p-values and for covSoS, STARCtsm and its double dipping corrected version for the in vivo scan. After correction, the number of activations from STARCtsm markedly drops. c - Activation maps on one volunteer for visual vs auditory contrast at $p<0.001$ (no correction). After double-dipping correction, activations are weaker and clusters smaller.

5.5 Discussion

Motivated by the stagnation of tSNR despite the increase in SNR in the presence of scanner instabilities and/or physiological noise, and by the preference of tSNR over SNR as quality metric in fMRI, we investigated in this work tSNR and t-score for the mean optimality through voxel-wise data-driven coil combinations.

We showed that optimality could be reached for each voxel in the image by providing the right formulation of the optimization problem. Minimizing the temporal variance of the resulting signal while having its mean equal to an arbitrary constant yielded an analytical solution that uses the coil-to-coil (total) noise covariance matrix. Despite a great improvement of tSNR, activation maps obtained after STARC coil combination were not as good as those from covSoS. Indeed, signal variation contains noise but also neuronal activations. By reducing the variations, noise was reduced but activation spikes were reduced too. By looking closer at the coil combination weights, STARC penalizes the coils with the highest signal and promotes the weakest ones because the physiological noise or activations are most of

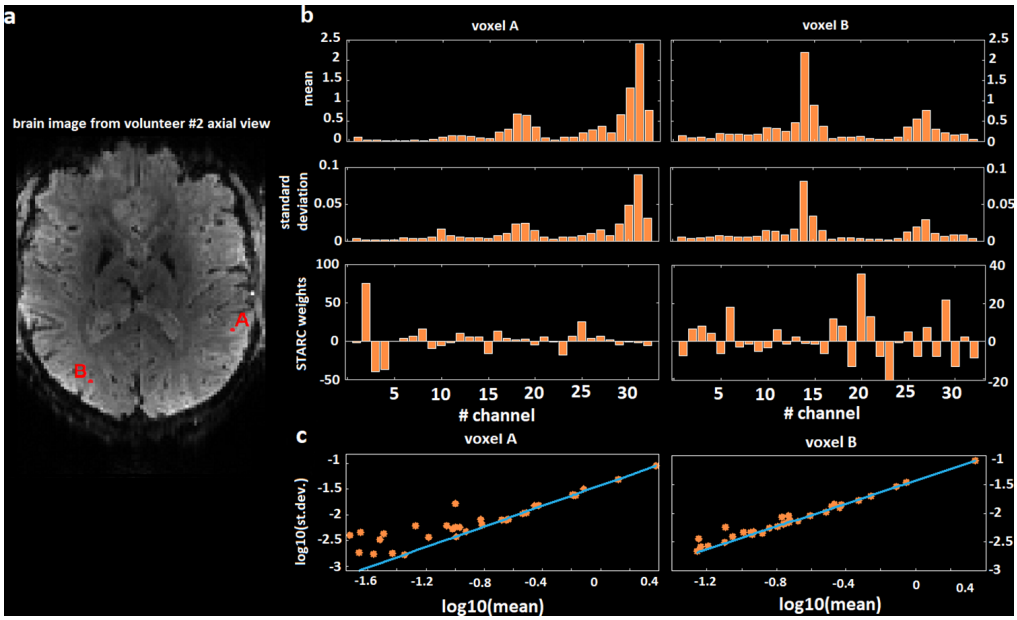

Figure 5.4-5: **Weights distributions from STARC optimization for two voxels.** a - Brain image from volunteer #2 axial view, the red points labelled A and B are the voxels whose weights are analysed. b - For both voxels A and B, the bar plots display the temporal mean, the temporal standard deviation and the optimized STARC weights. The channels receiving the strongest signal have the highest variability but will be given the lowest weight. c - Scatter plot of the mean versus the standard deviation for each channel, the slope of the linear fit of the ten strongest channels is also plotted. The signal variability is highly proportional to the signal strength.

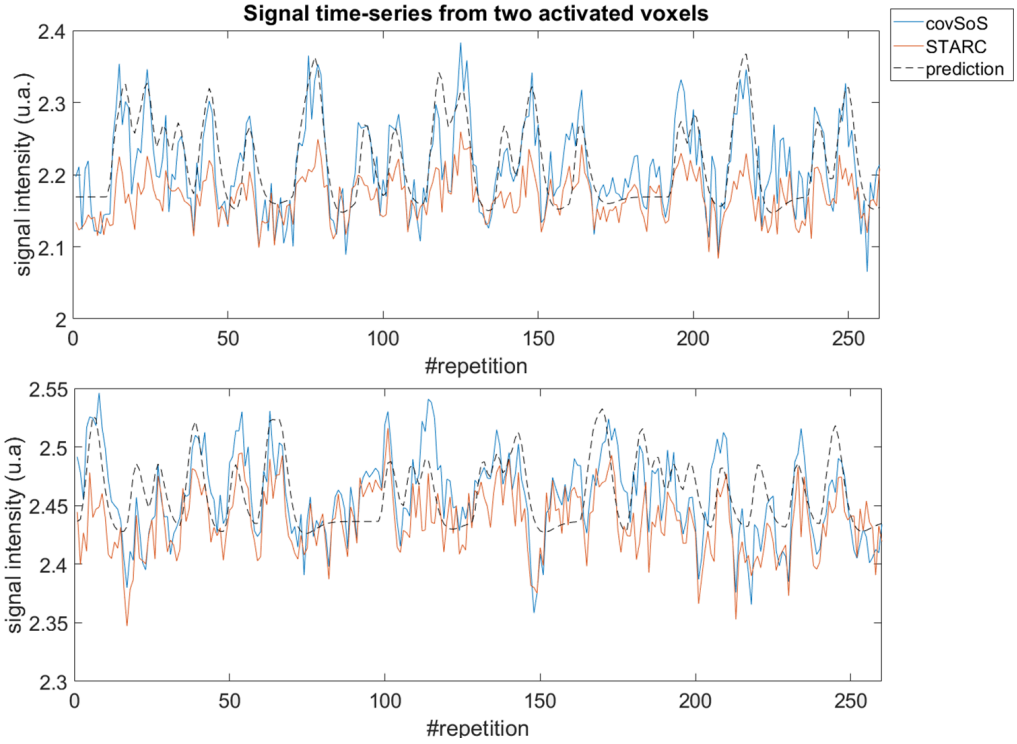

Figure 5.4-6: **Signal time series for two activated voxels for covSoS and STARC.** A time series of the stimuli onset convolved with the canonical hrf is also displayed. Each graph corresponds to a voxel. CovSoS has higher activation peaks than STARC but the latter has the highest tSNR.

the time proportional to signal strength while thermal noise can be roughly constant across all coils. This means that the STARC signal for a given voxel location will be mostly made from the receive coils that are the farthest to that location. Moreover, the poor results in tSNR and t-score from the pre-scan strategy ($STARC_{ps}$) show that the optimization can be scan-dependent despite the use of the same sequence with same settings. The covariance matrix of the signals across channels (Ψ_t) indeed can be sensitive to the particular signal instance or random noise sample. Unless the time-series are particularly long, the covariance matrix calculated with modestly long time series will exhibit fluctuations. This gives to the STARC approach an "opportunistic" behaviour when it comes to reduce the signal variability. The most extreme scenario would be a time-series of length Nc, where STARC would return infinite tSNR (assuming linear independence of the Nc signals), i.e. no signal variation. Applying the same optimized weights on another time-series would not return the same result because of a different noise sample.

The STARC method was unable to distinguish physiological noise from neuronal activity without any a priori while no assumptions about the nature of the noise or its statistics here were made. This motivated the change of strategy by optimizing the t-score for the mean instead of tSNR. Mathematically, it was shown to be a projection of the STARC problem onto a space orthogonal to the one spanned by the design matrix of the fMRI experiment. By doing so, potential activations were removed prior to variance minimization and an analytical solution again could be obtained. This strategy allowed having more activations than STARC but, as the Monte-Carlo simulations showed, this was an illusory consequence of double-dipping [Kri+09]. Once the null-hypothesis was characterized properly, the necessary corrections revealed no gain compared to covSOS. The optimization recipe provided in fact can be applied for any contrast optimization, but would lead again to double-dipping.

The t-score results of STARC do not follow those from the original abstract [Hub+17] but they confirm the results from a pilot experiment [Kas+18] where STARC returned also lower t-scores at higher resolution acquisitions, i.e. more in the thermal noise regime. The discrepancy could be temptingly explained by the fact that the original STARC algorithm consisted in a gradient descent with maximum and minimum constraints on the weights. These constraints could have possibly alleviated the destructive effects of the approach on the activations. Since an analytical solution was obtained, we wanted in this study to not include such constrains but rather emphasize the risks of searching for the best tSNR possible in data-driven optimization approaches. Despite the agreement between our observations and the results described in [Kas+18], we do not rule out the possibility of obtaining more activations in some other fMRI protocols based on such data-driven optimization principles.

In their paper [Tri+16], Triantafyllou et al. extended the KG noise model by adding a new term to its expression. They defined it theoretically as not scaling with signal strength. They confirmed experimentally its physiological noise origin by showing that the value of this term was higher on in vivo than on phantom acquisitions. They proposed examples of noise that do not scale with signal strength. These being seen simultaneously across channels, it can also presumably be reduced with linear combinations as in STARC. In our case, the strong proportionality between signal strength and signal variability shown in Fig 5 suggests that this type of noise here did not have an important influence on the STARC weights.

tSNR can increase if the signal mean increases (with constant or slower increase of variance) or if the variance decreases (with constant or slower decrease of mean). If the tSNR

is computed on acquired fMRI scans, both cases do not necessarily represent a favourable situation to see more activations, because in the first case, the physiological noise is most of the time proportional to signal temporal mean [KG01; Tri+16] and in the second case minimizing all signal variations can erode activation spikes. Although tSNR still remains an interesting metric to benchmark sequence settings, these results shed light on its limits. The results of this work suggest that tSNR should not be considered alone when evaluating or comparing acquired in vivo data because it contains neuronal fluctuations. The t-score for the mean is an interesting alternative to tSNR that does not take into account neural activity. However, we showed that an increase in the t-score for the mean is neither a necessary nor a sufficient condition to get an increase in t-score, but it depends on the strategy with which the t-score for the mean increase is obtained [Cor+18].

In conclusion, we presented tSNR and t-score for the mean optimal coil combination methods. Despite the proven optimality of these coil combinations for these data quality measures, activation maps did not improve compared to the gold standard covSoS coil combination, thereby indicating potential limits of tSNR and t-score for the mean metrics when assessing the quality of already acquired fMRI data. Although their approximate nature had already been reported in the literature, this work emphasizes the pitfalls associated with data-driven optimization approaches. Moreover, introducing prior information about the activations through the use of the GLM design matrix failed to outperform the covSoS coil combination method, once the statistical bias was taken into account properly. Although the theory leading to covSoS does not incorporate non Gaussian temporal fluctuations related to scanner instabilities or physiological noise, it appears that it remains so far more reliable for fMRI than data-driven coil combination methods being able to boost tSNR.

* * *
* *
*

General Conclusion

The 11.7T Iseult MRI represents a powerful tool to explore the human brain at higher resolution. Its ultra-high operating magnetic field enables an increase in SNR that can be invested into higher resolution imaging fMRI protocols. The goal of this work was to deliver a sequence capable of exploiting the MRI at its full potential. Contributions of this work include RF pulse design, artifact correction, sequence programming and reconstruction methodology.

Contributions

First, strategic choices had to be made on the RF pulses. Ultra-high field MRI suffers from severe RF field inhomogeneities, but parallel transmission coupled with appropriate RF pulse design can reduce them. Therefore, the first part of this work focused in designing RF pulses alleviating these B_1^+ artifacts. Universal k_T-point pulses [Clo+12] were optimized for slab-selective excitations. On one hand, the k_T-points parametrization approach allows optimizing RF pulses alleviating B_1^+ artifact while respecting SAR and hardware constraints. On the other hand, the Universal Pulse approach [Gra+17b] with k_T-points or spokes removed the burden of acquiring extra scans and performing an RF pulse optimization *in situ*.

Finally, coping with the current performance of commercially available gradients, the slab-selective approach allows having a smaller field of view and thus smaller acquisition times compared to a full brain acquisition with the same sequence parameters. We motivated the use of bipolar gradient shapes over unipolar for their shorter duration, and their robustness against susceptibility artifacts. These pulses suffer however from gradient delays originating from hardware imperfections and eddy currents but a published work [Jam+21a] proposed a general method to remove the resulting artifacts for any orientation or gradient anisotropy by using trim blips. Overall, the pulses performed better than RF shimming in terms of flip angle homogeneity.

The second strategic choice to adopt was about the implementation of the pulse. A single pulse was optimized on the whole brain to avoid a cumbersome library of pulses for each slab thickness and orientation, and then by adjusting the pulse parametrization (sinc-like shapes) and adding selection gradients for the excitation to ultimately become slab-selective. The plug-and-play philosophy was then extended to slab-selective Universal Pulses by implementing a sequence module allowing to generate dynamically a slab-selective gradient shape adapted to the desired Field Of View. This module being sequence agnostic,

it could be implemented likewise in the AFI sequence and starts producing results in SPACE, MPRAGE and GRE slab-select acquisitions. Because gradient delay correction is dependent on slab orientation, a small tool also was implemented allowing a fast, visual and online measurement of the gradient delay as well as a dynamic correction adapted to the slab orientation. This tool could be automatized to improve the precision of the estimation and reduce the duration of the delay measurement process. These modules were integrated into the 3D-EPI sequence provided by Rudïger Stirnberg (DZNE Bonn, Germany), to be later part of the PASTeUR sequence package. They also start being integrated and tested in other sequences of the package (SPACE, MPRAGE, GRE).

Finally, motivated initially by the STARC method for image formation, we explored in [Jam+21b] different receive coil combinations for fMRI. Two analytical solutions were provided by optimizing either the temporal SNR or the t-score for the mean. Despite a great increase of these metrics, we showed that their maximization tended to erode activation spikes. Consequently, we suggest that tSNR should not be considered alone when assessing the quality of an fMRI acquisition and that caution should be taken when data-driven optimizations are conducted.

* * *
* *
*

Appendices

Appendix **A**

Résumé en français

Abstract in French

Sujet : Développement d'une séquence d'IRM fonctionnelle à haute résolution spatiale et à haut-champ

Nous résumons ici les différents aspects de cette thèse. Après avoir donné le contexte et les motivations qui ont poussé à faire ces développements, nous aborderons la stratégie et méthodes utilisées comprenant la conception des impulsions radio-fréquence (RF), leur implémentation au sein de la séquence ainsi que l'optimisation du signal sur bruit temporel (tSNR) pour l'IRM fonctionnelle.

Motivations et contexte

L'Imagerie par Résonance Magnétique (IRM) est une modalité d'imagerie médicale utilisant les propriétés des protons d'hydrogène appelés spins. Ces derniers sont manipulés à l'aide de plusieurs champs magnétiques. Cette technique est particulièrement intéressante en imagerie cérébrale, car elle bénéficie d'une résolution spatiale avec une taille de pixel pouvant descendre en dessous du millimètre. L'imagerie à haute résolution est un puissant outil, car elle permet d'avoir accès de manière non invasive à des structures de plus en plus petites telles que l'hypothalamus ou les différentes couches corticales qui sont très étudiés en IRM fonctionnelle. L'IRM fonctionnelle (IRMf) est une méthode permettant de visualiser indirectement l'activité cérébrale via les changements locaux de concentration en hémoglobine oxygénée (BOLD). En acquérant des images rapidement (au moins chaque 2 secondes), il est possible d'échantillonner correctement le changement de signal BOLD et de le corréler soit à l'apparition de stimuli dans le cadre d'expériences d'IRMf ou au signal d'autres régions du cerveau dans le cadre d'IRMf de repos.

L'étude du cerveau par IRMf requiert l'emploi de résolutions spatiales de plus en plus grandes. En même temps, le réglage d'un protocole IRM est un compromis entre la résolution spatiale de l'image, le signal sur bruit (SNR) et le temps acquisition. L'IRM à ultra haut champ ($\geqslant 7$) bénéficie intrinsèquement d'un plus grand signal sur bruit ce qui permet de repousser les limites de résolution spatiale possible. C'est pour cela que le projet d'IRM à 11.7T Iseult a vu le jour en 2004 et fut installé à NeuroSpin en 2017. Malheureusement,

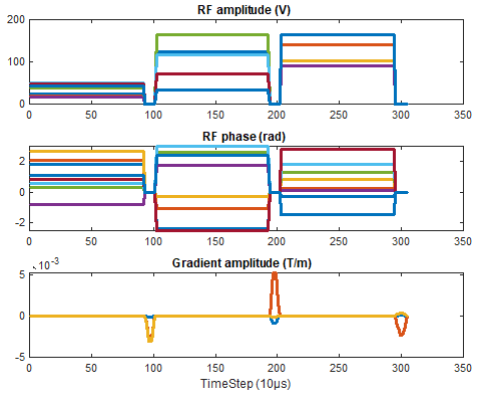

Figure A-1 : **Resultats d'un calcul avec 3 points-k_t.** A gauche de haut en bas, amplitude, phase (chaque couleur represente un canal de transmission) de la RF, blips de gradients (chaque couleur represente un axe de gradient). A droite, la trajectoire dans l'espace-k associée aux blips de gradient.

l'imagerie à ultra haut champ souffre d'artefacts d'inhomogénéités de champ RF, se traduisant par des régions sombres et une perte de contraste. En effet, à plus haut champ magnétique, la longueur d'onde des impulsions RF émises par les antennes est de plus en plus petite et atteind l'ordre de grandeur du cerveau, donnant lieu à des interférences constructives et destructives. La transmission parallèle permet de répondre à ce problème en autorisant un pilotage indépendant de chaque canal de transmission RF. Grâce à cette technologie, des méthodes de transmission RF développées à NeuroSpin telles que la paramétrisation en point-k_T permettent l'optimisation d'impulsions RF réduisant les inhomogénéités de champ RF tout en respectant les contraintes de sécurité liées au SAR, ainsi que les contraintes matérielles liées à l'antenne de transmission RF. Dans le cas des points k_T, ces impulsions RF consistent en une cascade de sous impulsions de magnitude et phase variable entrelacées avec des 'blips' de gradients (voir figure A-1).

Cependant, cette approche est peu fluide, car elle nécessite l'acquisition de cartes de champ magnétique RF ainsi que le calcul d'impulsions RF pendant l'expérience. Heureusement, la variabilité inter-sujets des profils des cartes de champ magnétique est relativement limitée. Cela représente une opportunité d'utiliser une approche d'impulsion point-k_T qui peut être robuste aux différences entre les sujets, et qui atténue le problème de l'inhomogénéité du champ RF sur une large population. Ainsi, il suffit d'optimiser une impulsion sur un groupe de sujets pour obtenir une solution " universelle ". Maintenant, le but de cette thèse est de développer une séquence d'IRM fonctionnelle incorporant ces impulsions RF universelles pour permettre l'exploitation de l'IRM Iseult à son plein potentiel et acquérir des images d'IRMf haute résolution.

Fabrication des impulsions RF

Étant donné les performances des gradients disponibles pour l'IRM Iseult, il est difficile à court terme d'obtenir une acquisition haute résolution tout en respectant les contraintes de résolution temporelle. Ainsi, une approche d'acquisition sur un champ de vue réduit a été adoptée. L'approche des impulsions universelles a donc été adaptée pour obtenir des impulsions RF universelles sélectives permettant l'excitation d'une tranche dont l'épaisseur, la

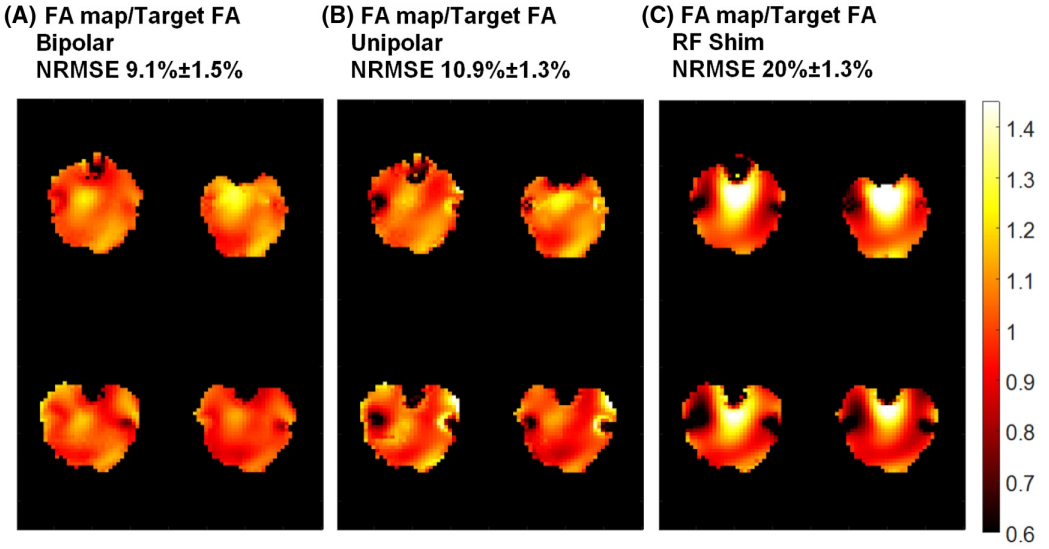

Figure A-2 : **Trois cartes d'angle de bascule obtenues par simulation de Bloch avec une impulsion universelle avec un gradient bipolaire (A), unipolaire (B) et avec une impulsion RF shimming (C).** Les cartes d'angle de bascule de 4 sujets parmi les 20 de la base de données sont montrées. Les cartes ont été normalisées par l'angle de bascule de consigne. Les impulsions avec un gradient bipolaire sont les plus homogènes.

position et l'orientation sont réglables. Pour ne pas devoir gérer une encombrante bibliothèque d'impulsions pour chaque épaisseur, position ou orientation de tranche, le choix a été fait de calculer une impulsion optimisée pour tout le cerveau. L'algorithme utilisé pour le calcul de l'impulsion reste donc le même que pour des impulsions universelles classiques, mais les contraintes changent. En effet, pour rendre ce pulse sélectif il suffit de traduire les pulses RF obtenus rectangulaires en sinus cardinaux apodisés couplée à l'ajout d'un gradient de sélection de coupe. Comme la durée de l'impulsion doit rester la même pour ne pas introduire de biais, le voltage pic du sinus cardinal est plus haut que sous sa forme rectangulaire. Ainsi les contraintes matérielles doivent pendre en compte la forme de sinus cardinal des impulsions RF. Il existe deux formes de gradients de sélection de coupe, bipolaires et unipolaires. Pour la fabrication des impulsions RF sélectives le choix s'est porté sur un gradient de forme bipolaire pour sa durée plus courte et sa plus grande robustesse aux problèmes de susceptibilités de champ magnétique. Deux impulsions RF universelles consistant en trois sous pulses de 0.92ms avec un gradient bipolaire et un gradient unipolaire ont été calculées sur une base de données comportant 20 cartes de B_0/B_1 puis comparées en simulation de Bloch à une impulsion optimisée par RF shimming en figure A-2. Les cartes d'angle de bascule de la magnétisation sont plus homogènes avec les impulsions universelles, d'autre part, l'impulsion utilisant un gradient bipolaire est plus homogène que la version unipolaire autour des régions ayant de forts artefacts de susceptibilité magnétique comme les canaux auditifs.

Malheureusement, les gradients bipolaires sont sensibles aux délais de gradient provenant du matériel ou des courants de Foucault générés par la commutation rapide de ceux là. Ces délais de quelques microsecondes, génèrent des artefacts où des zones de l'image sont assombries. Diffentes méthodes sont possibles pour corriger cet artefact, sous réserve de connaître le délai. Il est d'abord possible de décaler dans le temps les évenements de RF pour les repositionner correctement. Cette technique ne fonctionne pas dans pour une

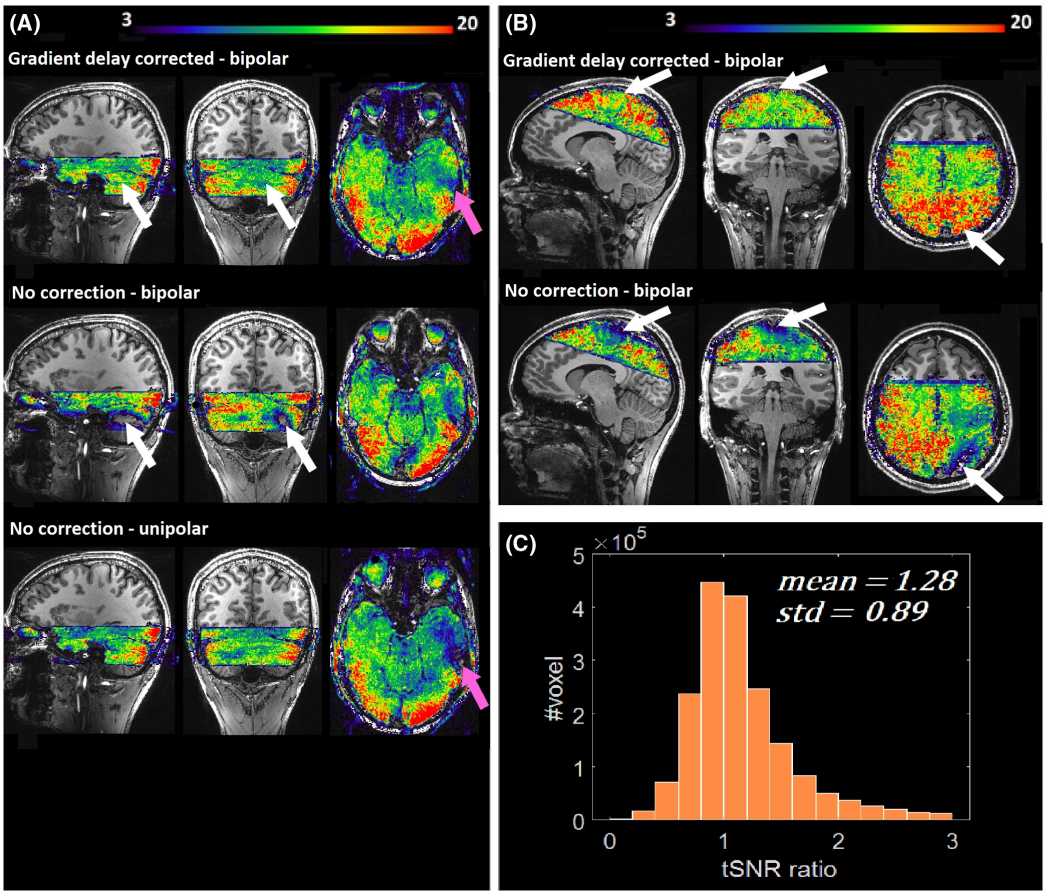

Figure A-3 : **Cartes de signal sur bruit temporel superposées sur une acquisition anatomique.** L'expérience a été reproduite sur deux volontaires (A et B). De haut en bas, impulsion bipolaire corrigée, bipolaire non corrigée, unipolaire. Les flèches blanches montrent des régions où les artefacts ont été corrigés grâce aux trim blips. Les flèches roses montrent des régions avec d'importants artefacts de susceptibilité où l'impulsion bipolaire est meilleure que l'impulsion unipolaire. En C, un histogramme du ratio de tSNR entre l'acquisition avec une impulsion bipolaire corrigée et non corrigée rassemblée pour les deux volontaires.

orientation oblique avec des délais différents sur chaque axe de gradient (situation de délais anisotropiques). La deuxième solution consiste à ajouter un décalage en phase, mais cette technique ne fonctionne que pour des coupes fines, car la phase à ajouter dépend de la position de la coupe. Cette méthode n'est pas adaptée pour les tranches épaisses de plusieurs centimètres. Nous avons donc proposé comme solution d'ajouter des moments supplémentaires aux blips de gradient, qui a l'avantage de fonctionner pour chaque orientation de coupe, même avec des délais différents sur chaque axe de gradient. La méthode a été expérimentée sur deux volontaires sains et comparée à une impulsion RF unipolaire (insensible aux délais de gradient) puis à une impulsion bipolaire sans correction. Des cartes de signal sur bruit temporel (tSNR) ont été acquises avec ces trois impulsions sur une séquence EPI-3D (voir figure A-3). La correction a permis de récupérer du signal, perdu avec l'approche bipolaire sans correction. D'autre part, le tSNR est meilleur dans les régions proches des canaux auditifs avec l'impulsion bipolaire corrigée que l'impulsion unipolaire. L'histogramme montre que de manière générale le tSNR est amélioré en corrigeant les délais de gradient.

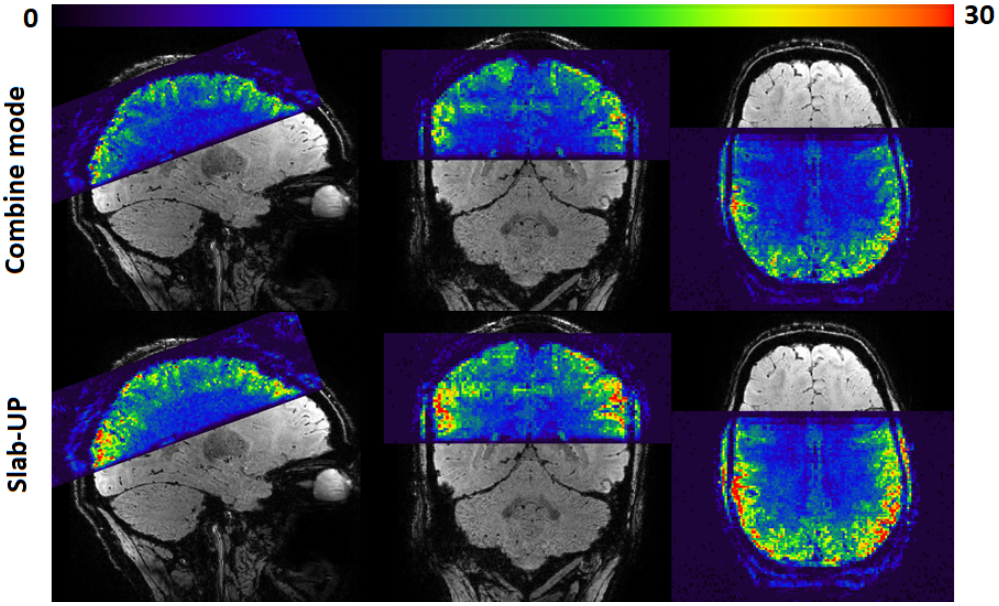

Figure A-4 : **Cartes de tSNR superposées sur une image anatomique.** La figure en haut correspond à une acquisition faite en transmission conventionnelle. La figure en bas correspond à une acquisition faite en transmission parallèle avec un pulse universel sélectif.

Implémentation sur la séquence

Pour être utilisés sur le système (Environnement IDEA Siemens Healthineers, Erlangen Allemagne), les impulsions sont injectées dans la séquence via des fichiers texte 'arbitraires' de type .ini. Ces fichiers contiennent les formes des impulsions de la RF en magnitude et phase ainsi que celle des gradients. Cependant, pour obtenir une tranche ajustée au champ de vue choisi par l'utilisateur, il faut que le gradient de sélection de coupe puisse être généré dynamiquement. Ainsi, un module générant ce gradient a été implémenté pour éviter d'avoir une bibliothèque de fichiers artbitraires pour chaque position/épaisseur/orientation de tranche. Ce module a été intégré à la séquence EPI-3D (auteur : Rudiger Stirnberg, DZNE Bonn Allemagne) mais son implémentation lui permet d'être intégrée à d'autres séquences (testées déjà dans une AFI, SPACE, GRE, MPRAGE). La figure A-4 montre des cartes de tSNR superposées sur une image anatomique. Le tSNR est meilleur avec la solution proposée, car la transmission conventionelle ne parvient pas à atteindre l'angle de bascule de consigne ce qui résulte en un signal plus faible et donc un tSNR plus faible.

La correction des délais de gradients dépend aussi de la position/épaisseur/orientation de la tranche. Par conséquent, un outil a été implémenté dans la séquence pour mesurer et ensuite corriger ces délais de gradient via la méthode que nous avons proposée. L'outil consiste en une double impulsion RF sélective. La première et deuxième impulsion sont déphasées de 180°, ainsi, sans délais de gradient, les impulsions s'annulent et la coupe centrale de la tranche a un signal nul. Sinon l'utilisateur peut ajouter un blip de gradient correspondant à un décalage en phase pour rétablir un déphasage effectif de 180°. Cette valeur de blip de gradient est ensuite appliquée à l'impulsion universelle. Figure A-5 montre deux cartes de tSNR acquises avec et sans la correction. L'expérience a été réalisée ici avec un angle de bascule inférieur à l'angle de Ernst pour accentuer les effets d'inhomogénéité de champ RF sur les cartes de tSNR. Les cartes de tSNR sont ici dans un régime dominé par le bruit

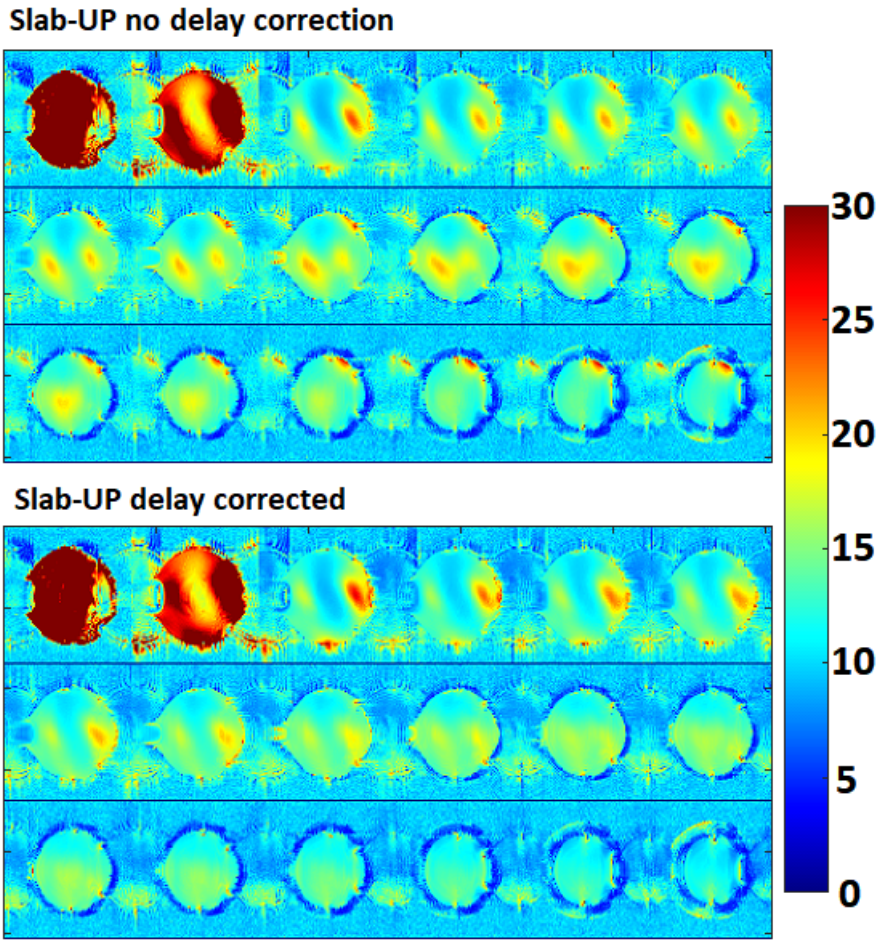

Figure A-5 : **Cartes de tSNR acquises avec et sans correction de délais.** L'estimation du délais a été effectuée avec le même outil. Le tSNR est assez faible pour être considéré égal au SNR. On voit que le profil de SNR est plus lisse avec la correction de délais ce qui suggère un champ RF plus homogène.

thermique ce qui permet d'affirmer que cela revient à avoir des cartes de SNR. Grâce à la correction, le profil de SNR est plus lisse suggérant un champ RF plus homogène.

Optimisation du signal sur bruit temporel par combinaison de canaux de réception

Lors d'une acquisition IRM avec une antenne RF multicanaux de réception, une image est reconstruite depuis chaque canal. L'image finale est typiquement calculée à partir de la somme des carrés de ces images (SoS). Cette méthode est quasi-optimale en SNR, mais elle ne l'est pas en tSNR, quantifiant la stabilité temporelle, qui est pourtant la métrique privilégiée en IRM fonctionnelle. Le but de ces travaux était de développer une alternative à la SoS dédiée à l'IRMf.

STARC est une combinaison de canaux optimale en tSNR. La méthode était à l'origine calculée via une optimisation par descente de gradient ce qui nécessitait l'exportation des données brutes qui étaient volumineuses. Pour remédier à ce problème nous avons proposé

une solution analytique pouvant facilement être intégrée en étape supplémentaire sur le reconstructeur d'image de l'IRM. D'autre part, bien que similaire au tSNR, il a été montré que le score du test de Student basé sur la moyenne (tsm) est une métrique mieux corrélée aux résultats des tests de Student pour un contraste donné. En effet, ce dernier prend en compte la variabilité du signal lié aux activations. Nous avons donc dérivé la solution de STARC pour obtenir une solution optimale en tsm ($STARC_{tsm}$). Ces deux solutions ont été comparées à la combinaison classique via une expérience d'IRMf sur quatre volontaires. Le paradigme fonctionnel consistait en une série de stimuli visuels, auditifs ainsi que des tâches motrices. La figure A-6 montre que malgré le gain en tSNR ou tsm, le score statistique des activations n'augmente pas voire diminue.

D'autre part, la combinaison $STARC_{tsm}$ souffre d'un biais statistique, car elle utilise la matrice de dessin de l'expérience comme a priori sur la variabilité du signal lié aux activations neuronales. Après correction par simulation de Monte Carlo, les performances de sensibilité de $STARC_{tsm}$ chutent en dessous de la combinaison de référence. Ainsi, ces résultats mettent ainsi en lumière les limites potentielles du tSNR lors de l'évaluation de la qualité des données d'IRMf.

Conclusion

Le travail fourni pendant cette thèse a permis de fournir une séquence d'IRM opérationnelle pour être utilisée à 11.7T. D'une part l'approche par impulsions universelles permet de minimiser les artefacts liés aux inhomogénéités de champ RF. D'autre part, leur traduction en pulses sélectifs permet d'effectuer des acquisitions sur des champs plus petits et donc de gagner en temps d'acquisition. Ensuite, leur intégration dans la séquence a permis de simplifier et fluidifier leur utilisation et d'améliorer leur robustesse face aux délais de gradients grâce à l'outil qui a été implémenté à cet effet. Enfin, nous avons montré expérimentalement les limites des metriques telles que le tSNR et le score-t de la moyenne pour évaluer la qualité des données d'IRMf. Nous espérons que cette séquence sera une pierre significative à l'édifice des acquisitions IRMf in vivo à venir sur l'IRM Iseult.

* * *
* *
*

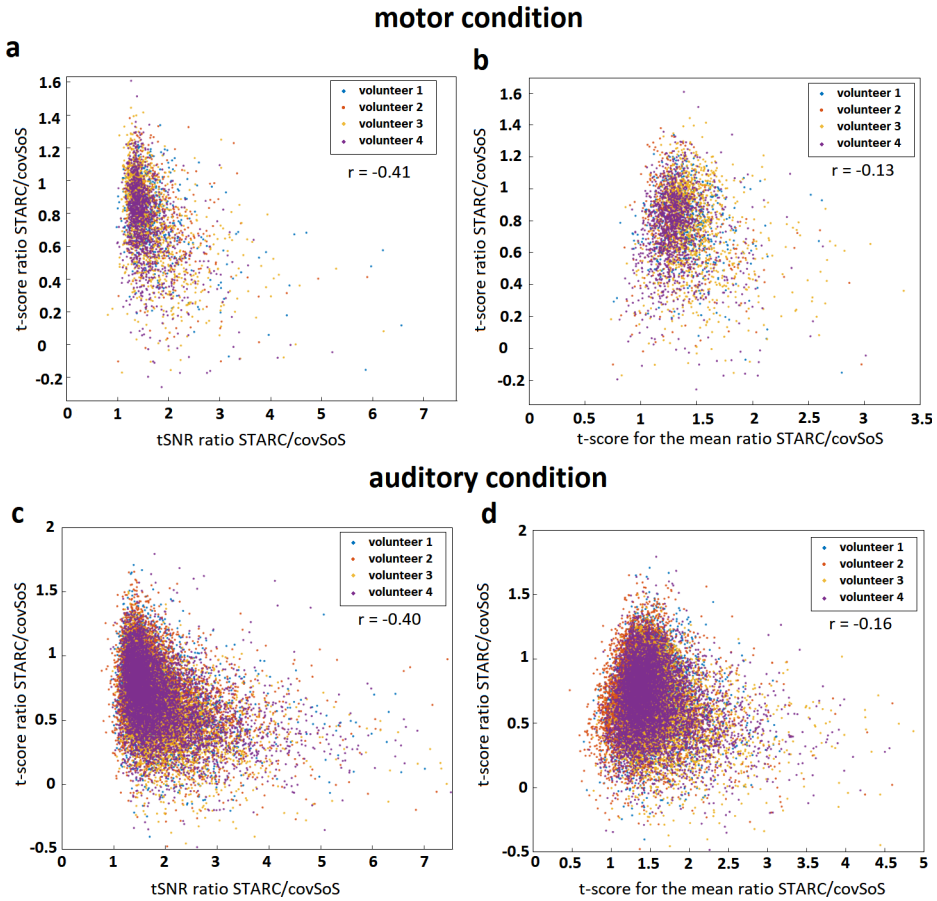

Figure A-6 : **Gains en score t par rapport aux gains en tSNR ou en score t basé sur la moyenne.** a - Nuage de points liant pour les voxels activés, le gain en tSNR contre le gain en t-score pour un contraste moteur. b - Nuage de points liant pour les voxels activés, le gain en score-t sur la moyenne contre le gain en score-t pour un contraste moteur. c - Pareil que a mais avec un contraste auditif. d - Pareil que b mais avec un contraste auditif. Chaque point correspond a un voxel activé ($p<0.001$) pour une combinaison covSoS. De manière générale, le gain en tSNR ne se traduit pas en gain en score-t.

List of Figures

0.1 **First MR images from Iseult MRI acquired at NeuroSpin**: MR image of a squash and an ex vivo brain at 0.4 mm isotropic resolution. Conventional transmission was used for this method leading to strong signal inhomogeneities in the image. They can be alleviated thanks to the parallel transmission techniques developped at NeuroSpin. 2

1.1-1 **Magnetization behavior after an excitation in a rotating frame around $\vec{z}$.**: After an RF excitation, the spin is tilted and a transversal magnetization appears in the $x - y$ plane. The frame of representation is a rotating at the Larmor frequency. 11

1.1-2 **Gradient for selective excitation**:Example for a gradient applied along $\vec{z}$. When a sinc shaped RF pulse is emitted coupled with a gradient on an axis, only a slice is selected. The thickness of the slice depends on the bandwidth of the pulse and the gradient amplitude. 12

1.1-3 **Longitudinal regrowth and transversal decay of magnetization** for white matter and gray matter at 7T. 14

1.2-4 **Free induction decay signal amplitude versus Gradient recalled echo signal**: the FID signal is oscillating because it is modulated at the Larmor frequency, it is decreasing in a T_2*. The GRE uses two gradient lobes to dephase and rephase again the spins leading to an 'echo'. 16

1.2-5 **3D-GRE chronogram**: Event through time for the GRE are summarized in a chronogram with RF, ADC and gradient events. In the GRE, only one k-space line per TR is acquired. Each line is encoded with the help of phase encode gradient G_{phase} and $G_{partition}$. The color of each gradient is represented by a movement of the same color (arrows) in k-space. 17

1.2-6 **Spin echo signal amplitude**: the spin echo allows to recover the T_2 by cancelling the effects static field inhomogeneity on the decay of the transversal magnetization. 18

1.2-7 **3D-EPI chronogram**: Like the 3D-GRE, the 3D-EPI uses two phase encoding gradients. The EPI consists in the sequential acquisition of each line of the k-space plane in a single TR. 19

1.3-8 **The brain from a macroscopic to a microscopic scale**: From left to right, the brain in axial view, the cortex, a neuron. 23

1.3-9 **The canonical hemodynamic response**: some models also include a signal dip at the beginning and at the end of the spike. 23

1.3-10 **An example of distortion correction**: illustrated here the method using two scans of opposite phase encoding direction. The correction is performed with the topup algorithm [ASA03] from the FSL library (FMRIB, Oxford UK). 25

2.1-1 **Fully sampled k-space compared to aliasing from GRAPPA and CAIPIRINHA for an acceleration factor of 2**: From left to right, fully sampled k-space, GRAPPA sampling, CAIPIRINHA sampling scheme. In bottom the corresponding reconstructed image. Aliasing is less severe with CAIPIRINHA than GRAPPA. 31

2.2-2 **tSNR versus SNR plot.** Different voxel sizes and magnetic fields are used. On the left, for an in vivo experiment and on the right on phantom. The physiological noise provokes a stalling of the tSNR at very high SNR. From [Tri+05]. 33

2.2-3 **Extreme susceptibility artifact due to braces.** From mriquestions.com. . 34

2.2-4 **Simulated B_1 inhomogeneities effect with field strength.** Simulated gradient echo with a birdcage coil [WC10]. 35

2.2-5 **B_1 inhomogeneities 3T versus 7T in vivo.** Same patient suffering from ischemic stroke (arrow heads) scanned at 3T (A) and 7T (B) with a FLAIR sequence. Despite slight differences in protocol settings signal dropouts are clearly visible on the temporal regions for the 7T scan (arrows). From [De +18]. 36

2.2-6 **Local SAR distribution for different frequencies.**: 10g SAR distribution for a birdcage coil in CP mode. SAR focuses in the center of the sample at frequencies. From Fiedler et al. [FLB18]. 37

2.3-7 **Conventional versus Parallel transmission.** Conceptual differences between conventional transmission (A) and parallel transmission (B). In conventional transmission the same RF pulse is amplified and splitted between channels. In parallel transmission, each transmission channel can be driven independently. 37

2.3-8 **Result of a 3 k_t-points design.** On the right RF amplitude, phase (each color represent a different transmission channel) and gradients blips (each color represent a gradient). On the left, k-space trajectory yielded by the gradient blips. 41

3.1-1 **Bipolar versus unipolar slab-selective gradient shapes.** The extra rephasing lobe makes the unipolar configuration less time efficient and less robust to ΔB_0 effects. 47

3.1-2 **Conversion from the non-selective UP to a slab-UP(axial), target FA = 30°.** Comparison between a non-selective UP (left) versus its slab selective pulse conversion (right). Each color represents a different transmit channel (top) and different gradient axis (middle). The blips in z axis (yellow) are played during the ramps of the slab-selective gradient. Notice the effect of the constraint peak voltage on the amplitude of the RF shapes. In this case, the maximum voltage was set up to 16.48V so the sinc RF shapes (BTP=10) respect the 'real' hardware constraint fixed at 165V. The bottom figures are simulated flip angle maps yielded by both excitations (whole brain NMRSE 9.1% over the database). The flip angle profile in the selected region by the slab-UP is the same as in the full brain flip angle map. 49

3.1-3 **Experimental Flip angle maps versus simulation with a slab-UP on phantom for two slab configurations. Sagittal view.** The similarity between the acquisition and simulation images show a good agreement between the theory and the experiment. Yellow pixels around the slab in the AFI acquisition are due to a wrong estimation of the flip angle because the signal is too weak. 50

3.1-4 **0.8 mm, 4.5 cm thick tilted slab-UP.** The slab (hot colomap) is thresholded and overlaid on an anatomical MPRAGE scan. 50

3.1-5 **Three simulated flip-angle (FA) maps from k_T-point solution for bipolar, unipolar, and RF shim configurations on the database, axial view.** Field maps over 4 subjects of the 20 found in the database are shown. The maps were normalized by the target flip angle. Bipolar pulses give more homogeneous maps than unipolar and RF shim pulses. Bipolar (A), unipolar (B), and RF shim (C) scenarios are shown. Abbreviation:NRMSE, normalized RMS error. 51

3.2-6 **Double RF subpulse experiment used to characterize gradient delays.** Gradient-induced rotations are displayed. Because of eddy currents and gradient delays, unwanted rotations arise. They can be corrected by a trim blip (green) between the two RF pulses. The second blip ensures intravoxel phase refocusing. 53

3.2-7 **Flip-angle ratio maps of phase correction, RF waveform time shift, and trim blip corrections for different delay configurations.** From left to right: simulations with delays of 4 μs on y and 2, 4, and 6 μs on z. From top to bottom: simulations without correction, with phase correction, RF waveform time-shifting, and trim blips. Each slab is compared with the no-delay reference-simulated flip-angle map on the top left with a ratio. Phase correction performs poorly for off-centered regions. The RF waveform time-shifting performs perfectly for isotropic delays, but only trim blips shows perfect correction for every configuration. 57

3.2-8 **Measured flip-angle maps versus Bloch simulations. For each volunteer, the top row displays AFI slab acquisitions, on the bottom row, Bloch simulations.** A, For volunteer 1, a +20° tilted slab was acquired with pulse 1 and enforced gradient anisotropy. B, For volunteer 2, a −20° tilted-slab pulse was acquired with pulse 2, with the measured, isotropic, gradient delays. We see good agreement between simulations and acquisitions, so that corrected pulses with trim blips alleviate effectively gradient delay effects. 58

3.2-9 **Temporal SNR (tSNR) maps from 3D-EPI acquisitions superposed on anatomical images and histogram of the ratio of the tSNR maps.** The double RF spoke pulse from the same design was used on the 2 volunteers with delay-corrected bipolar pulses (top row) and bipolar uncorrected pulses (bottom row). The pulses used are double-spoke RF pulses with axial (A) and −20° (B) tilted orientations derived from the universal kT-point solution. White arrows show regions where severe delay artifacts were corrected with trim blips. Pink arrows in (A) point toward large B_0 offsets (ear canals), where corrected bipolar pulses outperform the unipolar ones. C, Histogram of the tSNR ratio (bipolar corrected over bipolar uncorrected) pooled over the 2 subjects. 59

4.1-1 **Bloch simulations versus AFI flip angle maps (Target Flip angle = 15°, sagittal view).** Flip angle maps between Bloch simulations and acquisition with the modified AFI are in an acceptable agreement meaning that the implementation runs the pulses correctly. 64

4.1-2 **tSNR maps from the 3D-EPI-UP in vivo for two slab configurations.** Images acquired on combine mode are displayed on the left and with the Slab-UP on the right. Pink arrows indicate areas where the Slab-UP yields a tSNR clearly superior then in combine mode. 65

4.1-3 **tSNR maps overlaid on an anatomic EPI scan.** Top correspond to slab acquired in combined mode versus a slab acquired with a slab-UP in bottom. Here again the tSNR is clearly for the slab-UP acquisition is superior than combined mode. The slab thickness does not exceed the FOV. The high BTP of the slab-UP yields sharp slab profile compared to figure 3.1-2. 65

4.2-4 **Double RF spoke experiment with two different dephasing offsets.** On the left, the experiment is performed with a 180° net dephasing and on the right with a dephasing of 230°. The blue cross represents is located at center of the FOV. The axial view represents the middle slice of the FOV. 68

4.2-5 **tSNR map acquired with a slab-UP and with a slab-UP corrected for gradient delays. Axial view.** Top mosaic corresponds to the slab-UP acquisition and bottom one corresponds to the slab-UP with gradient delay correction. The tSNR map acquired with delay correction is smoother suggesting a smoother SNR and thus a more homogeneous RF magnetic field. 69

5.4-1 **tSNR results.** a - tSNR map from the same volunteer, scan and sagittal slice after covSoS, STARC, $STARC_{ps}$ and $STARC_{tsm}$ coil combinations. STARC yielded the highest tSNR map. b - Ratio of STARC and covSoS tSNR maps after median image filtering. STARC always improves tSNR, up to a factor 2. c - tSNR distributions pooled across all volunteers. Overall, STARC outperforms the other coil combinations in terms of tSNR. A brain mask was used to ignore non brain voxels. 79

5.4-2 **Activation results.** a - Activation maps for the motor contrast at p<0.001 (no correction) for covSoS, STARC, $STARC_{ps}$ and $STARC_{tsm}$. No double-dipping correction was applied to $STARC_{tsm}$. The shown maps are from the same volunteer as in Fig 1. b - Total number of activated voxels relative to the total number of voxels at different p-values and for different coil combinations, pooled over the volunteers. $STARC_{ps}$ and STARC have the poorest performance in terms of BOLD detection. CovSoS has the highest number of activations for the lowest p-values but $STARC_{tsm}$ (without double-dipping correction) reports more activations for the highest p-values. 80

5.4-3 **t-score gains versus tSNR or t-score for the mean gains.** a - Scatter plot linking the activated voxels, the tSNR gain with STARC to its t-score gain for motor contrast. b - Scatter plot linking the t-score for the mean gain with STARC to its t-score gain for motor contrast. c - Same plot than a but with auditory contrast. d - Same plot than b but with auditory contrast. Each point corresponds to an activated voxel (p<0.001) according to the covSoS combination maps. In general, an increase of tSNR did not yield a better t-score. 81

5.4-4 **Double-dipping results.** a - T-score distributions of covSoS and STARCtsm from noise signals and Monte Carlo simulations. The distribution of STARCtsm under the null hypothesis is distorted compared to covSoS because of double-dipping. b - Total number of activations relative to the total number of voxels at different p-values and for covSoS, STARCtsm and its double dipping corrected version for the in vivo scan. After correction, the number of activations from STARCtsm markedly drops. c - Activation maps on one volunteer for visual vs auditory contrast at p<0.001 (no correction). After double-dipping correction, activations are weaker and clusters smaller. 82

5.4-5 **Weights distributions from STARC optimization for two voxels.** a - Brain image from volunteer #2 axial view, the red points labelled A and B are the voxels whose weights are analysed. b - For both voxels A and B, the bar plots display the temporal mean, the temporal standard deviation and the optimized STARC weights. The channels receiving the strongest signal have the highest variability but will be given the lowest weight. c - Scatter plot of the mean versus the standard deviation for each channel, the slope of the linear fit of the ten strongest channels is also plotted. The signal variability is highly proportional to the signal strength. 83

5.4-6 **Signal time series for two activated voxels for covSoS and STARC.** A time series of the stimuli onset convolved with the canonical hrf is also displayed. Each graph corresponds to a voxel. CovSoS has higher activation peaks than STARC but the latter has the highest tSNR. 83

A-1 **Resultats d'un calcul avec 3 points-k_t.** A gauche de haut en bas, amplitude, phase (chaque couleur represente un canal de transmission) de la RF, blips de gradients (chaque couleur represente un axe de gradient). A droite, la trajectoire dans l'espace-k associée aux blips de gradient. 92

A-2 **Trois cartes d'angle de bascule obtenues par simulation de Bloch avec une impulsion universelle avec un gradient bipolaire (A), unipolaire (B) et avec une impulsion RF shimming (C).** Les cartes d'angle de bascule de 4 sujets parmi les 20 de la base de données sont montrées. Les cartes ont été normalisées par l'angle de bascule de consigne. Les impulsions avec un gradient bipolaire sont les plus homogènes. 93

A-3 **Cartes de signal sur bruit temporel superposées sur une acquisition anatomique.** L'expérience a été reproduite sur deux volontaires (A et B). De haut en bas, impulsion bipolaire corrigée, bipolaire non corrigée, unipolaire. Les flèches blanches montrent des régions où les artefacts ont été corrigés grâce aux trim blips. Les flèches roses montrent des régions avec d'importants artefacts de susceptibilité où l'impulsion bipolaire est meilleure que l'impulsion unipolaire. En C, un histogramme du ratio de tSNR entre l'acquisition avec une impulsion bipolaire corrigée et non corrigée rassemblée pour les deux volontaires. 94

A-4 **Cartes de tSNR superposées sur une image anatomique.** La figure en haut correspond à une acquisition faite en transmission conventionnelle. La figure en bas correspond à une acquisition faite en transmission parallèle avec un pulse universel sélectif. 95

A-5 **Cartes de tSNR acquises avec et sans correction de délais.** L'estimation du délais a été effectuée avec le même outil. Le tSNR est assez faible pour être considéré égal au SNR. On voit que le profil de SNR est plus lisse avec la correction de délais ce qui suggère un champ RF plus homogène. 96

A-6 **Gains en score t par rapport aux gains en tSNR ou en score t basé sur la moyenne.** a - Nuage de points liant pour les voxels activés, le gain en tSNR contre le gain en t-score pour un contraste moteur. b - Nuage de points liant pour les voxels activés, le gain en score-t sur la moyenne contre le gain en score-t pour un contraste moteur. c - Pareil que a mais avec un contraste auditif. d - Pareil que b mais avec un contraste auditif. Chaque point correspond a un voxel activé ($p<0.001$) pour une combinaison covSoS. De manière générale, le gain en tSNR ne se traduit pas en gain en score-t. 98

List of Tables

2.1 SAR limits as defined by the IEC, the limit for the partial body global SAR depends on the ratio exposed patient mass and patient mass. 36

Bibliography

[AB98] B. Aldefeld and P. Börnert. 'Effects of gradient anisotropy in MRI'. In: *Magnetic Resonance in Medicine* 39.4 (1998), pp. 606–614.

[ACM98] D. C. Alsop, T. J. Connick and G. Mizsei. 'A spiral volume coil for improved RF field homogeneity at high static magnetic field strength'. In: *Magnetic resonance in medicine* 40.1 (1998), pp. 49–54.

[ASA03] J. L. R. Andersson, S. Skare and J. Ashburner. 'How to correct susceptibility distortions in spin-echo echo-planar images: application to diffusion tensor imaging'. In: *NeuroImage* 20.2 (2003), pp. 870–888.

[Bil+15] B. Bilgic, B. A. Gagoski, S. F. Cauley, A. P. Fan, J. R. Polimeni, P. E. Grant, L. L. Wald and K. Setsompop. 'Wave-CAIPI for highly accelerated 3D imaging: Wave-CAIPI for Highly Accelerated 3D Imaging'. In: *Magnetic resonance in medicine* 73.6 (2015), pp. 2152–2162.

[Bis12] B. B. Biswal. 'Resting state fMRI: a personal history'. In: *NeuroImage* 62.2 (2012), pp. 938–944.

[BLA08] N. Boulant, D. Le Bihan and A. Amadon. 'Strongly modulating pulses for counteracting RF inhomogeneity at high fields'. In: *Magnetic resonance in medicine* 60.3 (2008), pp. 701–708.

[BMA09] N. Boulant, J.-F. Mangin and A. Amadon. 'Counteracting radio frequency inhomogeneity in the human brain at 7 Tesla using strongly modulating pulses'. In: *Magnetic resonance in medicine* 61.5 (2009), pp. 1165–1172.

[Bol+18] S. Bollmann, A. M. Puckett, R. Cunnington and M. Barth. 'Serial correlations in single-subject fMRI with sub-second TR'. In: *NeuroImage* 166 (2018), pp. 152–166.

[Bre+06] F. A. Breuer, M. Blaimer, M. F. Mueller, N. Seiberlich, R. M. Heidemann, M. A. Griswold and P. M. Jakob. 'Controlled aliasing in volumetric parallel imaging (2D CAIPIRINHA)'. In: *Magnetic resonance in medicine* 55.3 (2006), pp. 549–556.

[BS04] C. F. Beckmann and S. M. Smith. 'Probabilistic independent component analysis for functional magnetic resonance imaging'. In: *IEEE transactions on medical imaging* 23.2 (2004), pp. 137–152.

[CAM97] C. D. Constantinides, E. Atalar and E. R. McVeigh. 'Signal-to-noise measurements in magnitude images from NMR phased arrays'. In: *Magnetic resonance in medicine* 38.5 (1997), pp. 852–857.

[Cao+15] Z. Cao, J. Park, Z.-H. Cho and C. M. Collins. 'Numerical evaluation of image homogeneity, signal-to-noise ratio, and specific absorption rate for human brain imaging at 1.5, 3, 7, 10.5, and 14T in an 8-channel transmit/receive array: Simulating High-Field Human Brain MRI'. In: *Journal of magnetic resonance imaging* 41.5 (2015), pp. 1432–1439.

[Clo+12] M. A. Cloos, N. Boulant, M. Luong, G. Ferrand, E. Giacomini, D. Le Bihan and A. Amadon. 'kT-points: short three-dimensional tailored RF pulses for flip-angle homogenization over an extended volume'. In: *Magnetic resonance in medicine* 67.1 (2012), pp. 72–80.

[Cor+18] N. Corbin, N. Todd, K. J. Friston and M. F. Callaghan. 'Accurate modeling of temporal correlations in rapidly sampled fMRI time series'. In: *Human brain mapping* 39.10 (2018), pp. 3884–3897.

[De +13] F. De Martino, J. Zimmermann, L. Muckli, K. Ugurbil, E. Yacoub and R. Goebel. 'Cortical depth dependent functional responses in humans at 7T: improved specificity with 3D GRASE'. In: *PloS one* 8.3 (2013), e60514.

[De +18] L. J. De Cocker, A. Lindenholz, J. J. Zwanenburg, A. G. van der Kolk, M. Zwartbol, P. R. Luijten and J. Hendrikse. 'Clinical vascular imaging in the brain at 7T'. In: *NeuroImage* 168 (2018), pp. 452–458.

[DeD+16] D. J. DeDora, S. Nedic, P. Katti, S. Arnab, L. L. Wald, A. Takahashi, K. R. A. Van Dijk, H. H. Strey and L. R. Mujica-Parodi. 'Signal fluctuation sensitivity: An improved metric for optimizing detection of resting-state fMRI networks'. In: *Frontiers in neuroscience* 10 (2016), p. 180.

[Dup+15] L. Dupas, A. Massire, A. Amadon, A. Vignaud and N. Boulant. 'Two-spoke placement optimization under explicit specific absorption rate and power constraints in parallel transmission at ultra-high field'. In: *Journal of magnetic resonance (San Diego, Calif.: 1997)* 255 (2015), pp. 59–67.

[EG11] G. Eichfelder and M. Gebhardt. 'Local specific absorption rate control for parallel transmission by virtual observation points: Local SAR Control for Parallel Transmission'. In: *Magnetic resonance in medicine* 66.5 (2011), pp. 1468–1476.

[FLB18] T. M. Fiedler, M. E. Ladd and A. K. Bitz. 'SAR simulations and safety'. In: *NeuroImage* 168 (2018), pp. 33–58.

[Fri+94] K. J. Friston, A. P. Holmes, K. J. Worsley, J.-P. Poline, C. D. Frith and R. S. J. Frackowiak. 'Statistical parametric maps in functional imaging: A general linear approach'. In: *Human brain mapping* 2.4 (1994), pp. 189–210.

[Gei+07] A. Geissler, A. Gartus, T. Foki, A. R. Tahamtan, R. Beisteiner and M. Barth. 'Contrast-to-noise ratio (CNR) as a quality parameter in fMRI'. In: *Journal of magnetic resonance imaging* 25.6 (2007), pp. 1263–1270.

[Gra+15] V. Gras, M. Luong, A. Amadon and N. Boulant. 'Joint design of kT-points trajectories and RF pulses under explicit SAR and power constraints in the large flip angle regime'. In: *Journal of magnetic resonance (San Diego, Calif.: 1997)* 261 (2015), pp. 181–189.

[Gra+17a] V. Gras, M. Boland, A. Vignaud, G. Ferrand, A. Amadon, F. Mauconduit, D. Le Bihan, T. Stöcker and N. Boulant. 'Homogeneous non-selective and slice-selective parallel-transmit excitations at 7 Tesla with universal pulses: A validation study on two commercial RF coils'. In: *PloS one* 12.8 (2017), e0183562.

[Gra+17b] V. Gras, A. Vignaud, A. Amadon, D. Bihan and N. Boulant. 'Universal pulses: A new concept for calibration-free parallel transmission: Calibration-Free Parallel Transmission'. In: *Magnetic resonance in medicine* 77.2 (2017), pp. 635–643.

[Gra+17c] V. Gras, A. Vignaud, A. Amadon, F. Mauconduit, D. Le Bihan and N. Boulant. 'New method to characterize and correct with sub-µs precision gradient delays in bipolar multispoke RF pulses: Characterizing and Correcting for Gradient Delays with Sub-µs Precision'. In: *Magnetic resonance in medicine* 78.6 (2017), pp. 2194–2202.

[Gra+19] V. Gras, F. Mauconduit, A. Vignaud, C. Le Ster, L. Leroi, A. Amadon, E. Pracht, M. Boland, R. Stirnberg, T. Stocker, B. A. Poser, C. Wiggins, X. Wu, K. Ugurbil and N. Boulant. 'PASTeUR: Package of Anatomical Sequences using parallel Transmission UniveRsal kT-point pulses'. In: *ISMRM*. 2019.

[Gri+02] M. A. Griswold, P. M. Jakob, R. M. Heidemann, M. Nittka, V. Jellus, J. Wang, B. Kiefer and A. Haase. 'Generalized autocalibrating partially parallel acquisitions (GRAPPA)'. In: *Magnetic resonance in medicine* 47.6 (2002), pp. 1202–1210.

[GSC96] C. Gabriel, G. S. and E. Corthout. 'The dielectric properties of biological tissues: I. Literature survey'. In: *Physics in medicine and biology* 41.11 (1996), pp. 2231–2249.

[Gue+17] B. Guerin, J. F. Villena, A. G. Polimeridis, E. Adalsteinsson, L. Daniel, J. K. White and L. L. Wald. 'The ultimate signal-to-noise ratio in realistic body models: The Ultimate Signal-to-Noise Ratio in Realistic Body Models'. In: *Magnetic resonance in medicine* 78.5 (2017), pp. 1969–1980.

[HL79] D. I. Hoult and P. C. Lauterbur. 'The sensitivity of the zeugmatographic experiment involving human samples'. In: *Journal of magnetic resonance* 34.2 (1979), pp. 425–433.

[Hoy+14] A. Hoyos-Idrobo, P. Weiss, A. Massire, A. Amadon and N. Boulant. 'On variant strategies to solve the magnitude least squares optimization problem in parallel transmission pulse design and under strict SAR and power constraints'. In: *IEEE transactions on medical imaging* 33.3 (2014), pp. 739–748.

[HP00] D. I. Hoult and D. Phil. 'Sensitivity and power deposition in a high-field imaging experiment'. In: *Journal of magnetic resonance imaging* 12.1 (2000), pp. 46–67.

[Hub+17] L. Huber, D. Jandraw, M. Sean and P. A. Bandettini. 'Simple approach to improve time series fMRI stability: STAbility-weighted Rf-coil Combination (STARC)'. In: *ISMRM*. 2017.

[Jam+21a] R. Jamil, F. Mauconduit, V. Gras and N. Boulant. 'General gradient delay correction method in bipolar multispoke RF pulses using trim blips'. In: *Magnetic resonance in medicine* 85.2 (2021), pp. 1004–1012.

[Jam+21b] R. Jamil, F. Mauconduit, C. Le Ster, P. Ehses, B. A. Poser, A. Vignaud and N. Boulant. 'Temporal SNR optimization through RF coil combination in fMRI: The more, the better?' In: *PloS one* 16.11 (2021), e0259592.

[Jan+10] M. Jankiewicz, H. Zeng, J. E. Moore, A. W. Anderson, M. J. Avison, E. B. Welch and J. C. Gore. 'Practical considerations for the design of sparse-spokes pulses'. In: *Journal of magnetic resonance (San Diego, Calif.: 1997)* 203.2 (2010), pp. 294–304.

[Jen+02] M. Jenkinson, P. Bannister, M. Brady and S. Smith. 'Improved optimization for the robust and accurate linear registration and motion correction of brain images'. In: *NeuroImage* 17.2 (2002), pp. 825–841.

[Kas+18] S. Kashyap, F. J. Fritz, R. L. Harms, L. Huber, D. Ivanov, A. Roebroeck, B. A. Poser and K. Uludag. 'Effect of optimized coil-combinations on high-resolution laminar fMRI at 9.4T'. In: *ISMRM*. 2018.

[Kat+03] U. Katscher, P. Börnert, C. Leussler and J. S. van den Brink. 'Transmit SENSE: Transmit SENSE'. In: *Magnetic resonance in medicine* 49.1 (2003), pp. 144–150.

[KG01] G. Krüger and G. H. Glover. 'Physiological noise in oxygenation-sensitive magnetic resonance imaging: Physiological Noise in MRI'. In: *Magnetic resonance in medicine* 46.4 (2001), pp. 631–637.

[Kle+09] A. Klein, J. Andersson, B. A. Ardekani, J. Ashburner, B. Avants, M.-C. Chiang, G. E. Christensen, D. L. Collins, J. Gee, P. Hellier, J. H. Song, M. Jenkinson, C. Lepage, D. Rueckert, P. Thompson, T. Vercauteren, R. P. Woods, J. J. Mann and R. V. Parsey. 'Evaluation of 14 nonlinear deformation algorithms applied to human brain MRI registration'. In: *NeuroImage* 46.3 (2009), pp. 786–802.

[Kri+09] N. Kriegeskorte, W. K. Simmons, P. S. F. Bellgowan and C. I. Baker. 'Circular analysis in systems neuroscience: the dangers of double dipping'. In: *Nature neuroscience* 12.5 (2009), pp. 535–540.

[Lar+03] E. G. Larsson, D. Erdogmus, R. Yan, J. C. Principe and J. R. Fitzsimmons. 'SNR-optimality of sum-of-squares reconstruction for phased-array magnetic resonance imaging'. In: *Journal of magnetic resonance (San Diego, Calif.: 1997)* 163.1 (2003), pp. 121–123.

[Le +19] C. Le Ster, A. Moreno, F. Mauconduit, V. Gras, R. Stirnberg, B. A. Poser, A. Vignaud, E. Eger, S. Dehaene, F. Meyniel and N. Boulant. 'Comparison of SMS-EPI and 3D-EPI at 7T in an fMRI localizer study with matched spatiotemporal resolution and homogenized excitation profiles'. In: *PloS one* 14.11 (2019), e0225286.

[Lee+12] J. Lee, M. Gebhardt, L. L. Wald and E. Adalsteinsson. 'Local SAR in parallel transmission pulse design: Local-SAR Constrained pTx RF Design'. In: *Magnetic resonance in medicine* 67.6 (2012), pp. 1566–1578.

[Lou+15] C. Louapre, S. T. Govindarajan, C. Giannì, C. Langkammer, J. A. Sloane, R. P. Kinkel and C. Mainero. 'Beyond focal cortical lesions in MS: An in vivo quantitative and spatial imaging study at 7T'. In: *Neurology* 85.19 (2015), pp. 1702–1709.

[Mas+22] A. Massire, F. Mauconduit, V. Gras, M. Lapert, M. Naudin, R. Guillevin, A. Vignaud and N. Boulant. 'PASTEUR: Package of Anatomical Sequences Using Parallel Transmission Universal Pulses Now Available for MAGNETOM Terra'. In: *Magnetom Flash* (2022).

[MBB07] K. Murphy, J. Bodurka and P. A. Bandettini. 'How long to scan? The relationship between fMRI temporal signal to noise ratio and necessary scan duration'. In: *NeuroImage* 34.2 (2007), pp. 565–574.

[MSC06] W. Mao, M. B. Smith and C. M. Collins. 'Exploring the limits of RF shimming for high-field MRI of the human head'. In: *Magnetic resonance in medicine* 56.4 (2006), pp. 918–922.

[Noc06] W. S. Nocedal J. *Numerical Optimization*. Springer New York, NY, 2006.

[OA98] O. Ocali and E. Atalar. 'Ultimate intrinsic signal-to-noise ratio in MRI'. In: *Magnetic resonance in medicine* 39.3 (1998), pp. 462–473.

[Oel+04] M. Oelhafen, K. P. Pruessmann, S. Kozerke and P. Boesiger. 'Calibration of echo-planar 2D-selective RF excitation pulses'. In: *Magnetic Resonance in Medicine* 52.5 (2004), pp. 1136–1145.

[Oga+90] S. Ogawa, T. M. Lee, A. R. Kay and D. W. Tank. 'Brain magnetic resonance imaging with contrast dependent on blood oxygenation'. In: *Proceedings of the National Academy of Sciences of the United States of America* 87.24 (1990), pp. 9868–9872.

[Orz+10] S. Orzada, S. Maderwald, B. A. Poser, A. K. Bitz, H. H. Quick and M. E. Ladd. 'RF excitation using time interleaved acquisition of modes (TIAMO) to address B1 inhomogeneity in high-field MRI'. In: *Magnetic resonance in medicine* 64.2 (2010), pp. 327–333.

[OY11] C. A. Olman and E. Yacoub. 'High-field FMRI for human applications: an overview of spatial resolution and signal specificity'. In: *The open neuroimaging journal* 5.Suppl 1 (2011), pp. 74–89.

[Pin+07] P. Pinel, B. Thirion, S. Meriaux, A. Jobert, J. Serres, D. Le Bihan, J.-B. Poline and S. Dehaene. 'Fast reproducible identification and large-scale databasing of individual functional cognitive networks'. In: *BMC neuroscience* 8.1 (2007), p. 91.

[PNM11] J. Pauly, D. Nishimura and A. Macovski. 'A k-space analysis of small-tip-angle excitation.' In: *Journal of magnetic resonance (San Diego, Calif.: 1997)* 213.2 (2011), pp. 544–557.

[Pos+10] B. A. Poser, P. J. Koopmans, T. Witzel, L. L. Wald and M. Barth. 'Three dimensional echo-planar imaging at 7 Tesla'. In: *NeuroImage* 51.1 (2010), pp. 261–266.

[Pru+99] K. P. Pruessmann, M. Weiger, M. B. Scheidegger and P. Boesiger. 'SENSE: sensitivity encoding for fast MRI'. In: *Magnetic resonance in medicine* 42.5 (1999), pp. 952–962.

[PS18] B. A. Poser and K. Setsompop. 'Pulse sequences and parallel imaging for high spatiotemporal resolution MRI at ultra-high field'. In: *NeuroImage* 168 (2018), pp. 101–118.

[PSS16] R. Pohmann, O. Speck and K. Scheffler. 'Signal-to-noise ratio and MR tissue parameters in human brain imaging at 3, 7, and 9.4 tesla using current receive coil arrays: SNR at 9.4T'. In: *Magnetic resonance in medicine* 75.2 (2016), pp. 801–809.

[RFF02] S. Rieseberg, J. Frahm and J. Finsterbusch. 'Two-dimensional spatially-selective RF excitation pulses in echo-planar imaging'. In: *Magnetic resonance in medicine* 47.6 (2002), pp. 1186–1193.

[RHU18] S. Rosenzweig, H. C. Holme and M. Uecker. 'Simple auto-calibrated gradient delay estimation from few spokes using radial intersections (ring)'. In: *Magnetic Resonance in Medicine* 81.3 (2018), pp. 1898–1906.

[Rob+98] P. M. Robitaille, A. M. Abduljalil, A. Kangarlu, X. Zhang, Y. Yu, R. Burgess, S. Bair, P. Noa, L. Yang, H. Zhu, B. Palmer, Z. Jiang, D. M. Chakeres and D. Spigos. 'Human magnetic resonance imaging at 8 T'. In: *NMR in biomedicine* 11.6 (1998), pp. 263–265.

[Roe+90] P. B. Roemer, W. A. Edelstein, C. E. Hayes, S. P. Souza and O. M. Mueller. 'The NMR phased array'. In: *Magnetic resonance in medicine* 16.2 (1990), pp. 192–225.

[Sae+06] S. Saekho, C.-Y. Yip, D. C. Noll, F. E. Boada and V. A. Stenger. 'Fast-kz three-dimensional tailored radiofrequency pulse for reduced B1 inhomogeneity'. In: *Magnetic resonance in medicine* 55.4 (2006), pp. 719–724.

[SE16] K. Scheffler and P. Ehses. 'High-resolution mapping of neuronal activation with balanced SSFP at 9.4 tesla: High-Resolution bSSFP Functional Imaging at 9.4T'. In: *Magnetic resonance in medicine* 76.1 (2016), pp. 163–171.

[Set+12] K. Setsompop, B. A. Gagoski, J. R. Polimeni, T. Witzel, V. J. Wedeen and L. L. Wald. 'Blipped-controlled aliasing in parallel imaging for simultaneous multislice echo planar imaging with reduced g-factor penalty: Blipped-CAIPI for Simultaneous Multislice EPI'. In: *Magnetic resonance in medicine* 67.5 (2012), pp. 1210–1224.

[SS21] R. Stirnberg and T. Stöcker. 'Segmented K-space blipped-controlled aliasing in parallel imaging for high spatiotemporal resolution EPI'. In: *Magnetic resonance in medicine* 85.3 (2021), pp. 1540–1551.

[TG97] A. Tannus and M. Garwood. 'Adiabatic pulses'. In: *NMR in biomedicine* 10.8 (1997), pp. 423–434.

[TPW11] C. Triantafyllou, J. R. Polimeni and L. L. Wald. 'Physiological noise and signal-to-noise ratio in fMRI with multi-channel array coils'. In: *NeuroImage* 55.2 (2011), pp. 597–606.

[Tri+05] C. Triantafyllou, R. D. Hoge, G. Krueger, C. J. Wiggins, A. Potthast, G. C. Wiggins and L. L. Wald. 'Comparison of physiological noise at 1.5 T, 3 T and 7 T and optimization of fMRI acquisition parameters'. In: *NeuroImage* 26.1 (2005), pp. 243–250.

[Tri+16] C. Triantafyllou, J. R. Polimeni, B. Keil and L. L. Wald. 'Coil-to-coil physiological noise correlations and their impact on functional MRI time-series signal-to-noise ratio'. In: *Magnetic resonance in medicine* 6 (2016), pp. 1708–1719.

[TWP17] D. H. Y. Tse, C. J. Wiggins and B. A. Poser. 'Estimating and eliminating the excitation errors in bipolar gradient composite excitations caused by radiofrequency-gradient delay: Example of bipolar spokes pulses in parallel transmission: Estimating and Eliminating Gradient Delays in pTx Spokes Pulses'. In: *Magnetic resonance in medicine* 78.5 (2017), pp. 1883–1890.

[Ugu14] K. Ugurbil. 'Magnetic resonance imaging at ultrahigh fields'. In: *IEEE transactions on bio-medical engineering* 61.5 (2014), pp. 1364–1379.

[UMU09] K. Uludag, B. Müller-Bierl and K. Ugurbil. 'An integrative model for neuronal activity-induced signal changes for gradient and spin echo functional imaging'. In: *NeuroImage* 48.1 (2009), pp. 150–165.

[Vio+21] L. Vionnet, A. Aranovitch, Y. Duerst, M. Haeberlin, B. E. Dietrich, S. Gross and K. P. Pruessmann. 'Simultaneous feedback control for joint field and motion correction in brain MRI'. In: *NeuroImage* 226.117286 (2021), p. 117286.

[WC10] A. G. Webb and C. M. Collins. 'Parallel transmit and receive technology in high-field magnetic resonance neuroimaging'. In: *International journal of imaging systems and technology* 20.1 (2010), pp. 2–13.

[Web11] A. G. Webb. 'Dielectric materials in magnetic resonance'. In: *Concepts in magnetic resonance. Part A, Bridging education and research* 38A.4 (2011), pp. 148–184.

[WF95] K. J. Worsley and K. J. Friston. 'Analysis of fMRI time-series revisited–again'. In: *NeuroImage* 2.3 (1995), pp. 173–181.

[WR13] M. Welvaert and Y. Rosseel. 'On the definition of signal-to-noise ratio and contrast-to-noise ratio for fMRI data'. In: *PloS one* 8.11 (2013), e77089.

[Yac+01] E. Yacoub, A. Shmuel, J. Pfeuffer, P. F. Van De Moortele, G. Adriany, P. Andersen, J. T. Vaughan, H. Merkle, K. Ugurbil and X. Hu. 'Imaging brain function in humans at 7 Tesla'. In: *Magnetic resonance in medicine* 45.4 (2001), pp. 588–594.

[Yan+02] Q. X. Yang, J. Wang, X. Zhang, C. M. Collins, M. B. Smith, H. Liu, X.-H. Zhu, J. T. Vaughan, K. Ugurbil and W. Chen. 'Analysis of wave behavior in lossy dielectric samples at high field'. In: *Magnetic resonance in medicine* 47.5 (2002), pp. 982–989.

[Yan+06] Q. X. Yang, W. Mao, J. Wang, M. B. Smith, H. Lei, X. Zhang, K. Ugurbil and W. Chen. 'Manipulation of image intensity distribution at 7.0 T: passive RF shimming and focusing with dielectric materials'. In: *Journal of magnetic resonance imaging* 24.1 (2006), pp. 197–202.

[Yar07] V. L. Yarnykh. 'Actual flip-angle imaging in the pulsed steady state: a method for rapid three-dimensional mapping of the transmitted radiofrequency field'. In: *Magnetic resonance in medicine* 57.1 (2007), pp. 192–200.

[Zwa+09] W. van der Zwaag, S. Francis, K. Head, A. Peters, P. Gowland, P. Morris and R. Bowtell. 'fMRI at 1.5, 3 and 7 T: characterising BOLD signal changes'. In: *NeuroImage* 47.4 (2009), pp. 1425–1434.